BEILSTEIN JOURNAL OF NANOTECHNOLOGY

Nanophotonics, nano-optics and nanospectroscopy

Edited by Alfred J. Meixner

Imprint

Beilstein Journal of Nanotechnology
www.bjnano.org
ISSN 2190-4286
Email: journals-support@beilstein-institut.de

The *Beilstein Journal of Nanotechnology* is published by the Beilstein-Institut zur Förderung der Chemischen Wissenschaften.

Beilstein-Institut zur Förderung der Chemischen Wissenschaften
Trakehner Straße 7–9
60487 Frankfurt am Main
Germany
www.beilstein-institut.de

Beilstein Journal of Nanotechnology

Nanophotonics, nano-optics and nanospectroscopy

Alfred J. Meixner

Editorial

Open Access

Address:
Institute of Physical and Theoretical Chemistry, University of Tübingen, Auf der Morgenstelle 18, 72076 Tübingen, Germany

Email:
Alfred J. Meixner - alfred.meixner@ipc.uni-tuebingen.de

Keywords:
nano-optics; nanophotonics; nanospectroscopy

Beilstein J. Nanotechnol. **2011,** *2,* 499–500.
doi:10.3762/bjnano.2.53

Received: 07 August 2011
Accepted: 10 August 2011
Published: 30 August 2011

This article is part of the Thematic Series "Nanophotonics, nano-optics and nanospectroscopy".

Editor-in-Chief: T. Schimmel

This Thematic Series of the *Beilstein Journal of Nanotechnology* is devoted to nanophotonics, nano-optics and nanospectroscopy, and covers the field where nanoscience meets photonics, optics and spectroscopy. Since the pioneering days of scanning near-field optical microscopy [1,2], one of the main goals has been to combine scanning probe microscopy techniques with the spectroscopic means to characterize the chemical structure of materials with nanometer spatial resolution [3-6]. This has turned out to be a demanding but, at the same time, rewarding endeavor. The scaling down of optics and spectroscopy to the length scale of molecules is not simply a matter of making things smaller; the optical phenomena and spectroscopic behavior at the nanoscale are indeed markedly different from those at the macroscopic scale. This challenge continues to fascinate researchers all around the world and has led to many new discoveries concerning the interaction between light and matter at dimensions much smaller than the wavelength of electromagnetic radiation [7-9]. Well-known examples are the negative refractive index created by metamaterials [10,11], the quantum confinement observed in the absorption and luminescence spectra of semiconductor nanoparticles [12], and the plasmon resonances of silver and gold nanoparticles. The concept of plasmon resonance has led to broad applications, such as optical antennas made from noble metals, which have been used to locally focus light into volumes with dimensions far below the diffraction limit and to enhance the emission of locally excited states into the far field [13]. Equally important are fundamental studies of the optical properties of individual quantum systems, such as single atoms, single molecules [14] or single quantum dots, with high spectral resolution and high time resolution. A single molecule is the smallest chemical unit and can be regarded as a single-photon source; its optical properties demonstrate most naturally the quantum characteristics of light and reveal details of intermolecular interactions that would be otherwise hidden in an ensemble.

Nanophotonics and nanospectroscopy shine light into this intriguing new world. The study of the interaction between light and matter at the nanometer scale is motivated by the rapid progress in nanoscience and nanotechnology and requires the close cooperation of researchers from a number of different disciplines, including physics, chemistry and biology. Widespread applications can be imagined, e.g., in materials sciences in the pursuit of efficient photovoltaic energy conversion; in the

engineering sciences as quantum devices functioning as switches that truly operate at the quantum limit with single photons; or in the life sciences as local optical sensors to observe chemical processes in living cells.

Tübingen, August 2011

Alfred J. Meixner

References

1. Pohl, D. W.; Denk, W.; Lanz, M. *Appl. Phys. Lett.* **1984,** *44,* 651–653. doi:10.1063/1.94865
2. Lewis, A.; Isaacson, M.; Harootunian, A.; Muray, A. *Ultramicroscopy* **1984,** *13,* 227–231. doi:10.1016/0304-3991(84)90201-8
3. Betzig, E.; Trautman, J. K. *Science* **1992,** *257,* 189–195. doi:10.1126/science.257.5067.189
4. Betzig, E.; Chichester, R. J. *Science* **1993,** *262,* 1422–1425. doi:10.1126/science.262.5138.1422
5. Stöckle, R. M.; Suh, Y. D.; Deckert, V.; Zenobi, R. *Chem. Phys. Lett.* **2000,** *318,* 131–136. doi:10.1016/S0009-2614(99)01451-7
6. Hayazawa, N.; Inouye, Y.; Sekkat, Z.; Kawata, S. *Chem. Phys. Lett.* **2001,** *335,* 369–374. doi:10.1016/S0009-2614(01)00065-3
7. Novotny, L.; Hecht, B. *Principles of Nano-Optics;* Cambridge University Press: Cambridge, 2006.
8. Gaponenko, S. V. *Introduction to Nanophotonics;* Cambridge University Press: Cambridge, 2010.
9. Maier, S. A. *Plasmonics: Fundamentals and Applications;* Springer: New York, 2007.
10. Lezec, H. J.; Dionne, J. A.; Atwater, H. A. *Science* **2007,** *316,* 430–432. doi:10.1126/science.1139266
11. Boltasseva, A.; Atwater, H. A. *Science* **2011,** *331,* 290–291. doi:10.1126/science.1198258
12. Michler, P., Ed. *Single Quantum Dots: Fundamentals, Applications and New Concepts (Topics in Applied Physics);* Springer: Berlin, Germany, 2003.
13. Mühlschlegel, P.; Eisler, H.-J.; Martin, O. J. F.; Hecht, B.; Pohl, D. W. *Science* **2005,** *308,* 1607–1609. doi:10.1126/science.1111886
14. Basché, T.; Moerner, W. E.; Orrit, M.; Wild, U. P., Eds. *Single-Molecule Optical Detection, Imaging and Spectroscopy;* Wiley-VCH: Weinheim, Germany, 1997.

License and Terms

Beilstein Journal of Nanotechnology

Towards multiple readout application of plasmonic arrays

Dana Cialla[‡1], Karina Weber[‡1], René Böhme[1], Uwe Hübner[2], Henrik Schneidewind[2], Matthias Zeisberger[2], Roland Mattheis[2], Robert Möller[1] and Jürgen Popp[*1,2]

Letter

Open Access

Address:
[1]Institute of Physical Chemistry and Abbe Center of Photonics, Friedrich-Schiller-University Jena, Helmholtzweg 4, 07743 Jena, Germany and [2]Institute of Photonic Technology, Albert-Einstein-Straße 9, 07745 Jena, Germany

Email:
Jürgen Popp[*] - juergen.popp@uni-jena.de

* Corresponding author ‡ Equal contributors

Keywords:
fluorescence; multiple readout; plasmonic array; surface-enhanced fluorescence (SEF); surface-enhanced Raman spectroscopy (SERS)

Beilstein J. Nanotechnol. **2011,** *2,* 501–508.
doi:10.3762/bjnano.2.54

Received: 29 April 2011
Accepted: 12 August 2011
Published: 30 August 2011

This article is part of the Thematic Series "Nanophotonics, nano-optics and nanospectroscopy".

Guest Editor: A. J. Meixner

Abstract

In order to combine the advantages of fluorescence and surface-enhanced Raman spectroscopy (SERS) on the same chip platform, a nanostructured gold surface with a unique design, allowing both the sensitive detection of fluorescence light together with the specific Raman fingerprint of the fluorescent molecules, was established. This task requires the fabrication of plasmonic arrays that permit the binding of molecules of interest at different distances from the metallic surface. The most efficient SERS enhancement is achieved for molecules directly adsorbed on the metallic surface due to the strong field enhancement, but where, however, the fluorescence is quenched most efficiently. Furthermore, the fluorescence can be enhanced efficiently by careful adjustment of the optical behavior of the plasmonic arrays. In this article, the simultaneous application of SERS and fluorescence, through the use of various gold nanostructured arrays, is demonstrated by the realization of a DNA detection scheme. The results shown open the way to more flexible use of plasmonic arrays in bioanalytics.

Introduction

Fluorescence spectroscopy and microscopy is one of the most important analytical techniques in the life sciences and medicine. Due to its extreme sensitivity, fluorescence allows investigations on a single-molecule level [1]. Fluorescence in bioanalytics is mostly used for tracking intrinsic fluorophors (autofluorescence) or special fluorescence labels, which selectively bind to special cellular functional groups, such as proteins or nucleic acids [2,3]. However, the broad emission spectrum of the fluorescence reporter molecules prevents the parallel detection of several fluorescent dye labels by fluorescence microscopy.

Raman spectroscopy, i.e., the excitation of vibrational modes through inelastic light scattering, allows one to obtain highly specific molecular fingerprint information without the need for external labels. The drawback of the intrinsically small Raman scattering cross sections not allowing for trace analytics and fast detections times can be overcome by applying surface-enhanced Raman spectroscopy (SERS). The enhancement of the inherently small Raman cross sections by applying SERS is based on the strong plasmonic field enhancement at rough metallic surfaces. Since SERS combines the unique fingerprint specificity of Raman with trace level sensitivity, it is a very active topic in (bio)analytics [4-13].

In order to exploit the advantages of both fluorescence and SERS spectroscopy in a single sensor platform, the goal of the work presented here is the development and application of an innovative nanostructured surface that will allow both detection schemes. Thus, several requirements must be fulfilled by the plasmonic array:

(1) Periodically patterned arrays with homogenous signal enhancement must be prepared, because difficulties in the fabrication of metallic surfaces with reproducible signal enhancement hamper the routine application of SERS as a (bio)analytical tool [14]. (2) A patterned plasmonic active film is essential for detecting both fluorescence and SERS signals through a single plasmonic array, since the optimum distance between the (fluorescent) molecules and the metallic surface, for gaining the maximum signal intensity, is different in the two cases. The most efficient SERS enhancement is achieved for molecules within the first layer of the metallic surface, where the fluorescence signal will be quenched most efficiently. Thus, a parallel detection of fluorescence and SERS is prevented when applying a continuously nanostructured metallic layer, such as roughened metal electrodes, as a sensor array. (3) A further requirement which has to be fulfilled is the realization of large-scale production capacity for applications in (bio)analytics.

One of the most common type of periodically patterned plasmonic arrays is based on the formation of a polystyrene or silicon dioxide bead mask during the production process, such as in nanosphere lithography (NSL) [15,16], film over nanospheres (FON) [17,18], and sculpted SERS substrates [19]. Here, the arrays are tunable by varying the size of the monodisperse polystyrene or silicon dioxide beads. Unfortunately, frequently occurring constructional defects within the mask are transferred to the nanostructured metallic surface. Furthermore, electron beam lithography (EBL) [20] is a promising production technique for periodically patterned plasmonic arrays. We have recently shown that gold nanorhomb arrays produced by EBL [21] provide a homogenous signal enhancement across a large area [22]. By virtue of the patterning process, the optical parameters are tunable by varying both the size of the nanoparticles and the period of the array [23], which leads to design and fabrication strategies of SERS arrays developed to gain a maximum SERS enhancement [24].

Furthermore, the use of our gold nanorhomb arrays fabricated on a quartz wafer allows the binding of analyte molecules also through direct attachment to the quartz surface. Thus, molecule–surface distances from zero to several tens of nanometers (depending on interparticle distances) can be obtained, hence allowing both fluorescence and SERS detection. Finally, once optimized, plasmonic arrays produced by electron beam lithography can also be prepared through nanoimprint techniques, an inexpensive method to manufacture large quantities. Therefore, we report here on the application of such a nanorhomb array on a quartz wafer biochip platform for DNA detection by fluorescence and SERS readout. By doing so, fluorescence microscopy allows for a fast detection of any positive or negative binding event within several seconds. Moreover SERS provides detailed molecular fingerprint information of fluorescence reporter molecules. This work contributes to the development of the more flexible usage of different optical detection schemes on the same chip surface.

Results and Discussion

The work presented in the following reports on the design and application of biosensors based on periodically patterned plasmonic arrays, which can be read out by both fluorescence and Raman spectroscopy, thus utilizing the unique sensitivity of fluorescence spectroscopy and the molecular selectivity of Raman spectroscopy. Therefore, chip surfaces with gold as the plasmonic material and with clearly defined arrays in the range of 200 × 200 μm^2 were fabricated. The number and position of the plasmonic arrays across the entire sensor chip can be adjusted to the particular research and application of interest. In Figure 1A, the SEM image of a section of the periodically patterned plasmonic array is depicted. Rhombic structures with interparticle distances of ~100 nm were fabricated on a quartz wafer. The size of the single rhomb-shaped gold nanoparticles of the plasmonic arrays used in this study was 50–240 nm along the short axis and 100–750 nm along the long axis. The shape and size of the nanoparticles of the plasmonic array define its optical properties.

In order to illustrate potential applications of these plasmonic arrays for bioanalytics, the arrays were tested for DNA detection. Therefore, capture oligonucleotides were immobilized on the chemically modified quartz surface between the gold nanorhombs. The nonspecific interaction of the DNA strands with the gold surface, through the nitrogen atoms of the DNA

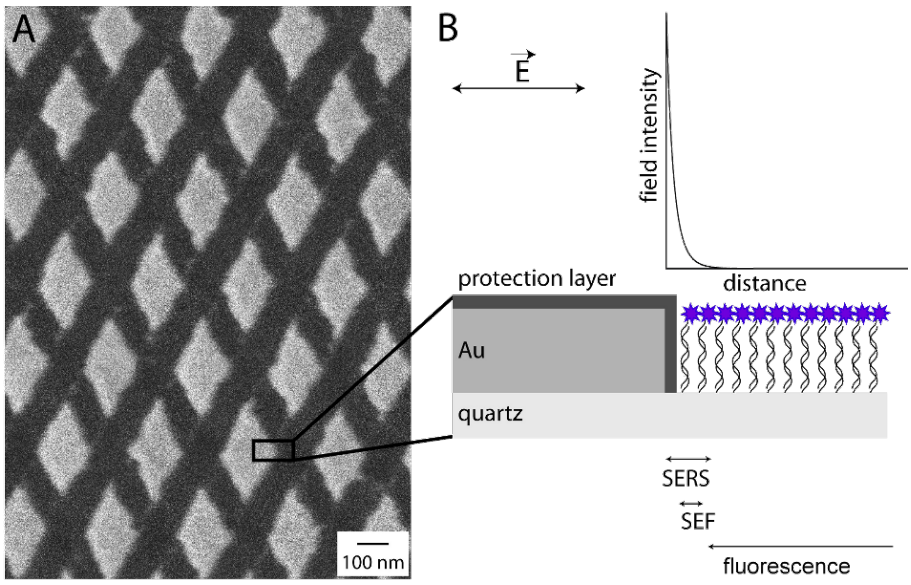

Figure 1: Schematic illustration of gold nanorhombs as plasmonic substrate. (A) The SEM image shows the periodically patterned gold surface. (B) Due to the interaction of the incident light with a metallic nanoparticle, surface plasmons are generated on the metal dielectric interface yielding a strong electromagnetic field with an evanescent decay on the nanoparticle surface. The strong electromagnetic field enhancement is employed for the effective enhancement of the Raman cross section (SERS) and the fluorescence (SEF), as indicating by the arrows.

bases, was prevented by the formation of an octanethiol SAM as a lipophilic protection layer. Dye-labeled target DNA was incubated on the chip surface and bound efficiently to the complementary capture sequences during the hybridization process. Figure 1B highlights the different readout methods, utilizing the properties of the periodically patterned plasmonic arrays. The excitation of localized surface plasmon resonances (LSPR) at the metal dielectric interface induces a strong electromagnetic field with evanescent decay on the metal surface. This strong field enhancement by the evanescent field can be employed for an effective enhancement of the weak Raman cross section (surface-enhanced Raman spectroscopy – SERS) [25] and also of the fluorescence signal (surface-enhanced fluorescence – SEF) [26]. However, the signal enhancement in SERS and SEF is characterized by different dependencies on the distance between the analyte and metal surface. In order to establish rules for an analyte–metal-surface, distance dependent, signal enhancement, scanning probe microscopy (SPM)-based measurements in combination with an optical readout were performed by several research groups: Roth et al. applied distance dependent tip-enhanced Raman spectroscopic (TERS) measurements, where SERS is combined with the SPM technique AFM (atomic force microscopy). These distance dependent TERS studies revealed that the highest signal intensities can be found for the smallest distance between tip and surface and moreover that the enhancement decays on a length scale of approximately 10 nm [27]. Furthermore, Anger et al. investigated the distance dependent enhancement of single-molecule fluorescence. The most efficient fluorescence enhancement was detected for distances in the range of 3–7 nm, whereas for shorter distances the molecular fluorescence was quenched [28]. Since the plasmonic behavior of a SPM probe for tip-enhanced near-field optical microscopy is comparable with that of a single metallic nanoparticle, the usage of periodically ordered plasmonic arrays should allow the application of SERS readout for molecule–metal surface distances up to 10 nm and SEF for analyte–metal distances of around 5 nm (Figure 1B). For distances of more than 20 nm the molecule remains more or less unaffected by the strong electromagnetic field enhancement, so normal fluorescence should be detectable.

In order to test the simultaneous application of fluorescence readout and SERS measurements on one common biochip platform, a DNA detection scheme based on the usage of a well-known fluorescence dye label (cyanine dye Cy3.5) was performed. In doing so, complementary and noncomplementary (here: negative control) capture DNA was immobilized on the sensor surface. Furthermore, the biochip was treated with dye-labeled target DNA, which binds to its complementary sequence. In a first test, fluorescence spectroscopy as one of the standard methods in bioanalytics was performed for a fast and easy control of the biochemical binding process: In the complementary case a bright fluorescence signal was detected, whereas under the same conditions no fluorescence signal was found for the noncomplementary case (Figure 2A). In order to gain more detailed information, SERS was employed as a readout tech-

nique for the same biosensor. The detected mean value SERS spectra, shown in Figure 2B, are dominated by contributions of the Cy3.5 label (see therefore the reference spectrum in [29]). The detected background signal, which can be attributed among others factors to the fluorescence emission of the dye, was subtracted from all SERS spectra for better visibility. An intense SERS signal of the reporter molecule Cy3.5 was detected due to the double helix formation in the complementary case. By insertion of mismatches within the DNA strand, the binding efficiency of the dye labeled target DNA and moreover the SERS signal was decreased for the noncomplementary case (Figure 2C). Thus, the established biosensor allowed the distinction between a complementary and a noncomplementary binding of target DNA through both a fluorescence and SERS detection scheme. This will be useful for the flexible usage of the same biochip platform in applying different detection schemes.

In order to achieve a maximum SERS enhancement, the excitation wavelength should lie within the plasmonic absorption. As shown in Figure 3A the optical transmission minimum at around 700 nm indicates the surface plasmon excitation along the short rhomb axis. Thus the Raman excitation wavelength of 633 nm is in resonance with the short wavelength tail of the plasmon band. However, the emitted Stokes Raman-scattered light of modes that are also in resonance with the surface plasmon will also be enhanced due to the plasmon resonance of the nanoantenna. This effect is described as the second part of the electromagnetic SERS mechanism [30,31]. Recently we [24] investigated this contribution of secondary emission enhancement to the overall SERS signal, utilizing the anisotropic character of gold nanorhomb arrays. Since the signal enhancement follows the plasmonic profile, fabrication strategies were developed for the vis and NIR spectral region. Here, the geometry of the gold nanorhombs was optimized by numerical calculations to efficiently improve the emission enhancement process. In Figure 3B a typical SERS spectrum is depicted for the complementary case concerning the capture and dye-labeled target DNA. The background-corrected fingerprint signature is dominated by contributions from the dye-label Cy3.5. In order to investigate the mismatch specificity of the binding process on the biochip surface, capture DNA was immobilized on the free quartz surface with the complementary sequence (NS150), one mismatch (NS151), three mismatches (NS153), and the noncomplementary sequence (N7), with respect to the Cy3.5-labeled target DNA. Figure 3C shows the Raman signal intensity of three prominent Raman modes, as determined by their peak areas. The mean values of the signal intensities are plotted for each of the tested capture DNA sequences. The largest signal intensities were found for the complementary case (NS150) due to the most specific interaction between the capture and target molecule. The Raman signal intensities for the mismatch (NS151, NS153) cases are lower than for the complementary (NS150) case, thus demonstrating the mismatch specificity of the used protocol. In addition, the signal intensity for the negative control (N7) is significantly lower than for the complementary case. Thus the established biochip is an appropriate tool for sequence specific SERS investigation and application to DNA analytics.

Due to the strong electromagnetic field enhancement, the fluorescence intensity of chromophores can also be enhanced in close vicinity to the metallic nanoparticles (SEF) [32,33]. In order to verify the amount of fluorescence signal enhancement

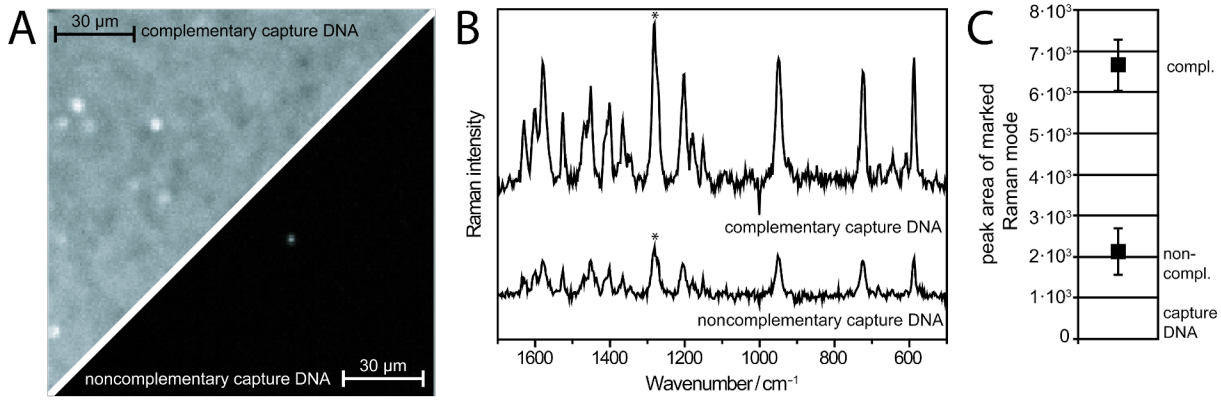

Figure 2: Application of the same plasmonic array for fluorescence and SERS readout. (A) Here, the fluorescence signal is shown in the upper-left and lower-right, for the complementary and noncomplementary capture and dye-labeled target DNA sequences, respectively. A bright fluorescence signal was detected for the complementary case due to the effective formation of the DNA double helix. (B) Raman signature (background-corrected mean value spectrum) of the Cy3.5 label, which is attached to the target DNA. (C) As more dye-labeled DNA molecules are attached to the surface in the complementary case, due to the double helix formation, the Raman signal is more intense.

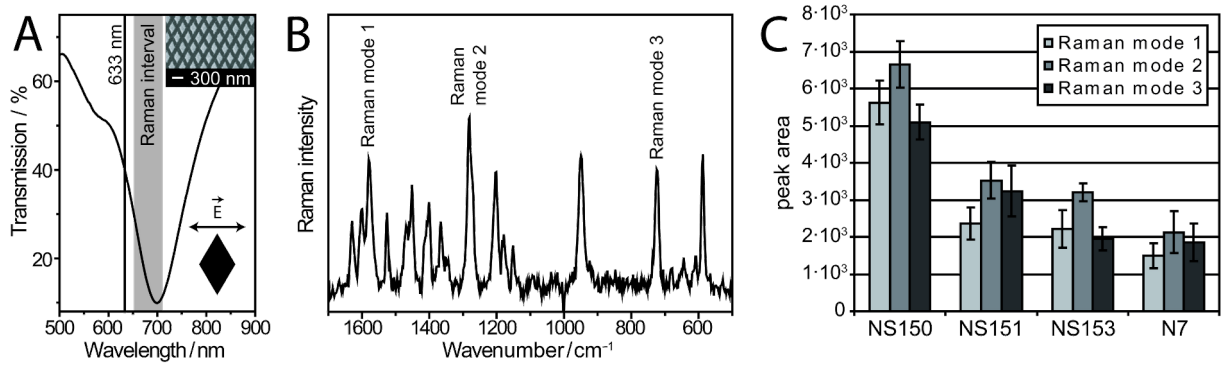

Figure 3: Mismatch-selective SERS investigation. (A) Transmission minimum at around 700 nm indicates the surface plasmon excitation along the short rhomb axis (inset: SEM image of periodically distributed nanorhombs). The excitation wavelength of 633 nm and the Raman interval matches the plasmonic profile. (B) The background-corrected Raman spectrum is dominated by contributions from the dye-label Cy3.5. The target DNA sequence is complementary to that of the capture DNA. (C) In order to illustrate the sequence-specific Raman intensity of three different Raman bands (marked in Fig. B), capture DNA with the complementary sequence (NS150), one mismatch (NS151), three mismatches (NS153), and the non-complementary sequence (N7) with respect to the Cy3.5-labeled target DNA were immobilized on the biochip surface. The strongest Raman signal intensity was detected for the complementary case, which indicates the efficient double helix formation.

that is due to coupling with a strong electromagnetic field, various plasmonic arrays were used for this study. The SEM images are depicted in Figure 4A. As mentioned above, the plasmonic samples were arrays of gold nanorhombs mounted on a quartz wafer, with interparticle distances in the range of 100 nm. The fluorescent dye was bound to DNA strands on the free quartz surface. Binding to the gold layer was hindered by a lipophilic protection layer. Thus the detected fluorescence intensity was strongly correlated with the area of free quartz surface per unit cell (Figure 4B). The lower the density of gold per unit cell, the higher the fluorescence intensity should be. Furthermore, the fluorescence enhancement is locally confined

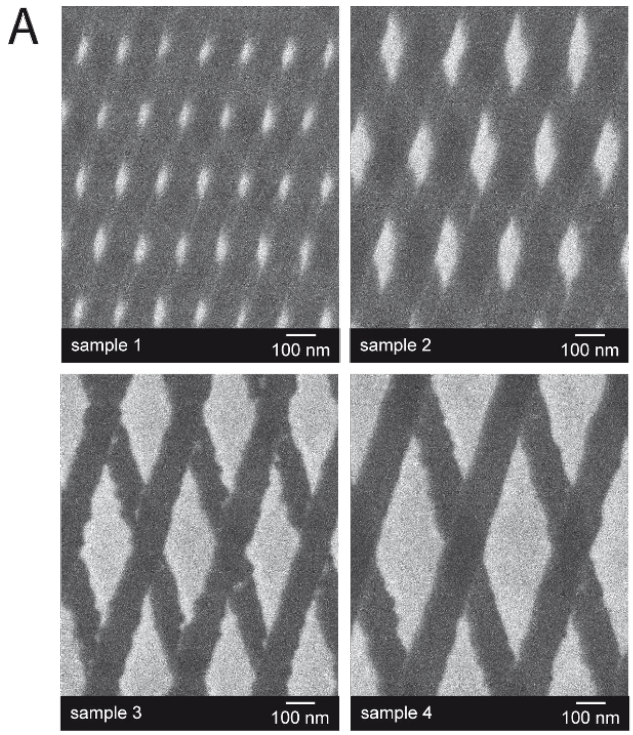

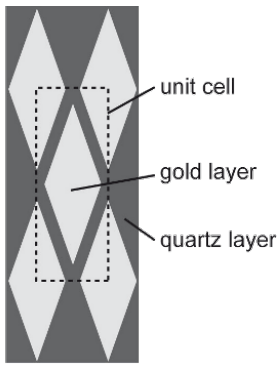

sample	free quartz surface [nm²] / unit cell [nm²]
1	0.9269
2	0.8639
3	0.6176
4	0.5934

Figure 4: Various plasmonic arrays, which were used for a fluorescence comparison study. (A) SEM images of the used plasmonic arrays illustrate the nanoparticle size and the interparticle distance, which is in the range of 100 nm. (B) Estimation of the free quartz surface area per unit cell.

to nanosized areas with strong electromagnetic field enhancement, which correspond to the edges of the short rhomb axis when using visible excitation wavelengths [22]. The perimeter of the nanorhomb plays no prominent role in the electromagnetic field enhancement. Due to the large distances between the gold nanoparticles, the fluorescence intensity of molecules bound on the quartz surface remains mainly unaffected by the excitation of the LSPR. Therefore, the detected fluorescence intensity was normalized with respect to the free quartz surface area per unit cell of the various plasmonic arrays.

Capture DNA was immobilized on the free quartz wafer. The dye-labeled target DNA bound to its complementary capture sequence. Thus, the formation of the DNA double helix was indicated by the fluorescence signal of the Cy3.5 label. The absorption and emission spectra of the fluorophore Cy3.5 and moreover the plasmonic profiles of the used gold nanorhomb arrays are depicted in Figure 5A for comparison. Since the various plasmonic arrays are characterized by a different size of the individual gold nanorhombs (Figure 4A), the transmission minimum, indicating the excitation of the LSPR, shifts to higher wavelengths with increasing size of the gold nanorhombs. Thus the LSPR peak overlaps with the absorption and emission spectra differently, which may have an influence on the fluorescence intensity. The normalized fluorescence intensity (detected fluorescence/free quartz surface area per unit cell, illustrated in Figure 5B) of sample 2 is surprisingly higher than that for the other plasmonic samples, whereas sample 3 and 4 exhibit comparable signal intensities. The observed fluorescence enhancement with sample 2 opens the way towards systematic SEF investigations with tunable plasmonic arrays. Furthermore, these results provide insight into the fluorescence enhancement mechanism. Due to the spectral overlap of the plasmonic profile with the absorption spectrum of the dye, an enhanced excitation rate may be reached. Thus the fluorescence intensity is enhanced because the fluorophore is excited more often [32]. This mechanism may be the explanation for the signal increase seen with sample 1 and 2 for fluorescence measurements of Cy3.5. A further contribution to SEF is described as an enhanced decay rate that improves the quantum yield of the fluorophore and decreases the lifetime, which should allow the fluorophore to undergo more excitation–de-excitation cycles before photobleaching occurs [26,32].

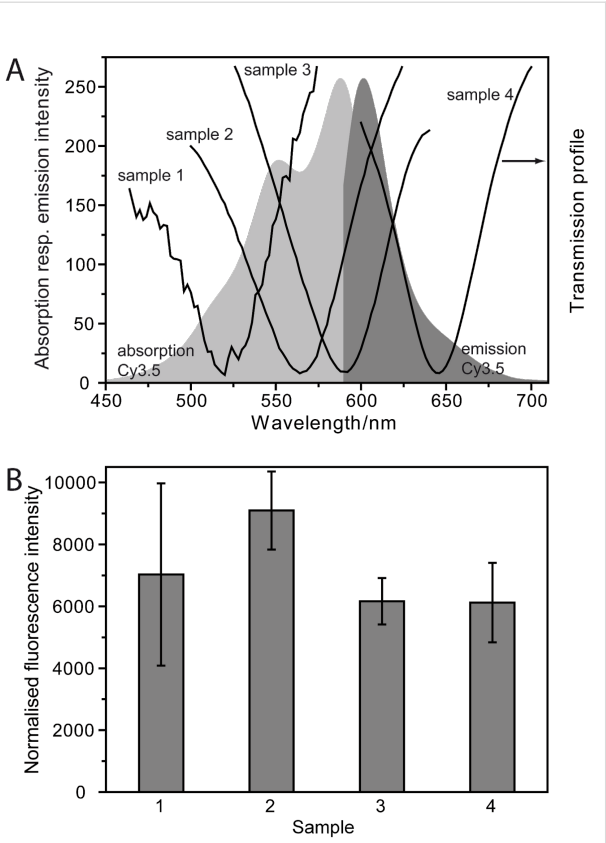

Figure 5: Observation of enhanced fluorescence intensity. (A) Absorption and emission spectrum of the dye-label Cy3.5, attached to a DNA strand, in comparison to the transmission spectra of various plasmonic arrays. The transmission minima (indicating the LSPR excitation) overlap with the absorption and emission spectra differently. (B) The detected fluorescence intensity is normalized with respect to the free quartz surface area per unit cell. The highest signal intensity was detected for sample 2, which may be attributed to a fluorescence enhancement mechanism.

Conclusion

In this paper, the application of a sensor platform employing fluorescence and SERS detection was introduced. Since the signal intensity is known to show a strong dependence on the distance between the molecules of interest and the metallic surface of the plasmonic active particle [27,28], an array of periodically patterned gold nanostructures mounted on a quartz wafer was preferred for these multimodal readout applications, due to the feasibility of binding molecules to the quartz layer, resulting in different distances to the metallic surface. In studying the example of a DNA detection scheme with a Cy3.5 dye label, fluorescence spectroscopy was applied, due to its fast detection time of several seconds, in order to detect the binding event of complementary DNA on the biochip surface. Additionally, SERS provides fingerprint information of the dye-label and the results illustrate the mismatch selectivity. By careful adjustment of the plasmonic behavior, the fluorescence intensity of the dye-label was significantly increased. As a result, the tuning of the optical behavior of plasmonic arrays allows studies of the fluorescence and SERS enhancement mechanism in future work. Finally, this study is a contribution towards the development of more flexible applications of the same biochip platform, through the performance of both fluorescence and SERS microscopy.

Experimental

Fabrication process of periodically patterned gold nanorhomb arrays. The geometry of the plasmonic array was optimized for maximum signal enhancement by finite element method (FEM) simulations (COMSOL Multiphysics). Periodically patterned SERS arrays were fabricated by means of electron beam lithography and Argon ion beam etching. Quartz wafer was coated with 20 nm of gold by vacuum evaporation, followed by spin-coating of a 120 nm thick PMMA (polymethyl methacrylate) resist layer onto the metal film. The resist layer was exposed by a commercial e-beam writer (LION LV-1, Vistec Electron Beam GmbH) operating at 20 keV. After the development in organic solvents (60 s in MIBK:IPA = 1:1 solution), the unprotected gold layer was removed by Argon ion beam etching. Finally, the entire process was completed with oxygen plasma cleaning. The fabrication process was described in detail previously [21-23,34]. Based on the concept of the crossed exposure of two gratings of lines in the resist layer, regularly patterned gold surfaces were produced. The gold surfaces were characterized by means of SEM and optical far-field transmission measurements (Lambda-950 Perkin Elmer).

Sample preparation (DNA immobilization). The regularly patterned gold nanorhomb arrays were treated with oxygen plasma under gentle conditions (35 W, 30 s) before usage. To prevent nonspecific interactions of the DNA strands with the metallic surface through the DNA bases, the plasmonic arrays were incubated in a 10 mM ethanolic solution of octanethiol, providing a lipophilic protection layer (here: Self assembled monolayer (SAM)) on the gold surface [35]. For the binding of the amino-modified capture DNA, the quartz surface was modified with 3-glycidyloxypropyl trimethoxysilane (GOPS) as described elsewhere [36]. The capture DNA (complementary sequence NS150: amino-link-5'-TTT TTT CAG CAT GTG CTC CTT GAT TCT ATG-3'; one mismatch sequence NS151: amino-link-5'-TTT TTT CAG CAT GGG CTC CTT GAT TCT ATG-3'; three mismatch sequence NS153: amino-link-5'-TTT TTT CAG CAT TAT CTC CTT GAT TCT ATG-3'; negative control N7 5'-ACT GAC TGA CTG ACT GAC TGA CTG GGC GGC GAC CT-3'-amino-link) was prepared as a 1 µM solution in 5× phosphate buffered saline (PBS). To deposit small volumes (here: 4 nL) of the capture DNA solution, a Nano-Plotter NP 2.0 (GeSiM mbH, Großerkmannsdorf, Germany) was used. After the drops dried up, the complete immobilization of the capture DNA strand was ensured by an UV linking process [37] (5 min at 254 nm). Finally, the chips were thoroughly washed to remove all unbound capture DNA. Before the hybridization, the dye-labeled target DNA (50 nM Cy3.5-labeled sequence: Cy3.5-5'-CAT AGA ATC AAG GAG CAC ATG CTG AAA AAA-3') was suspended in 5× saline–sodium citrate (SSC) and 0.1% sodium dodecyl sulphate (SDS). Droplets of approximately 10 µL of the target DNA were added onto the chip and incubated for 1 h at 40 °C in a humidity chamber. Afterwards, the substrates were washed for 5 min each in 2× SSC and 0.1% SDS, 2× SSC and 0.2× SSC. Finally, the chips were dried under a stream of nitrogen.

Fluorescence measurements. Fluorescence images were recorded by means of an Axio Imager A1m microscope with an AxioCam MRc5 camera (Carl Zeiss Jena GmbH, Germany). The correct settings of excitation and emission wavelength for the samples were realized by the special filter set 77HE (Carl Zeiss Jena GmbH, Germany), which contains a through-hole bandpass filter with specific excitation wavelengths in the range of 483 nm, 564 nm and 642 nm. Excitation and emission spectra of the fluorescent dye Cy3.5 were measured with a Jasco FP-6200 spectrofluorometer (JASCO Germany).

SERS set-up. The Raman spectra were recorded with a micro-Raman setup (HR LabRam invers, Jobin-Yvon-Horiba). The spectrometer has an entrance slit of 100 µm, a focal length of 800 mm, and is equipped with a 300 line mm^{-1} grating. The 633 nm line of a He–Ne laser (Coherent) with a laser power of ~600 µW incident on the sample was used for excitation. The Raman scattered light was detected by a CCD camera operating at 220 K. A Leica PLFluoar ×100 objective (NA 0.75) was used for focusing the laser light onto the samples (focus size ~1 µm) and collecting the Raman signal.

Acknowledgements

Funding of research project "Jenaer Biochip Initiative (JBCI)" within the framework "Unternehmen Region – InnoProfile" and "Photonic Nanomaterials (PhoNa)" within the framework "Spitzenforschung und Innovation in den Neuen Ländern" from the Federal Ministery of Education and Research, Germany (BMBF) is gratefully acknowledged. K. W. gratefully acknowledges financial support by "Carl-Zeiss-Stiftung". The authors thank Jörg Petschulat and Thomas Pertsch for providing the transmission spectra. Further, D.C. thanks Keiko Munechika, Yeechi Chen and David Ginger for helpful discussions during the stay at Ginger Research Lab (University of Washington) in summer 2009.

References

1. Weiss, S. *Science* **1999,** *283,* 1676–1683. doi:10.1126/science.283.5408.1676
2. Schena, M.; Shalon, D.; Davis, R. W.; Brown, P. O. *Science* **1995,** *270,* 467–470. doi:10.1126/science.270.5235.467
3. Braeckmans, K.; De Smedt, S. C.; Leblans, M.; Pauwels, R.; Demeester, J. *Nat. Rev. Drug Discovery* **2002,** *1,* 447–456. doi:10.1038/nrd817

4. Hering, K.; Cialla, D.; Ackermann, K.; Dörfer, T.; Möller, R.; Schneidewind, H.; Mattheis, R.; Fritzsche, W.; Rösch, P.; Popp, J. *Anal. Bioanal. Chem.* **2008,** *390,* 113–124. doi:10.1007/s00216-007-1667-3
5. Vo-Dinh, T.; Wang, H.-N.; Scaffidi, J. *J. Biophotonics* **2010,** *3,* 89–102. doi:10.1002/jbio.200910015
6. Geßner, R.; Rösch, P.; Petry, R.; Schmitt, M.; Strehle, M. A.; Kiefer, W.; Popp, J. *Analyst* **2004,** *129,* 1193–1199. doi:10.1039/b411690a
7. Ackermann, K. R.; Henkel, T.; Popp, J. *ChemPhysChem* **2007,** *8,* 2665–2670. doi:10.1002/cphc.200700554
8. Cialla, D.; Deckert-Gaudig, T.; Budich, C.; Laue, M.; Möller, R.; Naumann, D.; Deckert, V.; Popp, J. *J. Raman Spectrosc.* **2009,** *40,* 240–243. doi:10.1002/jrs.2123
9. Böhme, R.; Richter, M.; Cialla, D.; Rösch, P.; Deckert, V.; Popp, J. *J. Raman Spectrosc.* **2009,** *40,* 1452–1457. doi:10.1002/jrs.2433
10. Baia, M.; Baia, L.; Kiefer, W.; Popp, J. *J. Phys. Chem. B* **2004,** *108,* 17491–17496. doi:10.1021/jp047899h
11. Budich, C.; Neugebauer, U.; Popp, J.; Deckert, V. J. *Microsc.* **2008,** *229,* 533–539. doi:10.1111/j.1365-2818.2008.01939.x
12. März, A.; Ackermann, K. R.; Malsch, D.; Bocklitz, T.; Henkel, T.; Popp, J. *J. Biophotonics* **2009,** *2,* 232–242. doi:10.1002/jbio.200810069
13. Hering, K. K.; Möller, R.; Fritzsche, W.; Popp, J. *ChemPhysChem* **2008,** *9,* 867–872. doi:10.1002/cphc.200700591
14. Porter, M. D.; Lipert, R. J.; Siperko, L. M.; Wang, G.; Narayanan, R. *Chem. Soc. Rev.* **2008,** *37,* 1001–1011. doi:10.1039/b708461g
15. Haes, A. J.; Haynes, C. L.; McFarland, A. D.; Schatz, G. C.; Van Duyne, R. P.; Zou, S. *MRS Bull.* **2005,** *30,* 368–375. doi:10.1557/mrs2005.100
16. Baia, M.; Baia, L.; Astilean, S.; Popp, J. *Appl. Phys. Lett.* **2006,** *88,* 143121. doi:10.1063/1.2193778
17. Stropp, J.; Trachta, G.; Brehm, G.; Schneider, S. *J. Raman Spectrosc.* **2003,** *34,* 26–32. doi:10.1002/jrs.931
18. Baia, L.; Baia, M.; Popp, J.; Astilean, S. *J. Phys. Chem. B* **2006,** *110,* 23982–23986. doi:10.1021/jp064458k
19. Mahajan, S.; Baumberg, J. J.; Russell, A. E.; Bartlett, P. N. *Phys. Chem. Chem. Phys.* **2007,** *9,* 6016–6020. doi:10.1039/b712144j
20. Wells, S. M.; Retterer, S. D.; Oran, J. M.; Sepaniak, M. J. *ACS Nano* **2009,** *3,* 3845–3853. doi:10.1021/nn9010939
21. Huebner, U.; Boucher, R.; Schneidewind, H.; Cialla, D.; Popp, J. *Microelectron. Eng.* **2008,** *85,* 1792–1794. doi:10.1016/j.mee.2008.05.005
22. Cialla, D.; Siebert, R.; Hübner, U.; Möller, R.; Schneidewind, H.; Mattheis, R.; Petschulat, J.; Tünnermann, A.; Pertsch, T.; Dietzek, B.; Popp, J. *Anal. Bioanal. Chem.* **2009,** *394,* 1811–1818. doi:10.1007/s00216-009-2749-1
23. Petschulat, J.; Cialla, D.; Janunts, N.; Rockstuhl, C.; Hübner, U.; Möller, R.; Schneidewind, H.; Mattheis, R.; Popp, J.; Tünnermann, A.; Lederer, F.; Pertsch, T. *Opt. Express* **2010,** *18,* 4184–4197. doi:10.1364/OE.18.004184
24. Cialla, D.; Petschulat, J.; Hübner, U.; Schneidewind, H.; Zeisberger, M.; Mattheis, R.; Pertsch, T.; Schmitt, M.; Möller, R.; Popp, J. *ChemPhysChem* **2010,** *11,* 1918–1924. doi:10.1002/cphc.200901009
25. Lombardi, J. R.; Birke, R. L. *J. Phys. Chem. C* **2008,** *112,* 5605–5617. doi:10.1021/jp800167v
26. Lakowicz, J. R.; Geddes, C. D.; Gryczynski, I.; Malicka, J.; Gryczynski, Z.; Aslan, K.; Lukomska, J.; Matveeva, E.; Zhang, J.; Badugu, R.; Huang, J. *J. Fluoresc.* **2004,** *14,* 425–441. doi:10.1023/B:JOFL.0000031824.48401.5c
27. Roth, R. M.; Panoiu, N. C.; Adams, M. M.; Osgood, R. M.; Neacsu, C. C.; Raschke, M. B. *Opt. Express* **2006,** *14,* 2921–2931. doi:10.1364/OE.14.002921
28. Anger, P.; Bharadwaj, P.; Novotny, L. *Phys. Rev. Lett.* **2006,** *96,* 113002. doi:10.1103/PhysRevLett.96.113002
29. Cao, Y. C.; Jin, R.; Mirkin, C. A. *Science* **2002,** *297,* 1536–1540. doi:10.1126/science.297.5586.1536
30. Kerker, M.; Wang, D.-S.; Chew, H. *Appl. Opt.* **1980,** *19,* 4159–4174. doi:10.1364/AO.19.004159
31. Gersten, J.; Nitzan, A. *J. Chem. Phys.* **1980,** *73,* 3023–3037. doi:10.1063/1.440560
32. Chen, Y.; Munechika, K.; Ginger, D. S. *MRS Bull.* **2008,** *33,* 536–542. doi:10.1557/mrs2008.107
33. Chen, Y.; Munechika, K.; Ginger, D. S. *Nano Lett.* **2007,** *7,* 690–696. doi:10.1021/nl062795z
34. Cialla, D.; Hübner, U.; Schneidewind, H.; Möller, R.; Popp, J. *ChemPhysChem* **2008,** *9,* 758–762. doi:10.1002/cphc.200700705
35. Schwartz, D. K. *Annu. Rev. Phys. Chem.* **2001,** *52,* 107–137. doi:10.1146/annurev.physchem.52.1.107
36. Möller, R.; Schüler, T.; Günther, S.; Carlsohn, M. R.; Munder, T.; Fritzsche, W. *Appl. Microbiol. Biotechnol.* **2008,** *77,* 1181–1188. doi:10.1007/s00253-007-1241-0
37. Schüler, T.; Nykytenko, A.; Csaki, A.; Möller, R.; Fritzsche, W.; Popp, J. *Anal. Bioanal. Chem.* **2009,** *395,* 1097–1105. doi:10.1007/s00216-009-3045-9

License and Terms

The definitive version of this article is the electronic one which can be found at: doi:10.3762/bjnano.2.54

Beilstein Journal of Nanotechnology

Tip-enhanced Raman spectroscopic imaging of patterned thiol monolayers

Johannes Stadler, Thomas Schmid, Lothar Opilik, Phillip Kuhn, Petra S. Dittrich and Renato Zenobi*

Full Research Paper

Open Access

Address:
Department of Chemistry and Applied Biosciences, ETH Zurich, Wolfgang-Pauli-Strasse 10, HCI E 329, CH-8093 Zurich, Switzerland

Email:
Renato Zenobi* - zenobi@org.chem.ethz.ch

* Corresponding author

Keywords:
mercaptopyridine; microcontact printing; monolayer; spectroscopic imaging; tip-enhanced Raman spectroscopy

Beilstein J. Nanotechnol. **2011,** *2,* 509–515.
doi:10.3762/bjnano.2.55

Received: 16 March 2011
Accepted: 31 May 2011
Published: 30 August 2011

This article is part of the Thematic Series "Nanophotonics, nano-optics and nanospectroscopy".

Guest Editor: A. J. Meixner

Abstract

Full spectroscopic imaging by means of tip-enhanced Raman spectroscopy (TERS) was used to measure the distribution of two isomeric thiols (2-mercaptopyridine (2-PySH) and 4-mercaptopyridine (4-PySH)) in a self-assembled monolayer (SAM) on a gold surface. From a patterned sample created by microcontact printing, an image with full spectral information in every pixel was acquired. The spectroscopic data is in good agreement with the expected molecular distribution on the sample surface due to the microcontact printing process. Using specific marker bands at 1000 cm^{-1} for 2-PySH and 1100 cm^{-1} for 4-PySH, both isomers could be localized on the surface and semi-quantitative information was deduced from the band intensities. Even though nanometer size resolution information was not required, the large signal enhancement of TERS was employed here to detect a monolayer coverage of weakly scattering analytes that were not detectable with normal Raman spectroscopy, emphasizing the usefulness of TERS.

Introduction

The chemical characterization of surface adsorbates is of great interest in several areas of research. The composition of biological membranes or of artificially structured surfaces, used in molecular electronics, determines their properties as well as their function. However, characterization is difficult due to the small size and the low number of the molecules that comprise these structures. Most techniques such as nuclear magnetic resonance (NMR), infrared (IR) spectroscopy and Raman spectroscopy (RS) lack the necessary spatial resolution, while others such as scanning tunneling microscopy (STM) or scanning electron microscopy (SEM) do not provide enough chemical information. Furthermore, the limited quantity of analyte results in weak signals rendering characterization even more difficult. Ideally, information should be gathered with minimal distur-

bance of the molecules, which rules out any kind of labeling, and also emphasizes the need for an ambient pressure technique.

Tip-enhanced Raman spectroscopy (TERS) has been developed to obtain chemical information with very high spatial resolution [1-4], or chemical information from very few molecules, and in some cases even single molecules [5-7]. The technique uses a metal or metalized AFM/STM tip to confine the laser energy focused by a confocal microscope objective and to act as a "nano-torch" to locally excite molecules underneath it and enhance their Raman signals. Here an application of TERS is demonstrated which particularly exploits the signal enhancing effect anywhere on the sample surface. Due to the increased signal, TERS can detect small amounts of analyte in a short time, allowing acquisition of Raman images of a surface area covered with weakly scattering molecules. The information from such a Raman image was used here to chemically identify and localize two different thiol isomers in an inhomogeneous self-assembled monolayer (SAM). In this work the lateral resolution of TERS was not used to its full potential, but, by exploiting the signal enhancement, weak scatterers could be identified over a larger area.

Thiols are used for several purposes. They can form a very thin protective layer on metal surfaces [8] or can be employed in sensorics [9,10]. Moreover, thiols have been suggested as components in molecular electronics [11]. Thiols are commercially available in a wide chemical diversity and can easily be linked to a variety of (bio-)molecules using simple chemistry. Thus, they may be used to pattern and functionalize entire surfaces or certain surface areas. Here, selected areas on a gold surface were modified by a thiol and, in a second step, the remaining substrate was covered by a secondary thiol film. This type of surface can act as a basis for biosensors [12,13].

To produce patterned SAM structures on a gold surface, microcontact printing is the tool of choice. The technique originated in the lab of Whitesides in 1993 [14] and provides cheap, quick and easy access to patterned surfaces after the initial production of a microfabricated master that can be moulded multiple times to create stamps. The pattern on the surface allows us in a first step to check whether or not a patterned region can be discerned from the bare substrate using TERS. In a further step, the functionalization of the bare substrate with a secondary analyte shows, that two very similar analytes can be differentiated and localized.

For our experiments we chose 2- and 4-mercaptopyridine (2-PySH and 4-PySH), which have been used to modify electrode surfaces in protein electrochemistry [15]. In a non-destructive experiment, the spectral signature of both isomers was employed to map their distribution on the sample surface using TERS in a gap mode configuration. The term "gap mode" signifies the use of a metal tip for TERS in close proximity (<5 nm distance) to a metal surface with the analyte in between the two. In this geometry, a very strong, highly localized electromagnetic field is formed in the small gap between the metal tip and the substrate, leading to a strong signal enhancement and a well-localized signal source [16-20]. The extent of the enhancement and, along with that, the intensity of the measured Raman signal strongly depends on the tip–surface distance [5,21-23]. Fluctuations in the tip–sample distance can lead to considerable Raman intensity changes, thus flat gold films are an ideal substrate to minimize the STM feedback changes and distance related artifacts.

Previous studies on self-assembled thiol films were conducted using AFM [13], STM [15,24,25], XPS and Ellipsometry [26] as well as Raman spectroscopy [27,28]. Single point TERS experiments have already been presented by our group in a study of the spectral and binding properties of 4-PySH on gold [29]. By using TERS, the topography and the chemical composition of molecular monolayers can be measured simultaneously during Raman imaging with high lateral resolution, around 15 nm, as demonstrated for areas of less than 500 × 500 nm^2 [30]. As shown here, large sample areas can also be measured to gain information from coarser structures. Traditionally this is the scale where confocal Raman microscopy has its strengths, but due to the low signal intensity from molecular monolayers, an enhanced Raman technique is necessary to determine the chemical identity of the molecules. In surface-enhanced Raman spectroscopy (SERS) experiments (with a rough Ag film as a substrate, produced by vapor coating with randomly located enhancement hot-spots), the necessary enhancement can in principle be reached. An attempt was made to visualize the distribution of molecules using SERS, but this did not yield satisfactory results. However, the large signal-to-noise ratio in every pixel of a TERS image allows one to obtain enough information to distinguish a full monolayer from a few scattered molecules on the surface that contribute to the overall signal and thus allows the visualization of patterned monolayer structures.

In this article, we show that TERS can be used to image chemically heterogeneous surfaces without the need for labeling, even when the different adsorbates have very similar properties, i.e., a monolayer consisting of both 2-PySH and 4-PySH. With TERS, both isomers could be localized on the surface by their spectroscopic signature and approximate information on the surface coverage could be obtained from the intensity of characteristic marker bands within the spectra. Due to the strong

enhancement, this could even be done with a (sub-)monolayer of non-resonant molecules. Similarly to AFM and STM, TERS images could be acquired with different step sizes to gather information about objects or structures on the nanometer or micrometer scale.

Results and Discussion

Flat template-stripped gold thin films with a thickness of 60–200 nm on glass were used as substrates for the experiments and functionalized with thiols using micro contact printing (for details see the Experimental section). In a first step, the efficiency and coherence of the transferred 2-PySH thiol monolayer was investigated using AFM. Figure 1 shows height and phase images of two AFM scans. The 30 µm overview scan in Figure 1a shows a clear phase difference between the bare gold surface and the circular microcontact printed thiol covered areas. The corresponding height image in (b) exhibits a similar pattern, but the small elevations from the thiol layer are somewhat masked by the system's background noise. The enlarged 10 µm scan in (c) and (d) indicates a continuous smooth printing with few defects within the printed areas. The height signal now shows the elevation of the thiols a little more clearly, suggesting a step height <1 nm, in agreement with existing literature [31-33]. Due to the slight curvature of the underlying gold surface this value cannot be determined more exactly.

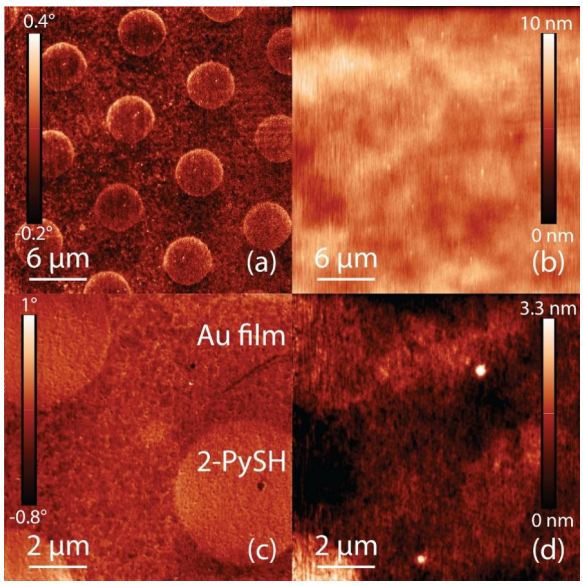

Figure 1: (a), (c) 30/10 µm AFM tapping mode phase images of microcontact printed 2-PySH on a gold surface. (b), (d) Corresponding height images showing slight elevation of the thiol layer, slightly masked by the system noise, suggesting a height between 0.5–1.0 nm. The phase image clearly illustrates the different surface properties of the printed thiol in comparison to the pure gold surface.

Attempts to spectroscopically visualize the thiol layer with confocal Raman spectroscopy failed due to the intrinsically weak cross section of the Raman process and the small number of molecules forming the investigated monolayer. No typical Raman bands were seen during excitation for 6 × 10 s at 3 mW by a 632.8 nm laser in confocal measurements. The absence of signals from decomposition products (carbonaceous decomposition products usually scatter strongly) leads to the conclusion that the SAM was not destroyed by the high laser power, but that the intensity of Raman signals from the intact monolayer was too weak to be detected.

In experiments on Ag SERS substrates (nominal thickness 6 nm), the printed patterns could not be detected and localized by confocal RS. Either no Raman signals at all or homogeneous signals from all over the substrate were detected (data not shown). Due to the strong but inhomogeneous enhancement by single sites on a typical SERS substrate, it is most likely that a very small fraction of molecules diffusing on the Ag surface during production of the samples dominated the spectra, preventing a localization of the molecules. Another possible explanation is that the roughness of the SERS substrate interfered with the patterning process used (compare Figure 6).

Results of a tip-enhanced Raman experiment are presented in Figure 2. An etched silver tip was used to probe the surface and enhance the Raman signals from the thiol monolayer. A 64 × 64 pixel map at 10 × 10 µm^2, with 156 nm/pixel, and full spectral information at every pixel, was acquired with a 632.8 nm laser at a power of 300 µW and an acquisition time of 2 s per spectrum. Figure 2a shows the intensity distribution of the 2-PySH marker band at 1000 cm^{-1} indicating the presence of 2-PySH on the surface. The circular structures from the microcontact printing can be seen clearly and distinguished from the pure metal background. The experiment did not destroy the thiol on the surface due to the low laser power and the non-contact nature of the STM. The AFM phase image in Figure 2b, taken after the TERS map from the same sample region, still shows the intact thiol patterns. Figure 2c shows a 120 s reference SERS spectrum of 2-PySH (blue, rescaled) and two 2 s TERS spectra from the positions indicated in (a), taken on the thiol layer (red, offset for clarity) and on the bare gold surface (black). The spectra clearly show the typical signals of the 2-PySH in the red curve and their absence in the black curve. The spectral background is caused by the Ag TERS tip.

A microcontact printed 2-PySH surface was then incubated in a 10 mM ethanolic solution of 4-PySH for 10 s, in order to fill the bare gold surfaces between the covered areas with 4-PySH. The result was a mixed monolayer of two thiols, with very similar

properties, distributed on the surface in a well-defined pattern. The AFM (a) phase and (b) topography images in Figure 3 demonstrate that it is not possible to differentiate the two isomers on the surface based on these AFM experiments alone, due to their similar surface properties (height, friction).

One possible but very tedious way to distinguish the two thiols would have been to use high resolution STM (which is usually size limited to the nanometer range) to search for typical molecular patterns in the SAM structure. However, both thiols can assemble in several different structures [15,24] and a possible mixing of both thiols would have led to further complications for STM. By using TERS imaging instead, and therefore gaining chemical contrast, the distribution of the two different thiols on the surface could be determined. Figure 4a and

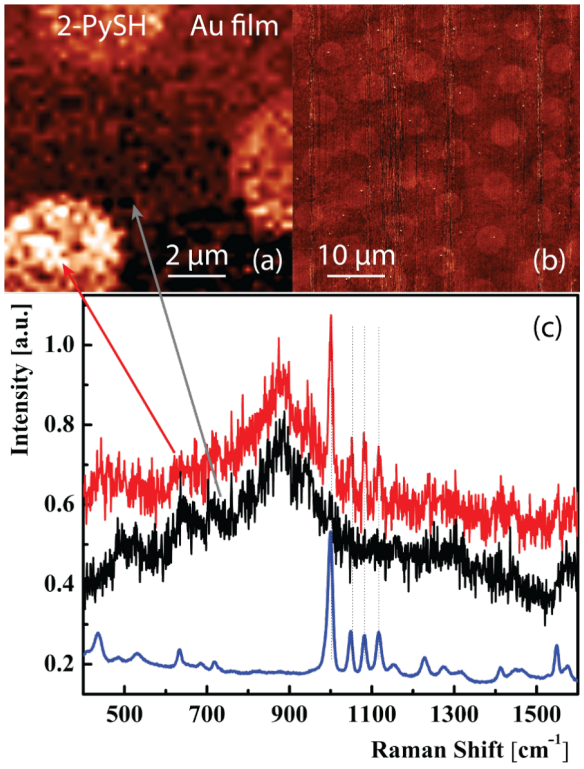

Figure 2: (a) 10 µm tip-enhanced spectroscopic image of microcontact printed 2-PySH on gold. Evaluation of a thiol marker band intensity at 1000 cm^{-1} yields a spot size of 5 µm with 4.1 µm spacings. (b) 50 µm phase image of the same area shows intact thiol structures after acquisition of the spectroscopic image in (a). (c) 120 s reference SERS spectrum of 2-PySH (blue) and 2 s TERS spectra from (a) on the thiol (red) and on the bare gold surface (black). Spectra have been offset (red) and rescaled (blue) for better visibility.

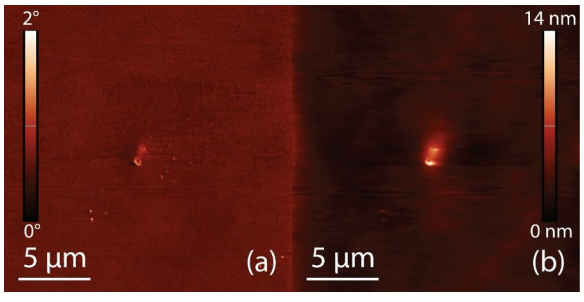

Figure 3: 20 µm tapping mode AFM image of microcontact printed 2-PySH on gold immersed in 4-PySH to fill gaps. (a) Phase image; (b) Topography – no discernible patterns on the surfaces between the two thiols can be seen. The roughness in (a) shows the typical topographic structure of the underlying gold film. The central feature originates from an impurity on the sample surface. The height of the image (excl. the central feature) is around 2 nm.

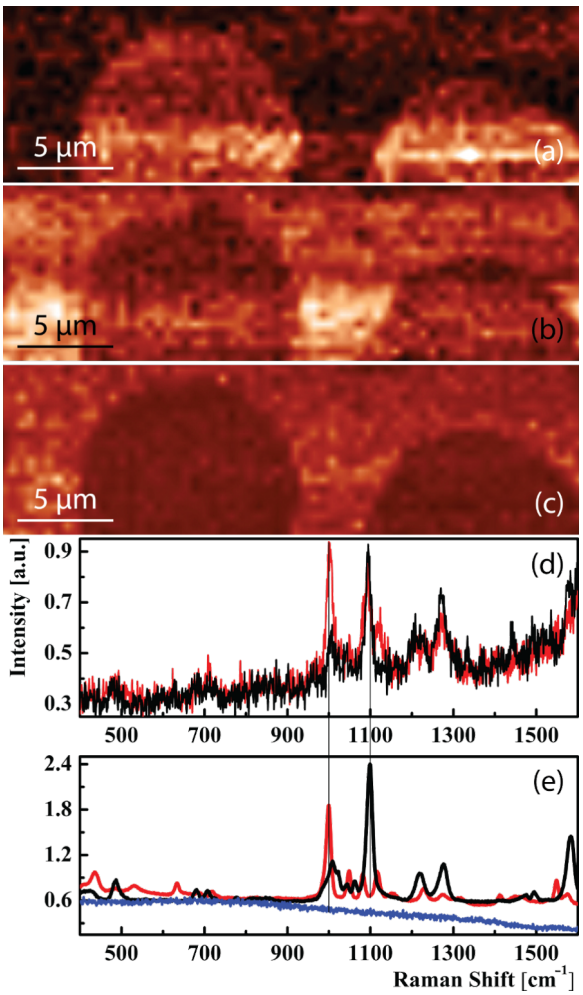

Figure 4: (a)–(c) 30 × 10 $µm^2$ tip-enhanced spectroscopic images. (a) Intensity of the 2-PySH marker band at 1000 cm^{-1}. (b) Intensity of the 4-PySH marker band at 1100 cm^{-1}. Images show complementary patterns with higher intensity of the microcontact printed thiol in the circles and higher intensity of the thiol used to fill the gaps around the circular areas. (c) Intensity ratio of the two marker bands. (d) 0.5 s TERS spectra from the printed 2-PySH area (red) and the area covered with 4-PySH (black). Small residues of 4-PySH in the red curve are visible at 1100 cm^{-1}. (e) 120 s reference SERS spectra from 2-PySH (red) and 10 s SERS spectrum of 4-PySH (black) and a 60 s confocal background spectrum (navy) from a 2-PySH thiol monolayer.

Figure 4b show the background corrected intensity maps of the 2-PySH and 4-PySH marker bands at 1000 cm^{-1} and 1100 cm^{-1}, respectively. To exclude the possibility that changes in enhancement during the experiment are responsible for the contrast (e.g., due to changes in tip–sample distance), the ratio between the two marker bands is also shown in Figure 4c. A reasonably uniform distribution within the printed areas and only weak fluctuations of this ratio in the filled areas can be seen. The evaluation shows that the printed thiol patterns have a diameter of 12 µm and a 3.5 µm spacing, in agreement with the 12 µm hexagon with a 55% coverage of circles on the microcontact printing stamp (see Experimental). Figure 4d shows 0.5 s TERS spectra from the printed 2-PySH area (red) and the area filled with 4-PySH (black). All bands from the black spectrum correspond well with bands in the black 10 s reference SERS spectrum from 4-PySH. The red TERS spectrum from 2-PySH exhibits all the bands from the 120 s reference SERS spectra from 2-PySH, and also an additional peak at 1100 cm^{-1} from the strongest band of 4-PySH. Considering that during preparation the entire sample is immersed in 4-PySH to fill the gaps from the microcontact printing, a certain amount of 4-PySH is expected to be embedded in the area printed with 2-PySH. Additionally, the 60 s confocal background spectrum (navy blue) from the 2-PySH thiol monolayer shows that the Raman signal of the monolayer is too weak to be picked up by a confocal measurement.

Conclusion

Full spectral imaging using TERS can be used to visualize the distribution of two very similar non-resonant thiols within a single monolayer on a gold film. Two isomeric thiol species were differentiated and localized on the sample surface using their spectroscopic signatures. The investigation of monolayers could be useful in the analysis of catalytic processes in heterogeneous catalysis [34], where the investigation of single active sites or the processes within a monolayer require signal enhancements from TERS combined with the ability to localize this enhancement on selected surface sites. The enhancement shown here can be conservatively estimated using the band intensity contrast between the confocal and the tip-enhanced case (<50 cts in 60 s confocally and 500 cts in 0.5 s for TERS), corrected by the area of origin known from previous experiments [30] (500 nm for confocal Raman and 25 nm in TERS), to be in the order of 10^5–10^6.

Experimental

All spectra were acquired by a combined AFM/STM connected to a quadruple grating Raman spectrometer (NTMDT Ntegra Spectra, Zelenograd, Russia) coupled to an EMCCD (Andor Newton, Belfast, UK). This top-illumination TERS setup has been described in detail in [30].

Template-stripped gold films were created using a similar method to that described in [35], by coating polished Si(100) wafers (Si-Mat, Landsberg, Germany) in a Bal-Tec Med 020 coating chamber at pressures below 1×10^{-5} mbar, with gold (99.99%, Leica, Wetzlar, Germany) evaporated by resistive heating at a rate ≤ 0.1 nm/s. The deposited gold film was bonded to clean microscope slide fragments using NOA61 (Norland, Cranbury, USA). The gold films were mechanically stripped from the Si wafers and used immediately.

STM was used to characterize the properties of the surface before sample preparation. The 10 × 10 $µm^2$ STM scan in Figure 5a shows that during evaporation of the gold, under the given conditions, flat flakes of around 500 nm were formed, as well as some single crystalline domains (seen in the top left and right central area). A more detailed 500 nm scan in Figure 5b reveals small surface corrugations on a well ordered crystalline patch from Figure 5a with an average roughness of <1 nm in height.

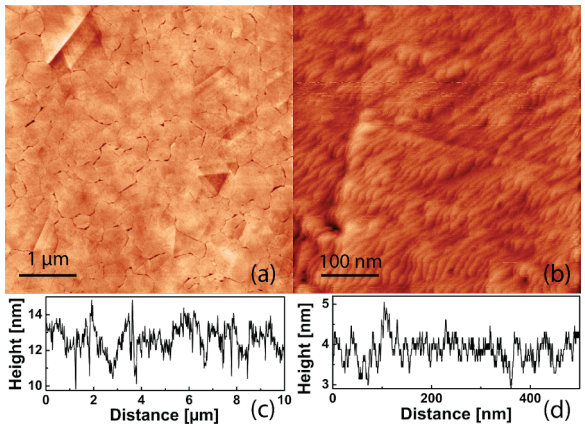

Figure 5: STM topography of a template-stripped gold surface (a) 10 × 10 $µm^2$ topography scan showing single crystalline gold areas (top left) and a typical grain size of around 0.5 µm. (b) 500 × 500 nm^2 image of the gold substrate showing slight corrugations. Line cuts (c) and (d) show peak-to-peak height differences of around 1–2 nm and a noise level below 1 nm.

Microcontact printing can be used to transfer a monolayer of thiols onto a noble metal substrate as described in [36,37]. A similar procedure to that described in [37] was used here to transfer a monolayer of 2-PySH onto the gold surface. To pattern the surface of the gold film, a microcontact printing stamp with differently sized elevated circles in hexagonal arrays was used (Figure 6). In Figure 6, a bright field image of the stamp layout is depicted. The stamp consists of an array of 650 µm wide hexagons, filled with flat circles of decreasing size (from top to bottom) and decreasing surface coverage (from left

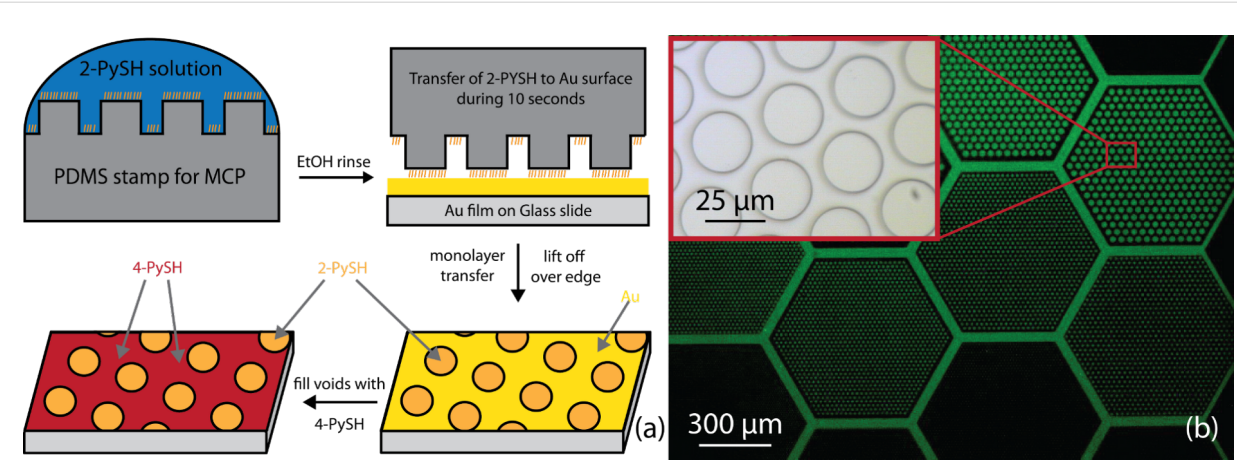

Figure 6: (a) Scheme of the microcontact printing process. Incubation of the stamp in ethanolic solution with subsequent printing on a template-stripped gold surface. (b) Magnified bright field image of a microcontact printing stamp for thiol deposition. The stamp consists of 650 µm hexagons filled with regular arrays of circles of different sizes and different distances between them. Circles from top to bottom have diameters of 25, 12 and 5 µm with increasing fill factors and distances from left to right. Inset: Magnified white light image from the circular elevations within a single hexagon.

to right). The height of the elevated features of the stamp is defined by the thickness of the photoresist on the master (2.1 ± 0.1 µm).

The master for microcontact printing stamps was fabricated by standard photolithography [14,38,39]. Briefly, a positive resist (AZ1518) was spin-coated to a height of 2.1 ± 0.1 µm onto a silicon wafer, exposed through a sub-micrometer resolution chrome mask and developed. After overnight silanization, poly(dimethylsiloxane) (PDMS) was mixed in a 10:1 ratio with curing agent, poured onto the master, degassed and cured in an oven at 80 °C overnight. The cured PDMS mould was cut into stamps.

For microcontact printing, a droplet of a 10 mM ethanolic solution of 2-PySH was placed on the stamp for 1 min, and washed with copious amounts of ethanol. The pattern was then printed onto the gold film by placing the stamp with the pressure of its own weight onto the gold film for 10 s followed by careful lift-off.

The filling of the bare gold areas by 4-PySH was achieved by covering the entire printed gold film with a 10 mM ethanolic solution for 10 s followed by thorough cleaning with ethanol.

TERS tips were fabricated by electrochemical etching of silver tips (99.99% Ag wire, 0.25 mm, Aldrich) similarly to [20,40] in a solution of 1:1 to 1:2 (v:v) of perchloric acid (Riedel de Häen)/methanol with an etching voltage of 8 V. After etching, tips were rinsed with methanol to remove residues of the etchant. Etched tips were produced shortly before the experiments, and exposure to ambient conditions did not exceed 4 h. Tips with suitable shape for STM scanning as well as TERS activity were chosen by visual inspection under a 360× stereo microscope (Nikon, Amstelveen, Netherlands).

For the TERS experiments, tips were carefully approached to the sample and checked for Raman activity using a 632.8 nm Helium–Neon laser. Selected tips were then aligned using the laser scanning mirrors [30] and subsequently used for TERS mappings. For each TERS map, laser power and exposure time per spectrum were adapted according to the enhancement of the tip and the activity of the analyte. The laser power used ranged between 0.1–2.0 mW and collection times of 0.1–2.0 s per spectrum were chosen to yield a sufficient signal-to-noise ratio for the investigated Raman bands. Each pixel in the TERS experiments corresponds to one spectrum from an area of roughly 25 nm in diameter. In measurements with larger pixel to pixel distances, only the probed area contributed to the respective Raman spectrum.

References

1. Anderson, N.; Hartschuh, A.; Novotny, L. *Nano Lett.* **2007,** *7,* 577–582. doi:10.1021/nl0622496
2. Steidtner, J.; Pettinger, B. *Phys. Rev. Lett.* **2008,** *100,* 236101. doi:10.1103/PhysRevLett.100.236101
3. Tarun, A.; Hayazawa, N.; Motohashi, M.; Kawata, S. *Rev. Sci. Instrum.* **2008,** *79,* 013706. doi:10.1063/1.2832347
4. Hartschuh, A.; Qian, H.; Georgi, C.; Bohmler, M.; Novotny, L. *Anal. Bioanal. Chem.* **2009,** *394,* 1787–1795. doi:10.1007/s00216-009-2827-4
5. Neacsu, C. C.; Dreyer, J.; Behr, N.; Raschke, M. B. *Phys. Rev. B* **2006,** *73,* 193406. doi:10.1103/PhysRevB.73.193406
6. Zhang, W. H.; Yeo, B. S.; Schmid, T.; Zenobi, R. *J. Phys. Chem. C* **2007,** *111,* 1733–1738. doi:10.1021/jp064740r

7. Domke, K. F.; Zhang, D.; Pettinger, B. *J. Am. Chem. Soc.* **2006,** *128,* 14721–14727. doi:10.1021/ja065820b
8. Hassan, N.; Holze, R. *J. Chem. Sci.* **2009,** *121,* 693–701. doi:10.1007/s12039-009-0083-y
9. Wink, T.; van Zuilen, S. J.; Bult, A.; van Bennekom, W. P. *Analyst (Cambridge, U. K.)* **1997,** *122,* 43R–50R. doi:10.1039/A606964I
10. Tlili, A.; Abdelghani, A.; Hleli, S.; Maaref, M. *Sensors* **2004,** *4,* 105–114. doi:10.3390/s40670105
11. Nørgaard, K.; Brøndsted Nielsen, M.; Bjørnholm, T. Thiol End-capped Molecules for Molecular Electronics: Synthetic Methods, Molecular Junctions and Structure-Property Relationships. In *Functional Organic Materials: Syntheses, Strategies and Applications;* Müller, J. J.; Bunz, U. H. F., Eds.; Wiley-VCH: Weinheim, Germany, 2007. doi:10.1002/9783527610266.ch10
12. Nyquist, R. M.; Eberhardt, A. S.; Silks, L. A.; Li, Z.; Yang, X.; Swanson, B. I. *Langmuir* **2000,** *16,* 1793–1800. doi:10.1021/la990018r
13. Caballero, D.; Pla-Roca, M.; Bessueille, F.; Mills, C. A.; Samitier, J.; Errachid, A. *Anal. Lett.* **2006,** *39,* 1721–1734. doi:10.1080/00032710600714014
14. Kumar, A.; Whitesides, G. M. *Appl. Phys. Lett.* **1993,** *63,* 2002–2004. doi:10.1063/1.110628
15. Umemura, K.; Fujita, K.; Ishida, T.; Hara, M.; Sasabe, H.; Knoll, W. *Jpn. J. Appl. Phys., Part 1* **1998,** *37,* 3620–3625. doi:10.1143/JJAP.37.3620
16. Geshev, P. I.; Dickmann, K. *J. Opt. A: Pure Appl. Opt.* **2006,** *8,* S161–S173. doi:10.1088/1464-4258/8/4/S17
17. Novotny, L.; Bian, R. X.; Xie, X. S. *Phys. Rev. Lett.* **1997,** *79,* 645–648. doi:10.1103/PhysRevLett.79.645
18. Demming, A. L.; Festy, F.; Richards, D. *J. Chem. Phys.* **2005,** *122,* 184716. doi:10.1063/1.1896356
19. Roth, R. M.; Panoiu, N. C.; Adams, M. M.; Osgood, R. M.; Neacsu, C. C.; Raschke, M. B. *Opt. Express* **2006,** *14,* 2921–2931. doi:10.1364/OE.14.002921
20. Ibe, J. P.; Bey, J. P. P.; Brandow, S. L.; Brizzolara, R. A.; Burnham, N. A.; DiLella, D. P.; Lee, K. P.; Marrian, C. R. K.; Colton, R. J. *J. Vac. Sci. Technol., A* **1990,** *8,* 3570–3575. doi:10.1116/1.576509
21. Raschke, M. B.; Lienau, C. *Appl. Phys. Lett.* **2003,** *83,* 5089–5091. doi:10.1063/1.1632023
22. Domke, K. F. Tip-enhanced Raman spectroscopy - Topographic and chemical information on the nanoscale. Ph.D. Thesis, FU Berlin, Germany, 2006.
23. Pettinger, B.; Domke, K. F.; Zhang, D.; Schuster, R.; Ertl, G. *Phys. Rev. B* **2007,** *76,* 113409. doi:10.1103/PhysRevB.76.113409
24. Jin, Q.; Rodriguez, J. A.; Li, C. Z.; Darici, Y.; Tao, N. J. *Surf. Sci.* **1999,** *425,* 101–111. doi:10.1016/S0039-6028(99)00195-8
25. Ferreira, Q.; Brotas, G.; Alcacer, L.; Morgado, J. Characterization of self-assembled monolayers of thiols on gold using scanning tunneling microscopy. In *Proceedings of the 7th Conference on Telecommunications,* 2009.
26. Prato, M.; Moroni, R.; Bisio, F.; Rolandi, R.; Mattera, L.; Cavalleri, O.; Canepa, M. *J. Phys. Chem. C* **2008,** *112,* 3899–3906. doi:10.1021/jp711194s
27. Yu, H. Z.; Xia, N.; Liu, Z. F. *Anal. Chem.* **1999,** *71,* 1354–1358. doi:10.1021/ac981131+
28. Picardi, G.; Chaigneau, M.; Ossikovski, R.; Licitra, C.; Delapierre, G. *J. Raman Spectrosc.* **2009,** *40,* 1407–1412. doi:10.1002/jrs.2362
29. Zhang, W. H.; Schmid, T.; Yeo, B. S.; Zenobi, R. *Isr. J. Chem.* **2007,** *47,* 177–184. doi:10.1560/IJC.47.2.177
30. Stadler, J.; Schmid, T.; Zenobi, R. *Nano Lett.* **2010,** *10,* 4514–4520. doi:10.1021/nl102423m
31. Huang, L.; Chang, Y.-H.; Kakkassery, J. J.; Mirkin, C. A. *J. Phys. Chem. B* **2006,** *110,* 20756–20758. doi:10.1021/jp065404d
32. Koslowski, B.; Tschetschetkin, A.; Maurer, N.; Ziemann, P. *Phys. Chem. Chem. Phys.* **2011,** *13,* 4045–4050. doi:10.1039/c0cp02162h
33. Kucera, J.; Gross, A. *Langmuir* **2008,** *24,* 13985–13992. doi:10.1021/la802368j
34. Domke, K. F.; Pettinger, B. *ChemPhysChem* **2010,** *11,* 1365–1373. doi:10.1002/cphc.200900975
35. Hegner, M.; Wagner, P.; Semenza, G. *Surf. Sci.* **1993,** *291,* 39–46. doi:10.1016/0039-6028(93)91474-4
36. Larsen, N. B.; Biebuyck, H.; Delamarche, E.; Michel, B. *J. Am. Chem. Soc.* **1997,** *119,* 3017–3026. doi:10.1021/ja964090c
37. Delamarche, E.; Schmid, H.; Bietsch, A.; Larsen, N. B.; Rothuizen, H.; Michel, B.; Biebuyck, H. *J. Phys. Chem. B* **1998,** *102,* 3324–3334. doi:10.1021/jp980556x
38. Xia, Y. N.; Whitesides, G. M. *Annu. Rev. Mater. Sci.* **1998,** *28,* 153–184. doi:10.1146/annurev.matsci.28.1.153
39. Qin, D.; Xia, Y.; Whitesides, G. M. *Nat. Protoc.* **2010,** *5,* 491–502. doi:10.1038/nprot.2009.234
40. Zhang, W. H.; Cui, X. D.; Yeo, B. S.; Schmid, T.; Hafner, C.; Zenobi, R. *Nano Lett.* **2007,** *7,* 1401–1405. doi:10.1021/nl070616n

License and Terms

Beilstein Journal of Nanotechnology

Room temperature excitation spectroscopy of single quantum dots

Christian Blum[1,§], Frank Schleifenbaum[2,§], Martijn Stopel[1], Sébastien Peter[2], Marcus Sackrow[3,4], Vinod Subramaniam[*1] and Alfred J. Meixner[*3]

Full Research Paper

Open Access

Address:
[1]Nanobiophysics Group and MESA+ Institute for Nanotechnology, University of Twente, PO Box 217, 7500 AE Enschede, The Netherlands, [2]Center for Plant Molecular Biology, Biophysical Chemistry, University of Tübingen, Auf der Morgenstelle 18, 72076 Tübingen, Germany, [3]Institut für Physikalische und Theoretische Chemie, University of Tübingen, Auf der Morgenstelle 8, 72076 Tübingen, Germany and [4]present address: Picoquant GmbH, Rudower Chaussee 29, 12489 Berlin, Germany

Email:
Vinod Subramaniam[*] - v.subramaniam@utwente.nl;
Alfred J. Meixner[*] - alfred.meixner@uni-tuebingen.de

* Corresponding author
§ CB and FS contributed equally to the work

Keywords:
blinking; excitation spectrum; quantum dots; single molecule spectroscopy; supercontinuum laser

Beilstein J. Nanotechnol. **2011,** *2,* 516–524.
doi:10.3762/bjnano.2.56

Received: 22 April 2011
Accepted: 09 June 2011
Published: 30 August 2011

This article is part of the Thematic Series "Nanophotonics, nano-optics and nanospectroscopy".

Guest Editor: A. J. Meixner

Abstract

We report a single molecule detection scheme to investigate excitation spectra of single emitters at room temperature. We demonstrate the potential of single emitter photoluminescence excitation spectroscopy by recording excitation spectra of single CdSe nanocrystals over a wide spectral range of 100 nm. The spectra exhibit emission intermittency, characteristic of single emitters. We observe large variations in the spectra close to the band edge, which represent the individual heterogeneity of the observed quantum dots. We also find specific excitation wavelengths for which the single quantum dots analyzed show an increased propensity for a transition to a long-lived dark state. We expect that the additional capability of recording excitation spectra at room temperature from single emitters will enable insights into the photophysics of emitters that so far have remained inaccessible.

Introduction

Since the first demonstration of single molecule fluorescence spectroscopy over two decades ago, techniques to detect and characterize the emission from single emitters have become increasingly sophisticated and versatile. These developments have made optical single molecule spectroscopy an indispensable tool to address complex problems in chemistry [1-3], in material sciences [4-6], and in life sciences [7-11].

A number of parameters that characterize single molecule emission are now routinely accessible at ambient temperatures, including emission intensity and polarization [12,13], fluorescence lifetime [14-16], and the emission spectrum [17-19]. Access to these parameters yields unique insights into distinct properties of single molecules, and enables the determination of the distributions of the relevant experimental parameters, revealing, for example, distinct sub-states and energetic levels in a heterogeneous population [20,21]. Furthermore, external tailoring or directing of molecular emission has also been reported [22-24].

However, a detailed study of frequency resolved excitation dependent processes at the single molecule level, at room temperature, has not been experimentally achievable so far. Appreciation of these processes is fundamentally important for the understanding of the basic physics and for applications in next-generation photonic devices. The primary challenge has been the intrinsic difficulty in measuring the absorption of a single emitter at room temperature due to the extremely low signal to noise ratio. Although recent reports have demonstrated the detection of single molecule absorbance [25-27], a complete single molecule absorbance spectrum at room temperature has not yet been reported. A complementary approach to access the frequency dependent coupling of an emitter to an external electromagnetic field is based on photoluminescence excitation spectroscopy. Single emitter photoluminescence excitation microscopy has been already achieved in the early days of single molecule detection, but has been limited to experiments at cryogenic temperatures where the linewidths of individual emitters are not inhomogeneously broadened [28,29]. Hence, only a very limited excitation wavelength range was required to resolve individual absorbance properties of a single emitter at low temperatures.

In this paper, we describe the first successful acquisition of single emitter excitation spectra under ambient conditions over a wide spectral range. We combine a tunable white-light laser source with a confocal microscope with single molecule detection sensitivity to demonstrate excitation spectra of isolated semiconductor nanocrystals. These fluorophores, often referred to as quantum dots, have unique optical properties [30-35], including a narrow and tailored luminescence emission spectrum and significantly enhanced photostability compared to organic fluorophores. These properties make quantum dots promising nanomaterials in various fields of research, ranging from in vivo probes in the life-sciences [10,36,37] to single photon light sources in telecommunications [38] or quantum computing [30,35]. We demonstrate here how single emitter excitation spectroscopy provides a valuable addition to the range of single emitter spectroscopy techniques, yielding new insights into the complex photophysics of quantum dots.

The excitation spectrum, commonly used in ensemble fluorescence spectroscopy, depicts the evolution of the emission intensity recorded in a fixed spectral detection window upon scanning the excitation wavelength. Moreover, the excitation spectrum of an emitter coincides with its absorbance spectrum if the quantum efficiency is independent of excitation wavelength, which is generally assumed to be true for most emitters over large wavelength ranges. Hence, measurement of the excitation spectra of individual quantum dots permits access to the individual absorbance properties that are not accessible by common single molecule techniques or not at all by ensemble approaches.

Results and Discussion

In this study, we recorded excitation spectra of 48 individual CdSe/ZnS core–shell quantum dots at room temperature. Since the occurrence of emission intermittencies (blinking) is a clear indication for the observation of a single emitter, and because blinking of quantum dots is still not fully understood, we did not apply any measures to suppress or minimize blinking. The single quantum dot excitation spectra recorded exhibited the main characteristics of a declining slope from shorter to longer wavelengths, and a peak close to the band edge transition, which we identify as the $1S(e)$-$2S_{3/2}(h)$ transition [39]. However, we find distinct differences in the individual spectra that can be attributed to individual photophysical properties of the analyzed single quantum dots as well as to the well-known transitions of single emitters to dark, non-emitting, states. A typical example of an excitation spectrum obtained from a single quantum dot is shown in Figure 1a. In contrast to the ensemble spectrum, we observed distinct dips and gaps in the single quantum dot excitation spectra, which in principle could either result from blinking or reflect the photophysical properties of the quantum dot.

Semiconductor quantum dots exhibit a discrete structure of quantized energy states. Hence, one would expect to observe discrete bands in both the excitation and absorbance spectra when the excitation wavelength is in resonance with a transition to such a discrete state. Low temperature experiments showed narrow emission lines [40], but also revealed that only a few sharp transitions in the direct vicinity of the band edge can be found, while at higher excitation energies the optical transitions merge into a dense quasicontinuum [41]. At room temperature, these sharp transitions experience inhomogeneous broadening effects, mainly due to lattice vibrations. It is therefore not surprising that no sharp transitions are resolved in the room temperature ensemble excitation spectra of quantum dots.

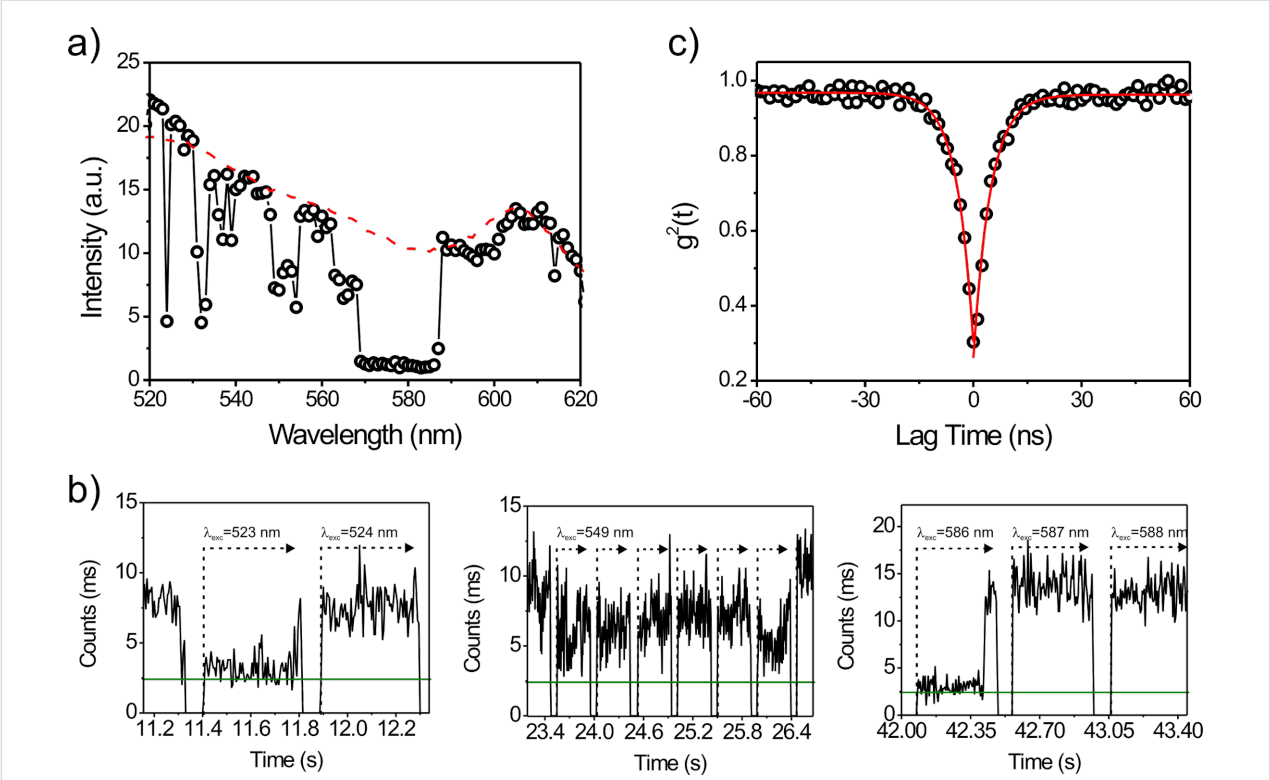

Figure 1: Single emitter characteristics observed by excitation spectroscopy of isolated quantum dots. a) Excitation spectrum of a single quantum dot (open circles) with typical intensity intermittencies that result in drops and gaps in the spectrum. The ensemble excitation spectrum is shown for comparison (red dashed line). b) Intensity trajectories of a single quantum dot for selected excitation wavelengths (green line marks the background level). c) Photon antibunching curve of a single quantum dot.

The spectra demonstrate obvious intensity fluctuations of different magnitudes within a single measurement interval, which are characteristic of the emission from a single emitter. These fluctuations have been reported for semiconductor quantum dots, and have only recently been circumvented in exceptional cases [42-44]. The intensity blinking of the quantum dot can be visualized from the intensity trajectories that were recorded with a temporal resolution of 5 ms (Figure 1b). The breaks to true zero between trajectories are instrument-related, and indicate the change of the excitation wavelength, while the green line marks the background signal level without quantum dot emission, attributed to the emitter being trapped in a dark state.

Clearly, these drops to the background level are not related to narrow absorbance lines due to the band structure of the semiconductor quantum dots. In this case, drops in the recorded intensity would result in excitation wavelengths for which no emission can be recorded. The start and end of such a dark interval would then have to coincide with the start of a new excitation wavelength recording interval. We did not observe this behavior and the beginning and end of a dark period occurred stochastically.

The left panel of Figure 1b depicts the intensity evolution for excitation from 522–524 nm. For these wavelengths, the excitation spectrum showed strong intensity fluctuations. At λ_{ex} = 522 nm, an intensity jump was observed immediately before the subsequent wavelength change. For λ_{ex} = 523 nm, the quantum dot was still in a non-emitting off-state, indicated by the signal intensity being at the background level. After 11.8 s it returned into a stable on-state after some initial short "bursts". Accordingly, transitions to short lasting off-states resulted in sudden dips in the excitation spectrum, and the intensity in the excitation spectrum did not drop to the background level, as the quantum dot was not dark during the whole integration interval.

The middle panel in Figure 1b depicts a decreased emission intensity that varied over time but did not drop to the background level. These variations in the observed emission intensity can be explained either as the result of fast blinking, below the time resolution of the experiment, or by transitions of the quantum dot to a dim (weakly-emitting) state [45]. As a result of this reduced emission we observed drops in the excitation spectrum over a number of wavelengths as can be seen around 550 nm in Figure 1a. Finally, we often found extended gaps in

the excitation spectrum of single quantum dots as can be seen in the spectrum between 569 nm and 587 nm (Figure 1a). This gap in the excitation spectrum is attributed to a long lasting dark state followed by the return to an emitting state as can be seen in the right panel of Figure 1b. It is important to note that the observed drops in intensity do not correlate with changes in the excitation wavelength. Clearly, the observed drops and gaps in the spectrum would vanish if exclusively emitting states were sampled for each excitation wavelength. For detection intervals where a transition to or from a dark state occurred (e.g., Figure 1b, right panel) this correction can easily be performed by considering just the higher emission intensity level. Drops and gaps in the spectrum originating from dim states or very fast transitions below the sampling resolution, and from long lasting dark states longer than the integration time per excitation wavelength, could be avoided by repeated, possibly faster, scanning of the excitation wavelength, which requires further technical development for implementation in future studies.

We argue that the observed transitions between on- and off-states reflect the intrinsic emission characteristics inherent to individual quantum dots. In addition to the intensity blinking observed, we further confirmed that we were addressing a single emitter and thus single photons by analyzing the coincidence of detected photons in time using a Hanbury Brown and Twiss configuration [46]. The resulting photon-antibunching curves recorded in this manner exhibited a near zero correlation ($g^2 = 0.3$) for the detection of two photons at the same time, as shown for a typical example in Figure 1c. Photon-antibunching data give strong evidence for the observation of single emitters [47], since a single emitting system intrinsically cannot emit two photons at the same time. Generally, g^2 values below 0.5 are accepted as a proof of single molecule observation [34].

The recorded spectra show varying degrees of blinking, ranging from spectra exhibiting almost no dips and gaps due to emission intermittencies (Figure 2a), to spectra where numerous transitions between emitting and dark states can be observed (Figure 2b–d). The excitation spectrum shown in Figure 2a is very intense and shows only minor signs of blinking, and is based on the detection of ~$2 \cdot 10^5$ photons emitted from the sampled quantum dot. This number of detected photons is comparable to the average number of photons that can be detected from organic fluorophores [48,49] and suggests that single emitter excitation spectroscopy could also be used for classes of emitters other than the very photostable quantum dots analyzed in this study.

The recorded data further enables the detailed analysis of the influence of the excitation wavelength on the blinking of single quantum dots. Numerous studies on single quantum dots have shown complicated luminescence intermittency, or blinking, with power law statistics over many decades in time. In most of these studies a single excitation wavelength was used, and only recently has the first in-depth investigation of quantum dot

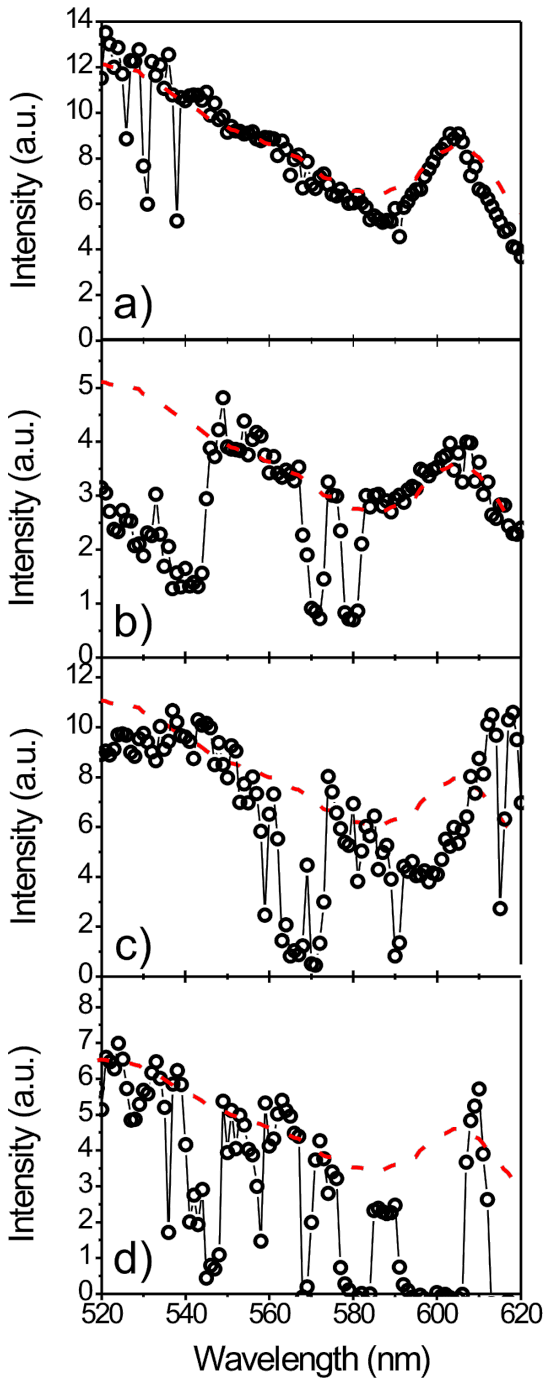

Figure 2: Single QD photoluminescence excitation spectra. For comparison, the ensemble excitation spectrum is shown as the red dashed line. The spectra show varying degrees of emission intermittencies visible as drops and gaps in the spectra. Especially in the wavelength region of the pronounced 1S(e)-2$S_{3/2}$(h) transition the spectra show distinct differences between different quantum dots, reflecting the individual nature of each quantum dot.

blinking comparing a small number of different excitation wavelengths been published [32]. These studies were based on the statistical analysis of different quantum dots and an analysis of the emission of individual emitters using different excitation wavelengths has not yet been achieved. The approach presented here makes it possible to study the response of individual emitters to changes in excitation wavelength over a broad range. Hence, increased photoluminescence intermittency for certain excitation wavelengths will result in systematically reduced emission intensity for this wavelength in our study. We therefore calculated the sum of the photoluminescence excitation spectra from all single quantum dots analyzed in our study and compared it to the ensemble spectrum recorded with a calibrated ensemble spectrometer (Figure 3a). The summed photoluminescence excitation spectrum shows a number of interesting characteristics. Globally, blinking that was visible in the individual excitation spectra averages out, and the sum spectrum shows no explicit gaps where the intensity suddenly drops and then recurs. However, there are clear differences between the ensemble photoluminescence excitation spectrum and the summed excitation spectra from single quantum dots. On the short wavelength side, the sum spectrum declines much faster than the ensemble spectrum, while on the long wavelength side there is good agreement between the positions of the pronounced 1S(e)-2$S_{3/2}$(h) transition. This discrepancy on the short wavelength side of the sum spectrum is not apparent in the individual spectra and can be understood from the details of how each single emitter excitation spectrum was recorded, that is, by considering that the excitation wavelength was always scanned from short to long wavelength. As the transition to dark states is driven by the excitation light, the probability to find a single quantum dot in a non-emitting state is minimal at the start of the experiment. Over time, which translates to longer excitation wavelengths in our experiment, the probability to find a quantum dot in a long-lived dark state increases. In the extreme case, a transition to a dark state occurs and photoluminescence is not regained before the end of the experiment (Figure 3a, inset). Thus, shorter excitation wavelengths are overweighted in the sum spectrum in the excitation scheme used, which was dictated by the monochromator used for these experiments (see Supporting Information File 1 for details) that only allows for scanning of the excitation from low to high wavelengths. One promising way to overcome this limitation in future experiments is to use an acousto-optical tunable filter (AOTF) for fast wavelength selection and bidirectional wavelength scanning.

However, not all discrepancies between the sum spectrum and the ensemble spectrum can be explained by the details of the excitation scheme used. If the probability for a transition to a long-lived dark state is independent of the excitation wavelength, a steady decline of the summed single quantum dot excitation spectrum approaching the spectral shape of the ensemble spectrum is expected when both spectra are normalized to the long wavelength edges of the spectra. Indeed, we find good agreement between the sum and ensemble spectra for excitation wavelengths beyond ~580 nm, which suggests only a minor influence from transitions to dark states that do not recover during the entire data acquisition time in this wavelength range. On the other hand we find large deviations between the sum and ensemble spectra for excitation wavelengths below ~580 nm. This observation is consistent with reports that excitation in the band gap area results in little blinking compared to excitation above the band gap [32]. However, we do not see a smooth decline of the excitation sum spectrum, but observe what appear to be a number of steps (~530 nm, ~550 nm, 565 nm, and 595 nm (less prominent); Figure 3a). These drops in the sum spectrum indicate that at the associated excitation wavelengths an increased probability of an intensity drop, that is, of a transition to a dark state, exists. The drops at 530 nm, 550 nm and 570 nm appear to be weakly reflected in the bulk spectrum. Since transitions to dark states are not sampled in the bulk spectrum due to the comparatively low excitation powers used to record bulk spectra, these similarities might point towards the

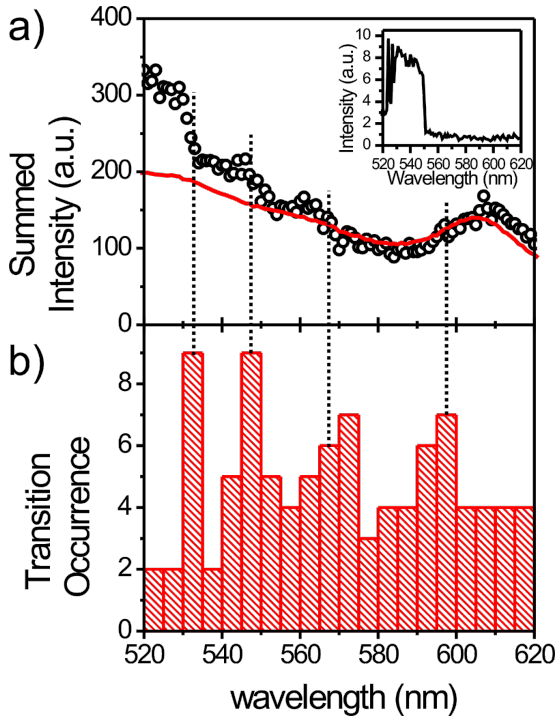

Figure 3: Single quantum dot excitation spectra reveal distinct excitation wavelengths with increased probability for a dark-state transition. a) sum spectrum of 48 excitation spectra of individual quantum dots (circles). Red: Ensemble excitation spectrum. Inset: Single quantum dot excitation spectra undergoing a transition to a dark state. b) Histogram of transitions to a long lived dark-state.

molecular mechanism underlying the increased probability for a transition to a dark state. To verify that the observed steps in the sum spectrum indeed result from an increased number of single quantum dots changing to a dark state, we created a histogram of the wavelengths for which a transition to a dark state could be observed (Figure 3b). To estimate the statistical significance of the distribution obtained we determined the p-value assuming equal probability of a dark state transition for all power normalized excitation wavelengths. We obtain a p-value of 0.06 indicating a statistically significant result since there is only a low probability of ~6% that the observed distribution originates from a random distribution of dark state transitions. The histogram shows significant peaks in the frequency of a dark state transition for the excitation wavelengths ~532 nm, ~548 nm, ~570 nm and ~595 nm. All four peaks are correlated to a signature in the sum spectrum.

The data suggest that there is not only a large difference in the probability of a transition to a dark state for excitation in the band gap compared to excitation above the band gap, but that there are additionally certain excitation wavelengths which preferentially induce transitions to dark states. We exclude the idea of increased blinking rates for lower wavelengths due to increased absorbance and thereby a higher probability of an Auger assisted ionization, since the excitation powers used were smaller at lower wavelengths than at higher wavelengths. Additionally such a mechanism cannot explain the increased probability of a dark state transition for certain wavelengths only. Our data indicates that the formation of dark states shows a complex dependence on the excitation wavelengths used, suggesting that dark states can be reached via different pathways that can be accessed preferentially by using certain excitation wavelengths. Besides details on the wavelength dependent blinking of single emitters, our data also give access to the individual spectral properties of the quantum dots. In Figure 2 we show some typical examples of single quantum dot excitation spectra. As a guide to the eye and for comparison, the reference ensemble excitation spectrum is plotted as a dashed red line in each panel of Figure 2.

Comparing the excitation spectra of different quantum dots we find both striking similarities and some clear differences between the spectra. The single quantum dot spectra are always enveloped by the ensemble spectrum below ~580 nm (Figure 2, Figure 1a). Besides dips and gaps due to the blinking behavior on different timescales, we see no significant differences between the single quantum dots or distinct individual features in this part of the spectrum.

In general, observed wavelength dependent changes in photoluminescence can result from changes in either the absorbance or the photoluminescence quantum yield. Although excitation wavelength dependent changes in photoluminescence quantum efficiency have been discussed [50,51], Tonti et al. were able to show that there is no intrinsic deviation between the excitation and absorbance spectra of quantum dots once all corrections and sample handling are properly performed [52]. This result implies that the photoluminescence quantum yield in CdSe quantum dot ensembles is independent of the excitation wavelength, and that analyzing the excitation spectra also allows one to draw conclusions about the absorbance spectra of single quantum dots. Following from this, the observed behavior directly results from the differences in the absorbance at different wavelengths of the quantum dots. The spectral region below 580 nm, where we find no clear signs of individual spectral behavior from individual quantum dots, is exactly that region where a quasicontinuum of optical transitions was observed at cryogenic temperatures, corresponding to low lying energy barriers between distinct states predicted by the theory. It is therefore not surprising that, except for blinking events, no individual characteristics of the observed quantum dots can be identified at room temperature in this wavelength region.

The picture changes significantly when looking at the pronounced transition at ~605 nm, closer to the band edge, where we find clear differences in the shape, height and spectral position of this peak in the individual excitation spectra. Variations in the spectral position of this peak from individual quantum dots are attributed to differences in the size of the individual quantum dots. As expected for a single molecule study, we also find that the width of the transition is generally smaller than the width of the ensemble transition. This broadening in the ensemble or summed single molecule spectra results from the superposition of a large number of excitation spectra of single quantum dots of varying peak wavelength. Interestingly, we find some excitation spectra that do not show narrowed spectral features, e.g., Figure 2b, pointing towards the existence of a phenomenon equivalent to spectral emission diffusion [53,54] in the excitation spectrum and, by inference, in the absorbance. Especially since we only find minor variations in the excitation spectra at the short wavelength side below 580 nm and do not observe individual fingerprints in this area, the observation of not only the spectral position but also the different relative height and shape for the $1S(e)$-$2S_{3/2}(h)$ transition reflects the individual characteristics of each single quantum dot. Moreover, our spectra strikingly show that the different heights and shapes of the transitions are not correlated with their spectral position and hence with the particle size, suggesting different molecular origins. The shape and height of the peak from the $1S(e)$-$2S_{3/2}(h)$ transition is determined by the coupling between these states. It has been shown that transitions close to the band edge show a fine structure splitting into

sublevels due to the quantum dot crystal field, shape anisotropy, and confinement enhanced electron-hole exchange interactions [55]. Although considerably broadened at room temperature and hence invisible in the ensemble, the variation of the height and shape of the peak around 605 nm, which we have observed for individual quantum dots, reflects details of these transitions. Since the differences in relative height of spectral features in the photoluminescence excitation spectrum represent the strength of the coupling between the ground and excited state of the individual quantum dots, it is likely that the observed differences in the individual excitation spectra reflect the differences in the photoluminescence quantum efficiency of individual quantum dots, as previously reported [56,57].

Conclusion

We have recorded for the first time single molecule excitation spectra at room temperature. The required spectrally narrow excitation over a wide spectral range of 100 nm was realized by using a monochromator to select the excitation wavelength from a supercontinuum white light source. The suitability of our approach and its potential were demonstrated by studying single quantum dots. The single emitter nature of our quantum dot samples was confirmed by photon antibunching experiments. Analysis of the single quantum dot excitation spectra gave access to hitherto unexplored details of this class of emitters. For the CdSe nanocrystals investigated, we found strong indications for an increased probability for a transition to long-lived dark states at specific excitation wavelengths, suggesting that these wavelengths are unsuitable for single photon applications. The excitation spectra showed no clear individual features for excitation wavelengths well above the band gap, but exhibited large differences for transitions close to the excitonic peak, representing the fine structure splitting into energetic sublevels of the individual quantum dots. Further, we found variations in the width and the spectral position of transitions for individual quantum dots.

On the basis of these investigations of quantum dots, we expect single molecule excitation spectroscopy to become a valuable addition to the established single molecule spectroscopy methods. The approach will not only aid in the analysis of isolated dyes or nanoparticles but also prove valuable in analyzing complex emitting systems such as Förster resonance energy transfer (FRET) pairs, fluorescent proteins and upconversion particles.

Experimental

We realized an instrument capable of single molecule excitation spectroscopy by combining a high power supercontinuum white light source (Fianium SC-400pp) with a grating spectrometer (Spectra Pro 300i, Acton Research) for excitation wavelength selection and a custom built confocal scanning stage single molecule detection microscope (for details see Supporting Information File 1). Experiments were carried out in two steps. First, the quantum dots immobilized in a thin polymer layer at low concentration ($c_{QD} = 5 \times 10^{-10}$ M) were visualized by creating a raster scanned emission intensity image of an 20×20 μm^2 area of the sample using a fixed excitation wavelength ($\lambda_{ex} = 600$ nm). After localization, the single quantum dots were positioned in the laser focus and the excitation wavelength was swept from 520 nm to 620 nm in increments of 1 nm. For each excitation wavelength the emitted fluorescence intensity was recorded for 400 ms, followed by an increment in the excitation wavelength during which data acquisition was disabled (~70 ms duration). In this way we obtained 400 ms fluorescence intensity trajectories depicting the evolution of the emission intensity for each excitation wavelength, interspersed with ~70 ms zero-intensity periods representing the excitation wavelength increment (Figure 1). To obtain the fluorescence excitation spectrum, the total emission intensity per excitation wavelength was integrated and calibrated using a reference spectrum recorded for a film of emitters (i.e., an ensemble of emitters) to compensate for wavelength dependent excitation power and detection efficiency (for details see Supporting Information File 1).

Supporting Information

Supporting Information features detailed description of instrumentation, and data acquisition and correction procedures.

Supporting Information File 1

Experimental details.
[http://www.beilstein-journals.org/bjnano/content/supplementary/2190-4286-2-56-S1.pdf]

Acknowledgements

This work was financed by a strategic research orientation grant from the MESA+ Institute for Nanotechnology to CB, MS, and VS and an MWK grant of the Land Baden-Württemberg to FS, SP, MS and AJM.

References

1. Moerner, W. *J. Phys. Chem. B* **2002,** *106,* 910–927. doi:10.1021/jp012992g
2. Schleifenbaum, F.; Blum, C.; Subramaniam, V.; Meixner, A. J. *Mol. Phys.* **2009,** *107,* 1923–1942. doi:10.1080/00268970802635004
3. Tinnefeld, P.; Sauer, M. *Angew. Chem., Int. Ed.* **2005,** *44,* 2642–2671. doi:10.1002/anie.200300647
4. Lupton, J. M. *Adv. Mater.* **2010,** *22,* 1689–1721. doi:10.1002/adma.200902306

5. Woell, D.; Uji-I, H.; Schnitzler, T.; Hotta, J. I.; Dedecker, P.; Herrmann, A.; De Schryver, F. C.; Muellen, K.; Hofkens, J. *Angew. Chem., Int. Ed.* **2008,** *47,* 783–787. doi:10.1002/anie.200704196
6. Roeffaers, M.; Sels, B.; Uji-i, H.; De Schryver, F.; Jacobs, P.; De Vos, D.; Hofkens, J. *Nature* **2006,** *439,* 572–575. doi:10.1038/nature04502
7. Schuler, B. *ChemPhysChem* **2005,** *6,* 1206–1220. doi:10.1002/cphc.200400609
8. Blum, C.; Subramaniam, V. *Anal. Bioanal. Chem.* **2009,** *393,* 527–541. doi:10.1007/s00216-008-2425-x
9. Dertinger, T.; Pacheco, V.; von der Hocht, I.; Hartmann, R.; Gregor, I.; Enderlein, J. *ChemPhysChem* **2007,** *8,* 433–443. doi:10.1002/cphc.200600638
10. Michalet, X.; Pinaud, F.; Bentolila, L.; Tsay, J.; Doose, S.; Li, J.; Sundaresan, G.; Wu, A.; Gambhir, S.; Weiss, S. *Science* **2005,** *307,* 538. doi:10.1126/science.1104274
11. Moerner, W. E. *Proc. Natl. Acad. Sci. U. S. A.* **2007,** *104,* 12596–12602. doi:10.1073/pnas.0610081104
12. Forkey, J. N.; Quinlan, M. E.; Goldman, Y. E. *Prog. Biophys. Mol. Biol.* **2000,** *74,* 1–35. doi:10.1016/S0079-6107(00)00015-8
13. Peterman, E.; Brasselet, S.; Moerner, W. *J. Phys. Chem. A* **1999,** *103,* 10553–10560. doi:10.1021/jp991968o
14. Schleifenbaum, F.; Blum, C.; Elgass, K.; Subramaniam, V.; Meixner, A. J. *J. Phys. Chem. B* **2008,** *112,* 7669–7674. doi:10.1021/jp7114753
15. Kapusta, P.; Wahl, M.; Benda, A.; Hof, M.; Enderlein, J. *J. Fluoresc.* **2007,** *17,* 43–48. doi:10.1007/s10895-006-0145-1
16. Tinnefeld, P.; Buschmann, V.; Herten, D.; Han, K.; Sauer, M. *Single Mol.* **2000,** *1,* 215–223. doi:10.1002/1438-5171(200009)1:3<215::AID-SIMO215>3.0.CO;2-S
17. Blum, C.; Meixner, A. J.; Subramaniam, V. *ChemPhysChem* **2008,** *9,* 310–315. doi:10.1002/cphc.200700784
18. Cotlet, M.; Hofkens, J.; Habuchi, S.; Dirix, G.; van Guyse, M.; Michiels, J.; Vanderleyden, J.; de Schryver, F. C. *Proc. Natl. Acad. Sci. U. S. A.* **2001,** *98,* 14398–14403. doi:10.1073/pnas.251532698
19. Lacoste, T. D.; Michalet, X.; Pinaud, F.; Chemla, D. S.; Alivisatos, A. P.; Weiss, S. *Proc. Natl. Acad. Sci. U. S. A.* **2000,** *97,* 9461–9466. doi:10.1073/pnas.170286097
20. Blum, C.; Meixner, A. J.; Subramaniam, V. *Biophys. J.* **2004,** *87,* 4172–4179. doi:10.1529/biophysj.104.049452
21. Widengren, J.; Kudryavtsev, V.; Antonik, M.; Berger, S.; Gerken, M.; Seidel, C. A. M. *Anal. Chem.* **2006,** *78,* 2039–2050. doi:10.1021/ac0522759
22. Eckel, R.; Walhorn, V.; Pelargus, C.; Martini, J.; Enderlein, J.; Nann, T.; Anselmetti, D.; Ros, R. *Small* **2007,** *3,* 44–49. doi:10.1002/smll.200600130
23. Taminiau, T.; Stefani, F.; Segerink, F.; Van Hulst, N. *Nat. Photonics* **2008,** *2,* 234–237. doi:10.1038/nphoton.2008.32
24. Chizhik, A.; Schleifenbaum, F.; Gutbrod, R.; Chizhik, A.; Khoptyar, D.; Meixner, A. J.; Enderlein, J. *Phys. Rev. Lett.* **2009,** *102,* 073002. doi:10.1103/PhysRevLett.102.073002
25. Gaiduk, A.; Yorulmaz, M.; Ruijgrok, P. V.; Orrit, M. *Science* **2010,** *330,* 353–356. doi:10.1126/science.1195475
26. Chong, S.; Min, W.; Xie, X. S. *J. Phys. Chem. Lett.* **2010,** *1,* 3316–3322. doi:10.1021/jz1014289
27. Kukura, P.; Celebrano, M.; Renn, A.; Sandoghdar, V. *J. Phys. Chem. Lett.* **2010,** *1,* 3323–3327. doi:10.1021/jz101426x
28. Orrit, M.; Bernard, J. *Phys. Rev. Lett.* **1990,** *65,* 2716–2719. doi:10.1103/PhysRevLett.65.2716
29. Ambrose, W.; Moerner, W. *Nature* **1991,** *349,* 225–227. doi:10.1038/349225a0
30. Kroutvar, M.; Ducommun, Y.; Heiss, D.; Bichler, M.; Schuh, D.; Abstreiter, G.; Finley, J. *Nature* **2004,** *432,* 81–84. doi:10.1038/nature03008
31. Neuhauser, R.; Shimizu, K.; Woo, W.; Empedocles, S.; Bawendi, M. *Phys. Rev. Lett.* **2000,** *85,* 3301–3304. doi:10.1103/PhysRevLett.85.3301
32. Knappenberger, K., Jr.; Wong, D.; Romanyuk, Y.; Leone, S. *Nano Lett.* **2007,** *7,* 3869–3874. doi:10.1021/nl0714740
33. Norris, D. J.; Bawendi, M. G. *Phys. Rev. B* **1996,** *53,* 16338–16346. doi:10.1103/PhysRevB.53.16338
34. Zwiller, V.; Blom, H.; Jonsson, P.; Panev, N.; Jeppesen, S.; Tsegaye, T.; Goobar, E.; Pistol, M.; Samuelson, L.; Björk, G. *Appl. Phys. Lett.* **2001,** *78,* 2476. doi:10.1063/1.1366367
35. Loss, D.; DiVincenzo, D. *Phys. Rev. A* **1998,** *57,* 120–126. doi:10.1103/PhysRevA.57.120
36. Medintz, I. L.; Uyeda, H. T.; Goldman, E. R.; Mattoussi, H. *Nat. Mater.* **2005,** *4,* 435–446. doi:10.1038/nmat1390
37. Alivisatos, A. P.; Gu, W. W.; Larabell, C. *Annu. Rev. Biomed. Eng.* **2005,** *7,* 55–76. doi:10.1146/annurev.bioeng.7.060804.100432
38. Ward, M.; Farrow, T.; See, P.; Yuan, Z.; Karimov, O.; Bennett, A.; Shields, A.; Atkinson, P.; Cooper, K.; Ritchie, D. *Appl. Phys. Lett.* **2007,** *90,* 063512. doi:10.1063/1.2472172
39. Klimov, V. I. *Annu. Rev. Phys. Chem.* **2007,** *58,* 635–673. doi:10.1146/annurev.physchem.58.032806.104537
40. Empedocles, S.; Norris, D.; Bawendi, M. *Phys. Rev. Lett.* **1996,** *77,* 3873–3876. doi:10.1103/PhysRevLett.77.3873
41. Htoon, H.; Cox, P. J.; Klimov, V. I. *Phys. Rev. Lett.* **2004,** *93,* 187402. doi:10.1103/PhysRevLett.93.187402
42. Wang, X.; Ren, X.; Kahen, K.; Hahn, M.; Rajeswaran, M.; Maccagnano-Zacher, S.; Silcox, J.; Cragg, G.; Efros, A.; Krauss, T. *Nature* **2009,** *459,* 686–689. doi:10.1038/nature08072
43. Efros, A. *Nat. Mater.* **2008,** *7,* 612–613. doi:10.1038/nmat2239
44. Hohng, S.; Ha, T. *J. Am. Chem. Soc.* **2004,** *126,* 1324–1325. doi:10.1021/ja039686w
45. Fisher, B. R.; Eisler, H.-J.; Stott, N. E.; Bawendi, M. G. *J. Phys. Chem. B* **2004,** *108,* 143–148. doi:10.1021/jp035756+
46. Basche, T.; Moerner, W. E.; Orrit, M.; Talon, H. *Phys. Rev. Lett.* **1992,** *69,* 1516–1519. doi:10.1103/PhysRevLett.69.1516
47. Lounis, B.; Bechtel, H.; Gerion, D.; Alivisatos, P.; Moerner, W. *Chem. Phys. Lett.* **2000,** *329,* 399–404. doi:10.1016/S0009-2614(00)01042-3
48. Lord, S. J.; Lee, H.-I. D.; Samuel, R.; Weber, R.; Liu, N.; Conley, N. R.; Thompson, M. A.; Twieg, R. J.; Moerner, W. E. *J. Phys. Chem. B* **2010,** *114,* 14157–14167. doi:10.1021/jp907080r
49. Deschenes, L. A.; Vanden Bout, D. A. *Chem. Phys. Lett.* **2002,** *365,* 387–395. doi:10.1016/S0009-2614(02)01490-2
50. Hoheisel, W. *J. Chem. Phys.* **1994,** *101,* 845.
51. Rumbles, G.; Selmarten, D.; Ellingson, R.; Blackburn, J.; Yu, P.; Smith, B.; Mićić, O.; Nozik, A. *J. Photochem. Photobiol., A* **2001,** *142,* 187–195. doi:10.1016/S1010-6030(01)00513-5
52. Tonti, D.; Van Mourik, F.; Chergui, M. *Nano Lett.* **2004,** *4,* 2483–2487. doi:10.1021/nl0486057
53. Stracke, F.; Blum, C.; Becker, S.; Müllen, K.; Meixner, A. J. *ChemPhysChem* **2005,** *6,* 1242–1246. doi:10.1002/cphc.200400436

54. Stracke, F.; Blum, C.; Becker, S.; Müllen, K.; Meixner, A. J. *Chem. Phys. Lett.* **2000,** *325,* 196–202. doi:10.1016/S0009-2614(00)00633-3
55. Htoon, H.; Takagahara, T.; Kulik, D.; Baklenov, O.; Holmes, A., Jr.; Shih, C. *Phys. Rev. Lett.* **2002,** *88,* 087401. doi:10.1103/PhysRevLett.88.087401
56. Biebricher, A.; Sauer, M.; Tinnefeld, P. *J. Phys. Chem. B* **2006,** *110,* 5174–5178. doi:10.1021/jp060660b
57. Brokmann, X.; Coolen, L.; Dahan, M.; Hermier, J. P. *Phys. Rev. Lett.* **2004,** *93,* 107403. doi:10.1103/PhysRevLett.93.107403

License and Terms

Beilstein Journal of Nanotechnology

Distinction of nucleobases – a tip-enhanced Raman approach

Regina Treffer[1], Xiumei Lin[1], Elena Bailo[2], Tanja Deckert-Gaudig[1] and Volker Deckert[*1,3]

Full Research Paper

Open Access

Address:
[1]IPHT – Institute for Photonic Technology, Albert-Einstein-Str. 9, D-07745 Jena, Germany, [2]WITec Wissenschaftliche Instrumente und Technologie GmbH, Lise-Meitner-Str. 6, D-89081 Ulm, Germany and [3]Institute of Physical Chemistry, Jena University, Helmholtzweg 4, D-07743 Jena, Germany

Email:
Volker Deckert[*] - volker.deckert@ipht-jena.de

* Corresponding author

Keywords:
DNA; nanoscale analysis; Raman; sequencing; TERS

Beilstein J. Nanotechnol. **2011,** *2,* 628–637.
doi:10.3762/bjnano.2.66

Received: 02 May 2011
Accepted: 18 August 2011
Published: 23 September 2011

This article is part of the Thematic Series "Nanophotonics, nano-optics and nanospectroscopy".

Guest Editor: A. J. Meixner

Abstract

The development of novel DNA sequencing methods is one of the ongoing challenges in various fields of research seeking to address the demand for sequence information. However, many of these techniques rely on some kind of labeling or amplification steps. Here we investigate the intrinsic properties of tip-enhanced Raman scattering (TERS) towards the development of a novel, label-free, direct sequencing method. It is known that TERS allows the acquisition of spectral information with high lateral resolution and single-molecule sensitivity. In the presented experiments, single stranded adenine and uracil homopolymers were immobilized on different kinds of substrates (mica and gold nanoplates) and TERS experiments were conducted, which demonstrated the reproducibility of the technique. To elucidate the signal contributions from the specific nucleobases, TERS spectra were collected on single stranded calf thymus DNA with arbitrary sequence. The results show that, while the Raman signals with respect to the four nucleobases differ remarkably, specific markers can be determined for each respective base. The combination of sensitivity and reproducibility shows that the crucial demands for a sequencing procedure are met.

Introduction

The determination of the exact nucleobase sequence of DNA is of great importance for research in the life sciences. The first sequencing methods were published in 1977 by Maxam and Gilbert [1], and Sanger et al. [2]. Since then the sequencing technology has been refined and automated, and current advances show a tendency towards single-molecule sequencing, which eventually results in the development of sequencing systems with reasonable costs and expenditure of time [3].

Tip-enhanced Raman scattering (TERS) is the combination of Raman spectroscopy with a scanning probe microscope, most often an atomic force microscope (AFM). A metal nanoparticle

at the apex of the AFM tip leads to a large enhancement of the electromagnetic field in the vicinity of the particle and consequently an increase of the Raman signal. Due to the size of the particle a lateral resolution of <20 nm can be reached [4-8]. The feasibility of TERS for biological samples has been exemplified by studies of specific molecules [9], single virus investigation [10] and studies of bacterial [11] and cellular systems [12,13], as well as of erythrocytes [14]. The first TERS experiments on DNA base nanocrystals [15-17] and a study of the hydrogen bonding between adenine and thymine on a gold substrate [18] showed that a distinction of the respective nucleobases is possible, and this eventually led to successful TERS measurements on a single RNA strand of a cytosine homopolymer [19].

The dependency of the electromagnetic field enhancement of TERS on the composition of the substrate, amongst other parameters, was shown in three-dimensional finite-difference time domain (3D-FDTD) simulations [20]. A metal substrate such as gold provides an additional field enhancement as it produces a large electromagnetic (EM) coupling with the tip, which is often called a "gap mode". In contrast, dielectric materials cannot couple as effectively, and hence in this case the effect relies on an isolated tip, resulting in a much smaller enhancement [20,21]. Prerequisites for a metal substrate suitable for TERS experiments on single stranded DNA or RNA are an almost atomic flatness of the surface and, as the used TERS setup is operated in back-reflection mode (i.e., through the substrate and back), transparency, i.e., the substrate has to be sufficiently thin. A suitable approach is the synthesis of triangular and hexagonal flat and transparent gold [22] or silver [23] nanoparticles that are large enough to avoid specific localized enhancement regions.

The experiments described here probed the factors affecting the TERS spectra collected on single stranded adenine and uracil homopolymers immobilized on a mica surface (adenine) and on a gold nanoplate (uracil), with respect to the intensity and reproducibility.

Another challenge with regards to a sequencing procedure with TERS is the fact that the four nucleobases reveal remarkably different Raman scattering cross sections. It was shown that in SERS experiments on an equimolar mixture of the bases, the intensities of the ring breathing modes of the distinct bases are as follows: Poly-adenine > poly-cytosine >> poly-guanine > poly-thymine [24]. Furthermore, in a comparison of the SERS spectra of two DNA molecules with different adenine contents (15.5% and 44.3%), the adenine signals dominated [25]. Hence it was predicted that signals from adenine only are likely to be detected when performing TERS experiments on native DNA [14]. In contrast, TERS measurements on calf thymus DNA presented here clearly show that specific contributions of all four nucleobases can be determined. Hence, with the chosen samples poly(A), poly(U) and calf thymus DNA typical molecules covering DNA, RNA and single stranded DNA molecules containing all four bases were addressed.

Results and Discussion

Figure 1a shows the AFM topography image of an adenine homopolymer on a mica substrate. As the height in the cross section is slightly higher than the height of a single DNA strand

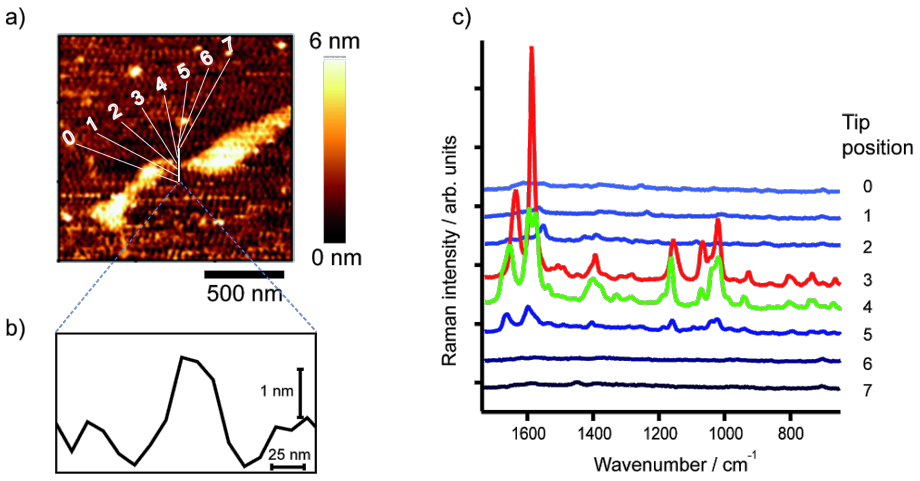

Figure 1: a) AFM topography image of adenine homopolymer, b) topography cross section of the raw data corresponding to the line indicated in a), and c) TERS spectra measured at the positions indicated in a). The AFM topography in a) was slightly smoothed (Gaussian) to enhance the contrast. The TERS experiment positions were selected using the topography as a template, but with a much smaller actual step size (10 nm) as it appears in the figure.

it is assumed that the sample is either coiled or that several strands are coagulated. TERS spectra were measured at eight different positions across the DNA each separated by a distance of 10 nm.

The measured positions are indicated in Figure 1a, and in Figure 1c the corresponding spectra are shown. Spectral features of poly(dA) can be seen at three positions, but only two exhibit a high enhancement, thus providing information on the enhancement area of the TERS tip. As the distance between two adjacent points is 10 nm, an enhancement region of <20 nm can be safely assumed. This value is a conservative estimation and in agreement with a tip diameter of approximately 20 nm, as we find typically from SEM pictures of similar probes [26].

Both spectra show bands that can be assigned to adenine and additional signals of the DNA backbone consisting of phosphate and ribose moieties. This would be not surprising in a normal Raman experiment, but in a TERS experiment the field decays rapidly with respect to the tip surface and these groups should only weakly contribute to the spectrum. Hence, the appearance of these signals could indicate that the DNA strands are not rigidly orientated on the mica substrate and, in addition to the previously mentioned topography arguments, support the assumption of a coiled or coagulated sample.

Simultaneously the instrumental reproducibility was evaluated by measuring TERS spectra twice at the same position. The respective spectra are shown in Figure 2 indicating that these spectra are nearly identical. This clearly indicates that the tip was positioned reliably at the selected positions and that sample drift was negligible during the measurement. The results also suggest that minute changes of the tip position can affect the spectral appearance as different parts of the molecule/strand experience a different enhancement when the tip is slightly changing its position. These changes, as can be seen in Figure 2, mainly manifest as changes in the intensity or peak ratios, nevertheless an assignment is still possible. The even smaller variations at the same tip position, e.g., the splitting of the band 1590 cm^{-1} (Figure 2, tip position 4a and 4b), must then be attributed either to a drift of the instrument in the subnanometre range or to molecular orientation changes, e.g., rotation.

An assignment for the TERS spectra measured at positions 3 and 4 is given in Table 1. For the band assignment the spectral features were compared with those of SERS and Raman spectra

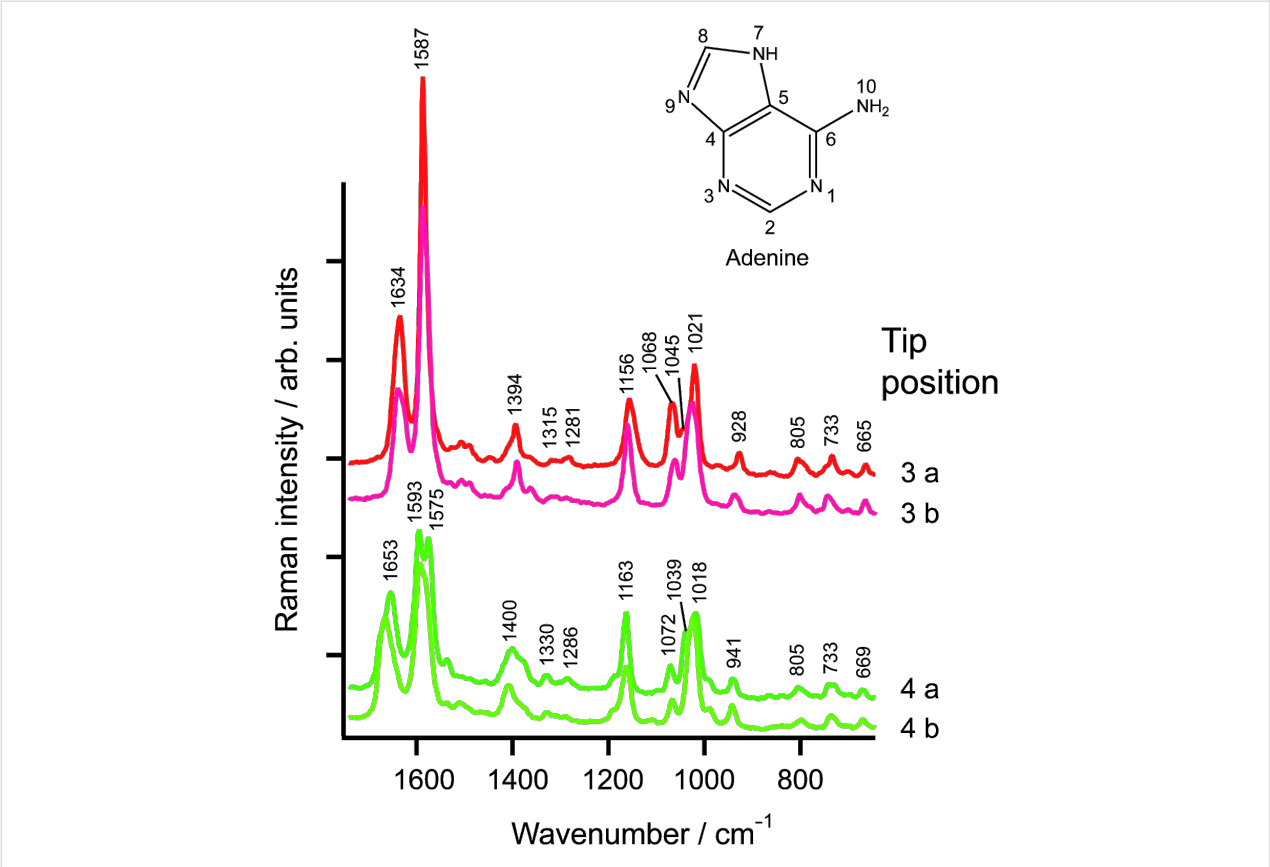

Figure 2: TERS spectra of the adenine homopolymer at positions 3 and 4 as indicated in Figure 1a. Both positions were measured twice (a, b).

of adenine derivates (deoxyadenosine (dA) [27], deoxyadenosine monophosphate (AMP) [28] and single stranded adenine homopolymer (poly(dA)) [29]).

A comparison of TERS and SERS spectra of adenine (or any other molecule) must take into account that a SERS experiment is either done in a colloidal solution or the dissolved sample is brought into contact with a solid SERS substrate. In both cases the molecules can select favoured binding sites to adsorb to the metal particles. In case of adenine these are the four nitrogen atoms: The pyrimidine N_1 and N_3, the imidazole N_7 and the N_{10} of the exocyclic NH_2 group. N_9 is the binding site to the ribose and therefore cannot bind to the metal nanoparticle. Density functional theory (DFT) calculations show changes in Raman band intensities and positions for the four respective complexes of adenine and a silver atom. These variations are attributed to a deformation of the adenine molecules to an energetically optimized conformation [16]. For the TERS experiments the adenine homopolymer was immobilized on a mica substrate and could not move freely. Consequently the TERS tip can be positioned at thermodynamically "unfavoured" sites, giving rise to a slightly different appearance of the spectra, in particular when chemical interactions between the tip and the SERS/TERS probe take place. Assuming an optimal immobilization, the phosphate backbone is fixed to the substrate and the bases should face upward. As single stranded DNA is a very flexible molecule it tends to form loops or twists along the strand, or even secondary helix structures. In this case the backbone becomes accessible and spectral contributions of the phosphate and sugar moieties can disguise the adenine signals at such positions. The bands at 1045 cm^{-1} at point 3 and 1039 cm^{-1} at position 4 are assigned to the N–sugar stretching and C–O sugar stretching vibrations and the bands at 1068 cm^{-1} at position 3 and 1072 cm^{-1} at position 4 are assigned to the N–sugar stretching and PO_2^- stretching vibrations. This strongly indicates an interaction of the backbone of the DNA strands with the silver tip and agrees well with the previously mentioned formation of loops along the strand.

Table 1: Band assignment of the TERS spectra of the adenine homopolymer (in cm^{-1}).[a]

Mode	3	4	SERS [27]	NRS [27]	SERS [28]	NRS [29]	Assignment
1	665	669				663	ring def [29]
2	733	733	728	734	732	727	ring breathing (Py) [27,29]
3	805	805				790/819	bk (OPO str), ring [29]
4						842	bk (OPO str) [29]
5	928	941	919	908	(960)	917	NH_2 rk [27], sugar [29]
6	1021	1018				1007	NH_2 def
7	1045	1039	1035			1052	N–sugar str [27], sugar (CO str) [29]
8	1068	1072		1066		1092	N–sugar str [27], bk (PO_2^- str) [29]
9	1156	1163	1171	1174		1163	(C_5–C_6) str [27]
10						1204	ring [29]
11						1221	ring [29]
12	1281	1286			1264	1251	ring [29]
13	1315	1330	1320	1348	1334	1306	C–N str [27], ring [29]
14						1336	ring [29]
15						1345	ring [29]
16	1394	1400	1389	1380	1370 1390	1378	(C_6–N_1) str (Py) [27], ring [29]
17						1423	ring [29]
18						1444	CH_2 def [29]
19			1472	1478	1460	1462	C=N str (Py) [27], C_2H_2 def [29]
20						1485	ring [29]
21						1509	ring [29]
22	1587	1575	1551	1572		1581	ring str [27,29], NH_2 def [29]
23		1593	1594				NH_2 def [27]
24	1634	1653	1657				NH_2 sci [27]

[a]Abbreviations: NRS, normal Raman scattering; SERS, surface-enhanced Raman scattering; Py, pyrimidine; bk, backbone; str, stretching; def, deformation; rk, rocking; sci, scissoring.

A Raman band around 725 cm^{-1} is usually present in spectra of purine derivates (except guanine), and this is attributed to the pyrimidine ring breathing mode. Pure adenine shows this band at 723 cm^{-1} and poly(dA) at 727 cm^{-1}. In the TERS spectra the previously mentioned binding of one or more nitrogen atoms to silver atoms of the tip, and/or conformational changes, cause a shift to 733 cm^{-1}.

In order to test the feasibility of different sample supports and to further check the reproducibility of the setup, TERS experiments on uracil homopolymer strands on transparent ultraflat gold substrates were performed. Figure 3 shows the AFM topography of a uracil strand immobilized on a typical gold nanoplate substrate. The magnification of the indicated area, in particular the height profile, indicates a single strand of polyuracil.

TERS spectra were obtained on five different positions on the strand and are shown in Figure 4. In addition a reference spectrum was recorded on pure gold to exclude spurious results due to tip contamination.

The spectra look remarkably similar and the main spectral features of uracil can be assigned. Minor variations in band

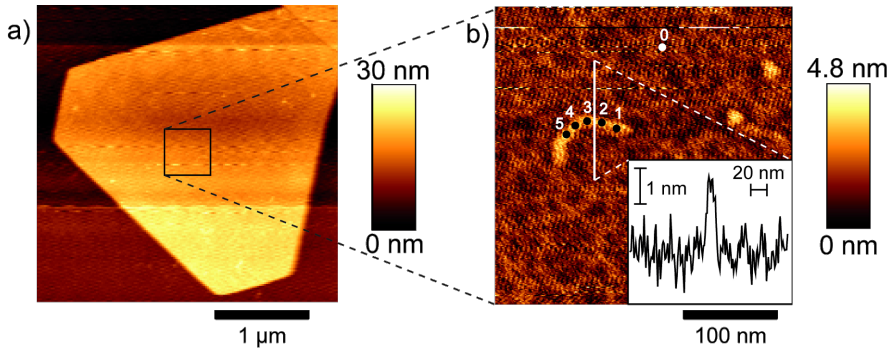

Figure 3: a) AFM topography image of a gold nanoplate with immobilized polyuracil strands, b) single strand of uracil homopolymer in the magnified area indicated in a). Inset in b) is the cross section corresponding to the line indicated in b).

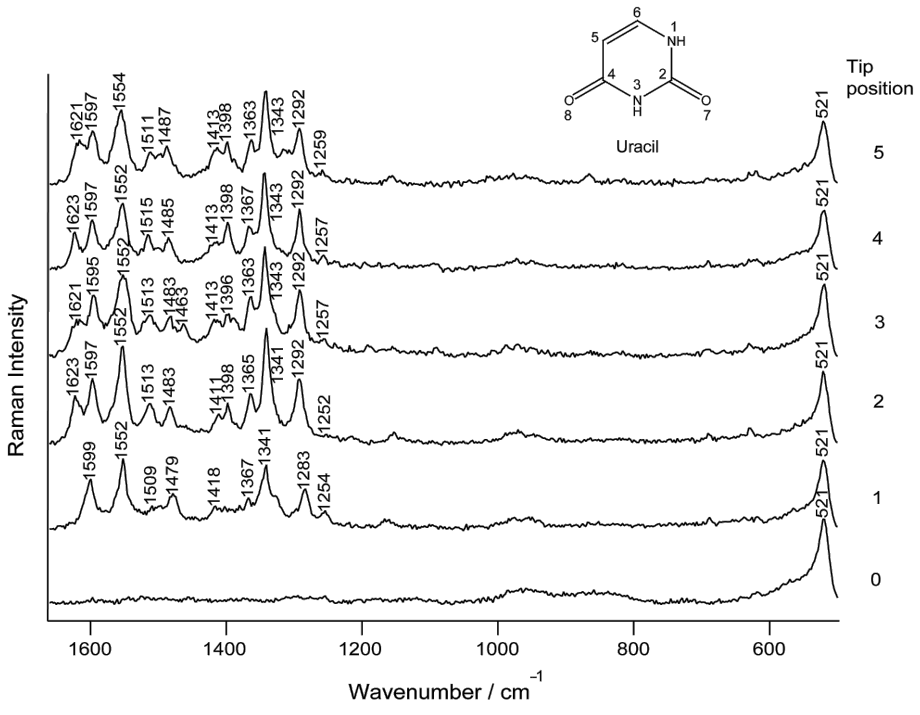

Figure 4: TERS spectra of the uracil homopolymer, measured at the positions indicated in Figure 3b.

intensity ratios and positions can be attributed to the previously discussed effects that appear when measuring with such a high lateral resolution [30]. Surprisingly, the usually intense ring breathing mode of uracil at 800 cm^{-1} is not visible in the spectra. As those vibrations that involve polarizability changes parallel to the TERS tip axis are expected to be more enhanced than perpendicular vibrations, the lack of the ring breathing mode may be due to a flat orientation of the ring on the gold surface. Similar effects were found to influence the ring breathing mode of aromatic amino acids [31]. Apart from this difference the spectral features can be attributed solely to uracil and no signals of the sugar and phosphate backbone were found. This suggests a strong immobilization of the homopolymer on the gold surface through the phosphate backbone. This finding, however, somewhat contradicts the idea of a flat orientation of the ring with respect to the gold substrate, and no explanation can be given at the moment.

An assignment of the measured spectra is provided in Table 2.

In a further step we address the issue of the different Raman cross sections of the distinct bases. Figure 5 shows four representative TERS spectra, out of a series of 26, that were measured on single stranded calf thymus DNA immobilized nonspecifically on a mica substrate. Spectral features of adenine, cytosine, guanine and thymine can be seen in the spectra. A tentative assignment of these four data sets is given in Table 3. As expected, when compared to the previously shown data on homogeneous strands, the spectra show a striking difference when measured at distinct tip positions, a fact that can be related to specific nucleobase patterns underneath the tip.

Among the 26 collected spectra, five show nucleobase ring breathing modes and no contributions from phosphate or ribose, indicating an immobilization of the DNA strand on the mica substrate through the phosphate backbone. The adenine ring breathing mode is shifted to lower wavenumbers due to the deformation of the molecule by the silver tip, supposedly because the silver atoms pushed against the N_3 nitrogen during the measurement [16]. The guanine ring breathing mode is down shifted as well, and thus it is likely that the same effects are responsible for this observation. Seven spectra showed spectral contributions from the phosphate and sugar, and no ring breathing modes were detected. Consequently in these cases the nucleobases are preferentially orientated perpendicular to the TERS tip axis, i.e., flat on the substrate surface, and only the DNA backbone interacts with the silver tip. Finally some TERS spectra show bands that can be attributed to ring breathing modes, to the ribose or to the phosphate backbone, as for example spectrum 3, either pointing towards a nonspecific binding of the DNA strands or to a coiled structure.

Assigning the bands of the TERS spectra is challenging regarding the different proposed band assignments found in the literature. An example is the band at 1251 cm^{-1} in spectrum 3. It can be attributed to the (C_8–H, N_9–H) deformation, the (N_7–C_8) stretching of adenine [35], a ring mode of adenine or cytosine [37], the (C_8–N_9) stretching of guanine [27] or the in-plane ring stretching of thymine [35].

Nevertheless, despite these difficulties and the previously mentioned intrinsic properties of the TERS setup, most bands can be unambiguously assigned to a specific base and thus can serve as marker bands. Others, such as the band at around

Table 2: Band assignment of the TERS spectra of the uracil homopolymer (cm^{-1}).[a]

1	2	3	4	5	Assignment
521	521	521	521	521	silicon (AFM tip)
1254	1252	1257	1257	1259	str N_3C_4, bend N_1H, C_5H, C_6H [32]
1283	1292	1292	1292	1292	str N_3C_4 (–C_4C_5–C_6N_1), bend N_1H, C_5H, C_6H [33]
1341	1341	1343	1343	1343	bend N_3H, C_5H, C_6H, str C_2N_3 [33,34]
1367	1365	1363	1367	1363	str N_1C_2–C_2N_3 + C_4C_5 (–C_2O_7), bend C_5H [32]
	1398	1396	1398	1398	bend N_1H, C_5H, C_6H [32]/str (NC–CN + CC–CN) [35]
1418	1411	1413	1413	1413	bend N_3H, N_1H, str N_1C_2, N_3C_4 [34]
		1463			bend C_6H, N_1H, N_2H, C_5H, str C_4C_5 [34]
1479	1483	1483	1485	1487	str C_6N_1–C_4C_5–C_2O_7, bend N_1H, C_5H, C_6H [32]
1509	1513	1513	1515	1511	bend N_1H, str C_6N_1 [34]/def (NH) + in-plane ring str [35]
1552	1552	1552	1552	1554	str C_4O–C_5C_6–C_2O, bend N_1H, C_6H [33]
1599	1597	1595	1597	1597	str C_4O_8, bend N_1H, C_6H [32]
	1623	1621	1623	1621	str C_2O_7 + C_5C_6, bend N_1H [32]

[a]Abbreviations: str, stretching; bend, bending; def, deformation.

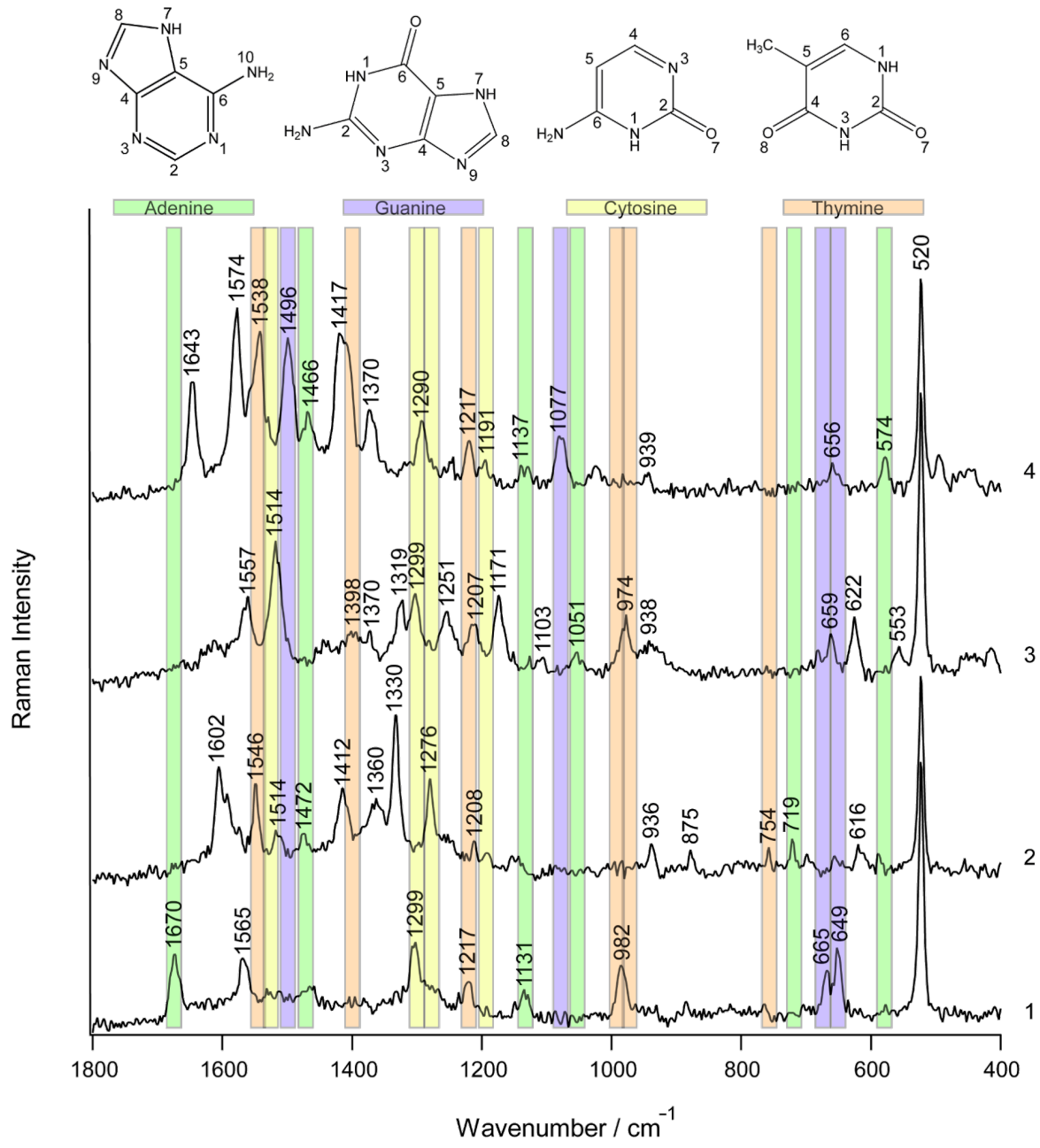

Figure 5: TERS spectra measured at four positions on single stranded calf thymus DNA. Unambiguously assignable bands are highlighted.

938 cm^{-1} in spectra 2, 3 and 4, cannot be related to a distinct base, but instead can be assigned to the NH_2 rocking mode of adenine, cytosine and guanine and, hence, exclude thymine. The band at around 650 cm^{-1} can be assigned to the guanine ring breathing mode. It usually is more intense, but it is also polarization and orientation dependent. Green et al. reported the detection of two Raman bands at 650 cm^{-1} and 688 cm^{-1}, both associated with the guanine ring breathing mode [24]. As the normal Raman band of free guanine is found at 680 cm^{-1} and the SERS band at 650 cm^{-1}, different adsorption configurations can be assumed, while the appearance of both bands in one spectrum of DNA can be explained by a steric influence of the backbone on the adsorption behavior of the strands. In our case the two bands never appeared in one spectrum and only once was the guanine band at 686 cm^{-1} detected.

Adenine exhibits a higher Raman scattering cross section than guanine. The band at 1319 cm^{-1} in spectrum 3 and the band at

Table 3: Band assignment of the TERS spectra of the calf thymus DNA (cm^{-1}).[a]

1	2	3	4	Assignment
520	520	520	520	silicon (AFM tip)
		553		C/T (ring def) [35]
			574	A (C_2–H, N_9–H wag) [35]
	616	622		A/T (ring def) [35]
649		659	656	G (ring breathing) [15,24]
665				G (ring breathing (Im)) [27]
	719			A (ring breathing) [15,35,36]
	754			T (ring breathing) [35,37]
	875			deoxyribose ring [38]
	936	938	939	A/C/G (NH_2 rk) [27,35]/deoxyribose [39]
		974		T (CC str, CO str, ribose) [40]
982				T (out-of-plane NH_2 wagging) [35]
		1051		A (N–sugar str) [27]
			1077	G [27]
		1103		PO_2 sym str
1131			1137	A (C_8–N_9 str, N_9–H, C_8–H def) [35]
		1171		A/G (C_5–C_6 str) [27]
			1191	C [15]
	1208	1207		T (ring str) [15,27,40]
1217			1217	T (in-plane ring-CH_3 str) [35]
		1251		A [35,37]/C [37]/G (C_8–N_9 str) [27]/T (ring str) [35]
	1276			C (C–NH_2 str + ring str) [35,39]
1299		1299	1290	C (C_2–N_3 str) [24,27]
		1319		A/G (C–N str (Im)) [27]
	1330			A/G (ring mode) [38]
	1360	1370	1370	A/C/G/T (C–N str (Py)) [27]
		1398		T (NH def/CH_3 def) [27,35]
	1412		1417	C (C_4–C_5 str) [27]/A [35]/T [35]
	1472		1466	A (C=N str (Py)) [27]
			1496	G (C=N str (Im)) [27]
	1514	1514		C (NH_2 def) [27]
	1546		1538	T (in-plane ring str) [35]
1565		1557	1574	A/C/G/T (ring str (Py)) [27]
	1602			A/C/G (NH_2 def) [27,37]
			1643	C/G/T (C=O str, C=C str) [27,40]
1670				A (NH_2 sci) [27]

[a]Abbreviations: Py, pyrimidine; Im, imidazole; str, stretching; def, deformation; rk, rocking; sci, scissoring.

1330 cm^{-1} in spectrum 2 can be attributed to adenine and guanine, respectively. To support this assignment further information from the other spectra must also be considered. Spectrum 3 shows the guanine ring breathing mode; consequently the band at 1319 cm^{-1} can be assigned to guanine. In spectrum 2 the adenine ring breathing mode appears (719 cm^{-1}), supporting the assignment of the band at 1330 cm^{-1} to adenine.

The band at 754 cm^{-1} in spectrum 2 refers to the ring breathing mode of thymine [35,37], but this mode also exhibits a band at around 800 cm^{-1} [15,18,35]. In our case only one of these bands was detected in the respective TERS spectra. This can probably be explained by orientational effects, similarly to the case of adenine.

The previously mentioned different Raman scattering cross sections of the nucleobases are reflected in the TERS spectra to a certain extent, as there are more spectral contributions from adenine, guanine and cytosine and relatively little from thymine. However, evidence for all four nucleobases was

found, and consequently a sequence-specific detection is only restricted by the lateral resolution and ultimately by the signal-to-noise ratio of the spectra recorded at subsequent positions.

Conclusion

Our results present several important steps towards a direct and label-free sequencing of RNA/DNA strands. First of all a reproducible immobilization of DNA and RNA strands on different substrates could be achieved. The successful TERS measurement on a uracil homopolymer immobilized on a gold nanoplate substrate is of particular interest regarding the additional field enhancement and field confinement attributed to a metal substrate. The TERS spectra collected on the DNA and RNA homopolymers show a high reproducibility of the spectral features of the respective base and clearly demonstrate the effects related to the tip location. A very important finding was that spectral contributions from all four nucleobases can be detected and distinguished on a genuine strand. In previous experiments it was shown that the limits of detection of TERS already reach single base sensitivity [19]. In combination with the results presented here, this means that when the TERS probe is laterally shifted over the DNA strand in intervals of less than one base-to-base distance the subsequent spectra provide the sequence information.

Experimental

Sample preparation

A single stranded DNA homopolymer of adenine (Sigma-Aldrich Chemie GmbH, Germany), a single stranded RNA homopolymer of uracil (Sigma-Aldrich) and single stranded calf thymus DNA (Sigma-Aldrich) were used in these experiments without further purification. Any further chemicals used for buffer solutions and colloid synthesis were purchased either at Sigma-Aldrich or VWR international. The adenine homopolymer and the calf thymus DNA were dissolved in a buffer solution consisting of HEPES (20 mM, 4-(2-hydroxyethyl)-1-piperazineethanesulfonic acid) and magnesium chloride (20 mM, $MgCl_2$) to immobilize the strands through the negatively charged phosphate backbone by means of divalent cations (Mg^{2+}) on mica (BAL-TEC) [19]. The concentration was 10–100 ng/μL. 1 μL of the respective solution was dropped on a freshly cleaved mica sheet and incubated under an argon atmosphere. Residues from the buffer were removed prior to the TERS measurements by rinsing with double distilled water and subsequent drying under argon [41].

The uracil homopolymer was dissolved in water and immobilized through nonspecific adsorption through the pyrimidine ring on gold nanoplates. The synthesis is described in detail in [22]. For the immobilization procedure the gold nanoplates were centrifuged onto a clean cover slide. 1 μL of the polyuracil solution was dropped on this substrate and incubated under an argon atmosphere. Excess RNA strands were removed with double distilled water and subsequent drying under argon.

Instrumentation

The TERS setup used for the experiments on the adenine homopolymer and the calf thymus DNA has been described in detail elsewhere [15,26,42]. For all TERS spectra of the adenine homopolymer the laser intensity on the sample was set to 500 μW at 530.9 nm and the acquisition time was 5 s. For all TERS measurements on the calf thymus DNA the laser intensity at the sample was set to 1 mW at 568.2 nm and the acquisition time was 10 s.

The TERS setup employed for the measurement on the uracil homopolymer consists of an adapted Raman spectrometer (Acton Advanced SP2750 A, S&I GmbH, Germany) in combination with an AFM (NanoWizard II, JPK Instruments AG, Germany). The laser intensity on the sample was set to 860 μW at 532 nm and the acquisition time was 5 s.

Regarding both instruments, the time lag between two spectra is <1 second, which corresponds to the tip moving to the next position and the storage of the acquired data.

Acknowledgements

We thank the Federal Ministry of Education and Research (BMBF) project No. 0312032B for financial support.

References

1. Maxam, A. M.; Gilbert, W. *Proc. Natl. Acad. Sci. U. S. A.* **1977,** *74,* 560–564. doi:10.1073/pnas.74.2.560
2. Sanger, F.; Nicklen, S.; Coulson, A. R. *Proc. Natl. Acad. Sci. U. S. A.* **1977,** *74,* 5463–5467. doi:10.1073/pnas.74.12.5463
3. Treffer, R.; Deckert, V. *Curr. Opin. Biotechnol.* **2010,** *21,* 4–11. doi:10.1016/j.copbio.2010.02.009
4. Stöckle, R. M.; Suh, Y. D.; Deckert, V.; Zenobi, R. *Chem. Phys. Lett.* **2000,** *318,* 131–136. doi:10.1016/S0009-2614(99)01451-7
5. Hayazawa, N.; Inouye, Y.; Sekkat, Z.; Kawata, S. *Opt. Commun.* **2000,** *183,* 333–336. doi:10.1016/S0030-4018(00)00894-4
6. Anderson, M. S. *Appl. Phys. Lett.* **2000,** *76,* 3130–3132. doi:10.1063/1.126546
7. Hartschuh, A.; Sánchez, E. J.; Xie, X. S.; Novotny, L. *Phys. Rev. Lett.* **2003,** *90,* 095503. doi:10.1103/PhysRevLett.90.095503
8. Pettinger, B.; Picardi, G.; Schuster, R.; Ertl, G. *Single Molecules* **2002,** *3,* 285–294. doi:10.1002/1438-5171(200211)3:5/6<285::AID-SIMO285>3.0.CO;2-X
9. Schmid, T.; Messmer, A.; Yeo, B.-S.; Zhang, W.; Zenobi, R. *Anal. Bioanal. Chem.* **2008,** *391,* 1907–1916. doi:10.1007/s00216-008-2101-1
10. Cialla, D.; Deckert-Gaudig, T.; Budich, C.; Laue, M.; Möller, R.; Naumann, D.; Deckert, V.; Popp, J. *J. Raman Spectrosc.* **2009,** *40,* 240–243. doi:10.1002/jrs.2123

11. Neugebauer, U.; Rösch, P.; Schmitt, M.; Popp, J.; Julien, C.; Rasmussen, A.; Budich, C.; Deckert, V. *ChemPhysChem* **2006,** *7,* 1428–1430. doi:10.1002/cphc.200600173
12. Böhme, R.; Richter, M.; Cialla, D.; Rösch, P.; Deckert, V.; Popp, J. *J. Raman Spectrosc.* **2009,** *40,* 1452–1457. doi:10.1002/jrs.2433
13. Böhme, R.; Cialla, D.; Richter, M.; Rösch, P.; Popp, J.; Deckert, V. *J. Biophotonics* **2010,** *3,* 455–461. doi:10.1002/jbio.201000030
14. Yeo, B.-S.; Stadler, J.; Schmid, T.; Zenobi, R.; Zhang, W. *Chem. Phys. Lett.* **2009,** *472,* 1–13. doi:10.1016/j.cplett.2009.02.023
15. Rasmussen, A.; Deckert, V. *J. Raman Spectrosc.* **2006,** *37,* 311–317. doi:10.1002/jrs.1480
16. Watanabe, H.; Ishida, Y.; Hayazawa, N.; Inouye, Y.; Kawata, S. *Phys. Rev. B* **2004,** *69,* 155418. doi:10.1103/PhysRevB.69.155418
17. Domke, K. F.; Zhang, D.; Pettinger, B. *J. Am. Chem. Soc.* **2007,** *129,* 6708–6709. doi:10.1021/ja071107q
18. Zhang, D.; Domke, K. F.; Pettinger, B. *ChemPhysChem* **2010,** *11,* 1662–1665. doi:10.1002/cphc.200900883
19. Bailo, E.; Deckert, V. *Angew. Chem., Int. Ed.* **2008,** *47,* 1658–1661. doi:10.1002/anie.200704054
20. Yang, Z.; Aizpurua, J.; Xu, H. *J. Raman Spectrosc.* **2009,** *40,* 1343–1348. doi:10.1002/jrs.2429
21. Futamata, M.; Maruyama, Y.; Ishikawa, M. *J. Phys. Chem. B* **2003,** *107,* 7607–7617. doi:10.1021/jp022399e
22. Deckert-Gaudig, T.; Deckert, V. *Small* **2009,** *5,* 432–436. doi:10.1002/smll.200801237
23. Deckert-Gaudig, T.; Erver, F.; Deckert, V. *Langmuir* **2009,** *25,* 6032–6034. doi:10.1021/la901001n
24. Green, M.; Liu, F.-M.; Cohen, L.; Köllensperger, P.; Cass, T. *Faraday Discuss.* **2006,** *132,* 269–280. doi:10.1039/b506636k
25. Barhoumi, A.; Zhang, D.; Tam, F.; Halas, N. J. *J. Am. Chem. Soc.* **2008,** *130,* 5523–5529. doi:10.1021/ja800023j
26. Budich, C.; Neugebauer, U.; Popp, J.; Deckert, V. J. *Microsc.* **2008,** *229,* 533–539. doi:10.1111/j.1365-2818.2008.01939.x
27. Jang, N.-H. *Bull. Korean Chem. Soc.* **2002,** *23,* 1790–1800. doi:10.5012/bkcs.2002.23.12.1790
28. Otto, C.; De Mul, F. F. M.; Huizinga, A.; Greve, J. *J. Phys. Chem.* **1988,** *92,* 1239–1244. doi:10.1021/j100316a046
29. Movileanu, L.; Benevides, J. M.; Thomas, G. J., Jr. *J. Raman Spectrosc.* **1999,** *30,* 637–649. doi:10.1002/(SICI)1097-4555(199908)30:8<637::AID-JRS431>3.0.CO;2-B
30. Deckert-Gaudig, T.; Bailo, E.; Deckert, V. *J. Biophotonics* **2008,** *1,* 377–389. doi:10.1002/jbio.200810019
31. Deckert-Gaudig, T.; Rauls, E.; Deckert, V. *J. Phys. Chem. C* **2010,** *114,* 7412–7420. doi:10.1021/jp9098045
32. Cho, K.-H.; Choo, J.; Joo, S.-W. *Spectrochim. Acta, Part A: Mol. Biomol. Spectrosc.* **2005,** *61,* 1141–1145. doi:10.1016/j.saa.2004.06.032
33. Lin, Z.-B.; Xie, B.-G.; Tian, J.-H.; Tang, Y.-A.; Sun, J.-J.; Chen, G.-N.; Ren, B.; Mao, B.-W.; Tian, Z.-Q. *J. Electroanal. Chem.* **2009,** *636,* 74–79. doi:10.1016/j.jelechem.2009.09.014
34. Giese, B.; McNaughton, D. *J. Phys. Chem. B* **2002,** *106,* 1461–1470. doi:10.1021/jp011986h
35. Badr, Y.; Mahmoud, M. A. *Spectrochim. Acta, Part A: Mol. Biomol. Spectrosc.* **2006,** *63,* 639–645. doi:10.1016/j.saa.2005.06.013
36. Giese, B.; McNaughton, D. *J. Phys. Chem. B* **2002,** *106,* 101–112. doi:10.1021/jp010789f
37. Ke, W.; Zhou, D.; Wu, J.; Ji, K. *Appl. Spectrosc.* **2005,** *59,* 418–423. doi:10.1366/0003702053641487
38. Thomas, G. J., Jr.; Benevides, J. M.; Overman, S. A.; Ueda, T.; Ushizawa, K.; Saitoh, M.; Tsuboi, M. *Biophys. J.* **1995,** *68,* 1073–1088. doi:10.1016/S0006-3495(95)80282-1
39. Hennemann, L. E.; Meixner, A. J.; Zhang, D. *Spectroscopy* **2010,** *24,* 119–124. doi:10.3233/SPE-2010-0416
40. Escobar, R.; Carmona, P.; Molina, M. *Analyst* **1996,** *121,* 105–109. doi:10.1039/an9962100105
41. Hansma, H. G.; Revenko, I.; Kim, K.; Laney, D. E. *Nucleic Acids Res.* **1996,** *24,* 713–720. doi:10.1093/nar/24.4.713
42. Bailo, E.; Deckert, V. *Chem. Soc. Rev.* **2008,** *37,* 921–930. doi:10.1039/b705967c

License and Terms

Beilstein Journal of Nanotechnology

Distance dependence of near-field fluorescence enhancement and quenching of single quantum dots

Volker Walhorn*§, Jan Paskarbeit, Heinrich Gotthard Frey, Alexander Harder and Dario Anselmetti

Full Research Paper

Open Access

Address:
Experimental Biophysics and Applied Nanosciences, Bielefeld University, Department of Physics, Universitätsstr. 25, 33615 Bielefeld, Germany

Email:
Volker Walhorn* - volker.walhorn@physik.uni-bielefeld.de

* Corresponding author
§ Fax: +49 (0)521 106 2959

Keywords:
AFM; fluorescence energy transfer; multiple multipole simulation; quantum dots

Beilstein J. Nanotechnol. **2011,** *2,* 645–652.
doi:10.3762/bjnano.2.68

Received: 29 April 2011
Accepted: 24 August 2011
Published: 29 September 2011

This article is part of the Thematic Series "Nanophotonics, nano-optics and nanospectroscopy".

Guest Editor: A. J. Meixner

Abstract

In fluorescence microscopy and spectroscopy, energy transfer processes between single fluorophores and fluorophore quencher pairs play an important role in the investigation of molecular distances or orientations. At distances larger than about 3 nm these effects originate predominantly from dipolar coupling. As these experiments are commonly performed in homogenous media, effects at the interface boundaries can be neglected. Nevertheless, the combination of such assays with single-molecule manipulation techniques such as atomic force microscopy (AFM) requires a detailed understanding of the influence of interfaces on dipolar coupling effects. In the presented work we used a combined total internal reflection fluorescence microscopy (TIRFM)–AFM setup to elucidate this issue. We measured the fluorescence emission emanating from single quantum dots as a function of distance from the apex of a gold-coated cantilever tip. As well as fluorescence quenching at close proximity to the tip, we found a nonlinear and nonmonotonic distance dependence of the fluorescence emission. To confirm and interpret our findings we performed calculations on the basis of a simplified multiple multipole (MMP) approach, which successfully supports our experimental data. Moreover, we revealed and quantified the influence of interfering processes such as field enhancement confined at interface boundaries, mirror dipoles and (resonant) dipolar coupling.

Introduction

Fluorescence microscopy and spectroscopy are important and versatile tools in life sciences. Fluorophores are not merely position markers, but can be regarded as active transducers that interact with species in their local vicinity and provide information about their micro-environment. The spectroscopic properties of semiconductor nanocrystals (quantum dots) can be easily tuned and they exhibit excellent resistance against photobleaching. Moreover, quantum dots that are functionalized for

biological applications are readily available. Locally confined dipole–dipole couplings, such as quenching and fluorescence resonance energy transfer (FRET) [1] between individual molecules, open up fascinating means to explore inter- or intramolecular distances [2], orientation [3], affinity and binding dynamics at the single-molecule level [4]. The combination of fluorescence with single-molecule manipulation techniques, e.g., AFM [5] or optical tweezers [6], opens up novel means of manipulating and controlling matter at the nanometer scale, and also applications such as optomechanics [7] and externally controlled optical switching [8-11]. Nevertheless, surface bound fluorescence assays require solid supports (microbeads, AFM cantilevers, glass substrates, etc.), where fluorophores are not only excited by the incident light, but are also affected by secondary field effects induced at the interface boundaries. Since excited fluorophores polarize their vicinity, they give rise to phenomena such as energy transfer, resonant coupling or shifted angular distribution of fluorescence emission [12-16]. Even though these processes are short ranged, as they predominantly originate from dipole–dipole coupling ($\propto R^{-6}$), they can significantly affect the observable fluorescence emission. Therefore, a profound knowledge of these effects plays a key role in the acquisition and interpretation of data obtained with combined single-molecule mechano-optical setups.

Results and Discussion

The distance dependence of the electrodynamical coupling between a single dipole emitter located near an air–glass interface and a gold coated AFM cantilever tip was elucidated by means of a combined TIRFM–AFM approach based on a home-built AFM setup that was mounted on an inverted microscope (Figure 1a). The cantilever position relative to the sample surface can be set and adjusted with subnanometer precision. The sample is irradiated by a p-polarized Ar^+-Laser at an angle of total reflection, resulting in an evanescent wave constrained close to the surface [17]. The fluorescence emission emanating from the sample is detected by an image-intensified charge-coupled device (ICCD) camera (Figure 1b).

To investigate the dependence of the fluorescence emission from a single quantum dot on the distance from the gold coated cantilever tip apex, we acquired the fluorescence emission intensity at several *z*-distances. After each 2.5 nm step, 200 frames with an exposure time of 50 ms were obtained. The measurements suffer from the typical intermittent fluorescence emission of quantum dots, often referred to as blinking, but the effect on the results was reduced by binning three distance steps together. The integrated fluorescence intensity shows a pronounced distance dependence for gap sizes below 75 nm (Figure 2).

At close proximity to the surface (<20 nm) we found a distinct decrease of the fluorescence emission, which was completely quenched at surface contact. This finding is attributed to energy transfer between the fluorophore and the gold tip. Analogous results for colloidal gold nanoparticles and organic dye mole-

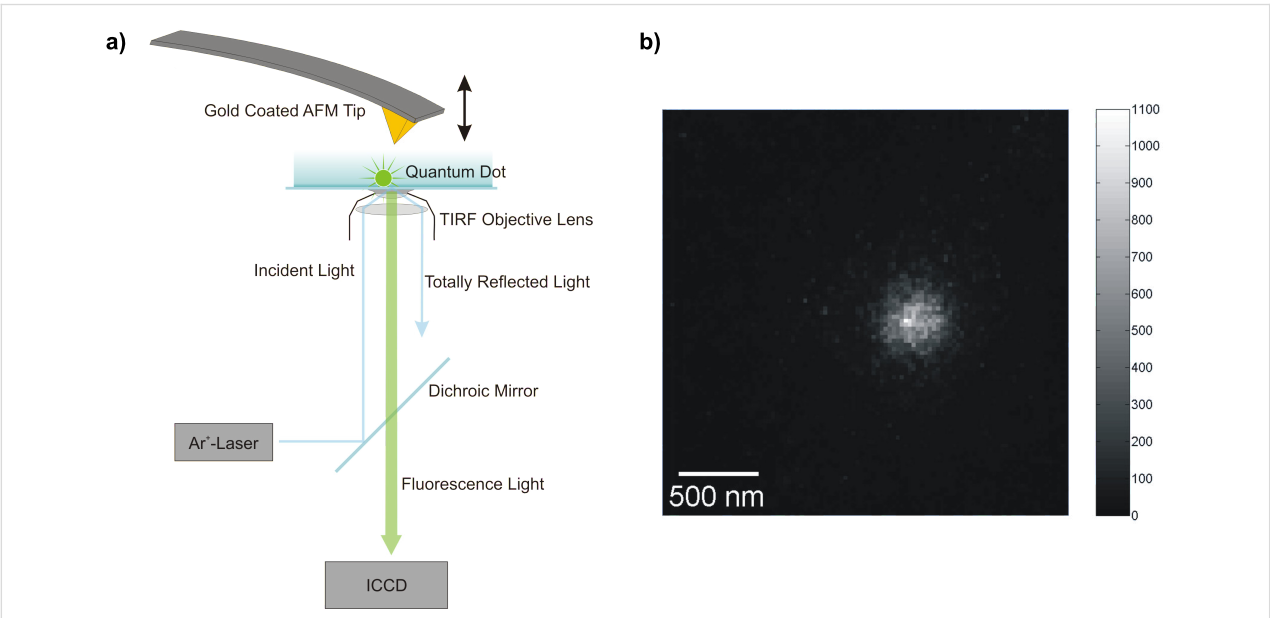

Figure 1: a) Schematic image of the combined TIRFM–AFM setup. The AFM is placed on top of an inverted microscope. The subnanometer spatial resolution of the AFM piezo drive allows precise positioning relative to the sample surface. The incident laser is directed towards the sample surface at an angle of total reflection. The intensity of the evanescent wave projecting beyond the cover slip decreases exponentially. An image-intensified CCD camera detects the fluorescence light. b) Single CCD camera frame of a single quantum dot.

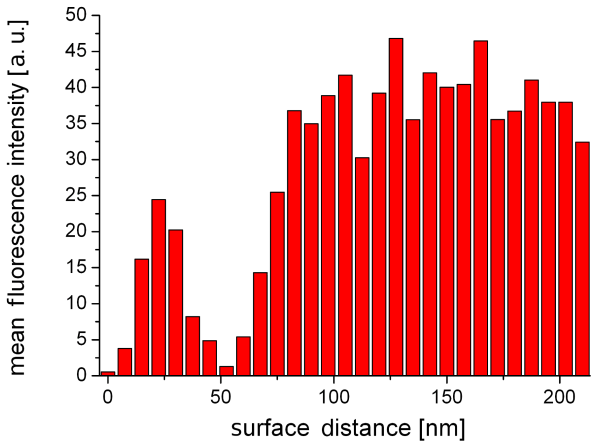

Figure 2: Integrated fluorescence intensity of a single quantum dot as a function of tip distance. The bin size is 7.5 nm (3 × step size of 2.5 nm).

cules were obtained and discussed recently [13]. At larger gap sizes we observed a significant distance dependence of the fluorescence emission. A relative fluorescence maximum at $z \approx$ 22 nm was followed by a drop of the emission intensity at a surface distance of approximately 52 nm. Further retracting led to a recovery of the fluorescence emission until the impact of the tip became negligible. Our experimental findings are well supported by the ensemble data of Govorov et al. [18] who studied the coupling between colloidal gold nanoparticles and CdTe quantum dots coupled by polymer linkers as a function of linker length. The enhanced fluorescence as well as the second minimum must be explained on the basis of two interfering processes caused by the nonhomogeneity of the medium. Firstly, we consider the coupling between the cantilever tip and the evanescent sample illumination: The dipolar coupling between the incident light and the gold tip leads to a field enhancement confined at the tip apex. Secondly, we have to consider the dipolar coupling between the fluorophore and the tip, which either leads to fluorescence enhancement due to resonant coupling or fluorescence quenching as a result of energy transfer. Unfortunately, these effects cannot be observed separately. Hence, to gain a detailed insight into the contribution of the involved processes, we performed multiple dipole (MDP) calculations at tip distances from 5–500 nm. Furthermore, several tip shapes with opening angles ranging from 18–46° were modelled. We evaluated the observable intensity of the fluorescence emission I as a function of tip distance, in a three step procedure. Firstly, we examined the interaction between the cantilever tip apex and the incident light. The relative excitation rate Γ_{exc} (Equation 2) of a single dipole emitter that is oriented perpendicular to the sample surface was estimated for several tip distances. Secondly, to evaluate the relative quantum yield Q (Equation 3), one has to separate the impact of the coupling between the dipole emitter and the tip apex from that of the secondary fields. Therefore, we calculated the observable fluorescence emission I (Equation 4) of a single dipole emitter with Γ_{exc} = constant. Thirdly, to approximate the experimental data, the distance dependence of Γ_{exc} was considered when computing I.

We found a nontrivial dependence of the coupling between the evanescent field and the AFM cantilever tip (Figure 3a). At small tip distances a strong field enhancement is observed that rapidly decreases with growing gap size. This strong distance dependence is characteristic of dipole–dipole coupling effects. Upon further retraction from the surface Γ_{exc} exhibits a relative minimum at tip distances between 35 and 60 nm. The extent of the drop is moderate (approx. 25%) for all tip shapes. Notably,

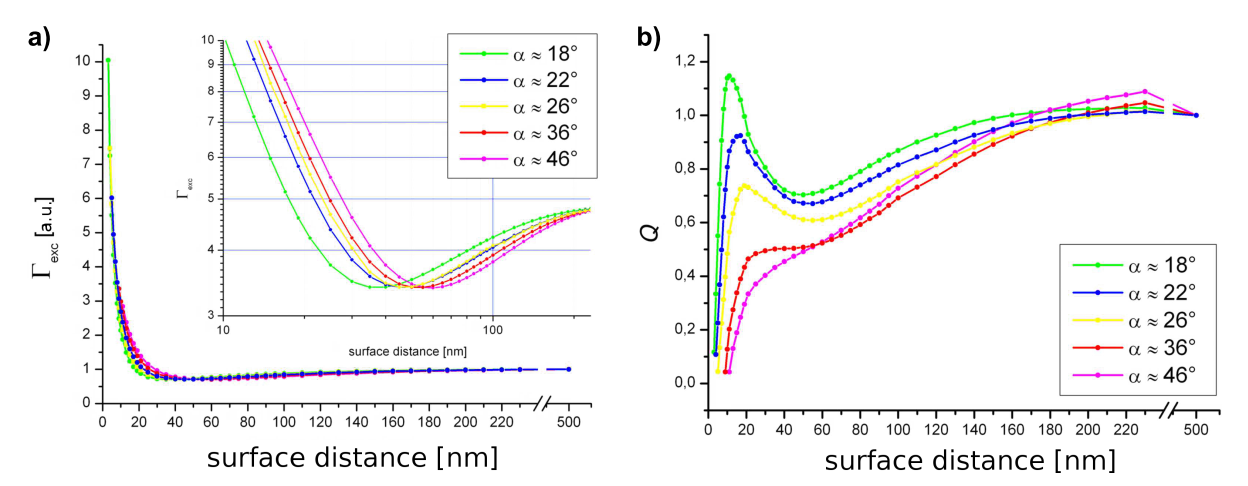

Figure 3: Separated contributions to the external control of fluorescence emission, for several different tip shapes. a) Relative excitation rate Γ_{exc} (inset: semilog plot) at an illumination angle of 45°. b) Relative quantum yield calculated for constant excitation.

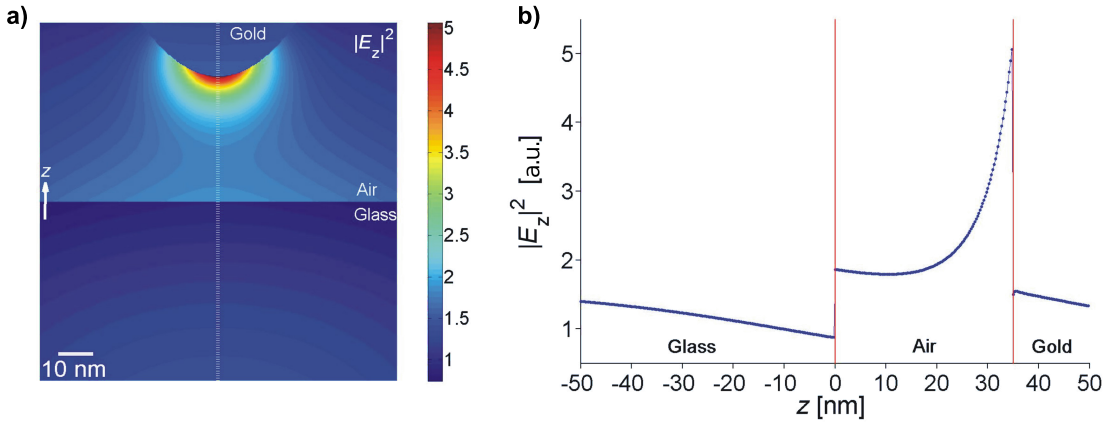

Figure 4: a) Distribution of the field intensity $|E_z|^2$ near an evanescently illuminated gold tip 35 nm above an air–glass interface. b) Field intensity $|E_z|^2$ along the symmetry axis.

the minimum occurs at smaller surface distances for sharp tips. This effect is likely to stem from interference between mirror dipoles in the glass induced by the strong field confined at the tip apex (Figure 4). Further withdrawing of the tip successively diminishes the impact of such tip-induced effects.

The electrodynamic coupling between a dipole emitter and the tip at constant Γ_{exc} is presented in Figure 3b.

We observe almost complete fluorescence quenching at close proximity to the surface, which is in excellent agreement with recent findings [12,13]. The fluorescence emission, however, does not increase monotonically as the tip is withdrawn from the surface. Instead, we observed an enhanced fluorescence emission at approximately 20 nm, which is followed by partial fluorescence quenching at a gap size of about 50–60 nm. Both effects become less pronounced for larger cone angles. Equally, fluorescence enhancement as well as quenching can be attributed to (resonant) exciton–plasmon coupling. To obtain the observable fluorescence emission *I*, we now consider the variability of fluorophore excitation (Figure 5). Comparison of the theoretical results with our experimental data shows a very good agreement. The surface distances for fluorescence enhancement as well as partial quenching were validated.

Discrepancies between experimental and theoretical data are most likely due to the assumed simplifications. More elaborate approaches that use higher orders of the multipole expansion or lower symmetry may give more precise results. Generally, with our comparably simple model we were able to validate the experimental results qualitatively. Moreover, we were also able to separate and quantify the influence of the enhanced field confined to the tip apex and the impact excitation plasmon coupling on the detectable fluorescence intensity.

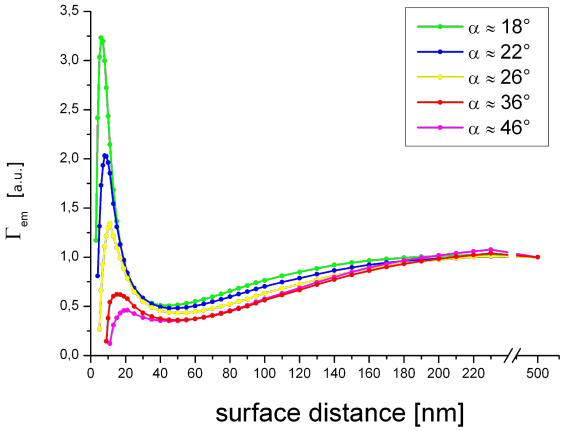

Figure 5: Relative emission rate for several surface distances and tip opening angles estimated by the observable fluorescence emission intensity *I*.

Furthermore, we found a considerable shift in the angular distribution of the fluorescence emission (Figure 6) induced by the coupling between the tip apex and the dipole emitter.

The angle of highest emission intensity (arrows) lies within the detection angle of the objective lens for the retracted tip, however, it successively shifts beyond the detection angle for decreasing gap size. Consequently, the observed quenching of the fluorescence intensity is not only due to an absolute reduction of the emission rate, but also because of the successive decrease of the detection efficiency I_{det}/I_{tot} of the objective lens (Figure 7). This finding is well supported by recently published experimental and theoretical data [16]. Yet, in our case the impact of this relative fluorescence quenching is negligible.

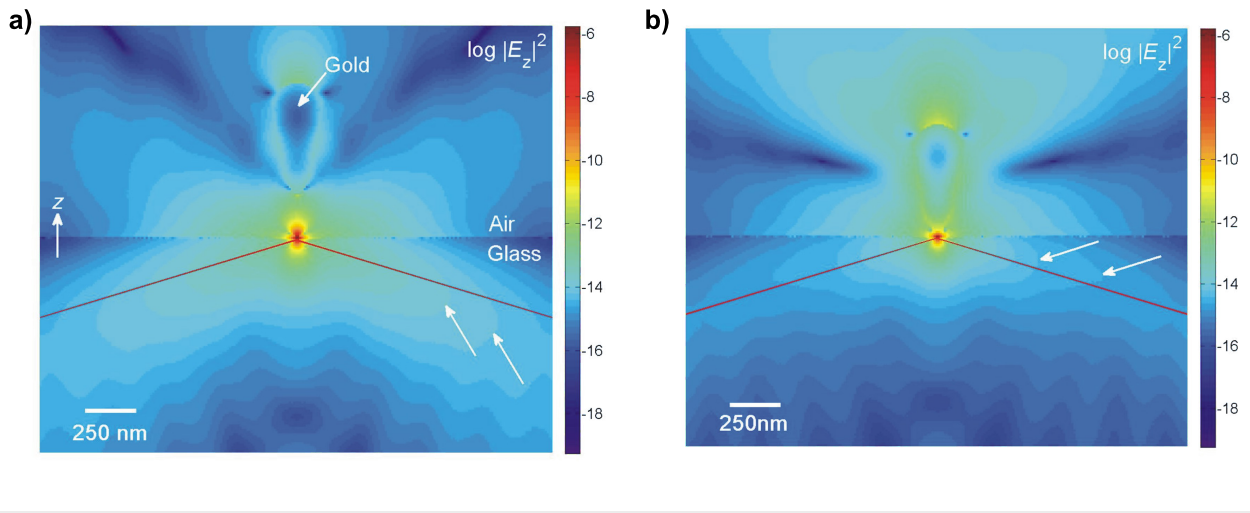

Figure 6: Logarithmic field distribution of a single dipole emitter perpendicular to a glass–air interface for tip distances of a) 200 nm and b) 5 nm. The tip opening angle is 18°. The microscope objective lens detection angle (red) illustrates the change in the angular emission pattern at different tip distances. The direction of highest emission intensity (arrows) shifts to larger angles at smaller tip distances.

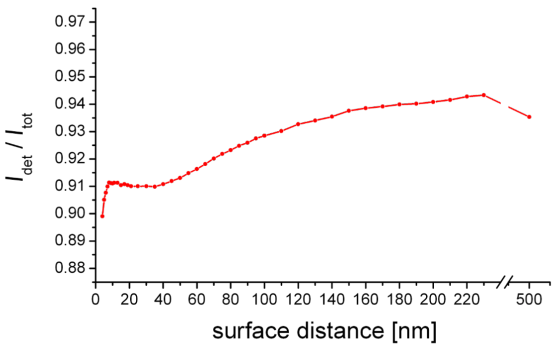

Figure 7: Detection efficiency of an objective lens (numerical aperture (NA) = 1.45) as a function of tip distance.

Conclusion

We presented experimental data and simulations for the fluorescence emission control of single quantum dots by the external intervention of a gold-coated AFM tip. The acquired luminescence data exhibited a nontrivial dependence on the tip distance. Modelling the system with a MDP approach unveiled the multivalent interplay of incident and emitted electromagnetic fields at the boundary of different media.

Our results represent an important step en route towards being able to controllably address and manipulate fluorescently labelled individual molecules. Furthermore, the MDP approach is very well suited for qualitative ad hoc validation of experimental data. The significance of dipolar coupling in single molecule manipulation assays was demonstrated. Conceivable applications range from microarrays to controlled manipulation of single molecules. The strong distance dependence of dipole–dipole coupling combined with the subnanometer resolution of AFM holds great promises to yield as yet unattainable information about the interplay of individual molecules, such as their molecular recognition mechanisms [19-24], folding pathways [25] or micro environments [26].

Experimental

TIRF–AFM Setup

All experimental work was performed on a combined total internal reflection fluorescence microscopy (TIRFM) atomic force microscope (AFM) setup. The homebuilt AFM head is mounted on an inverted Microscope Axiovert 100 (Carl Zeiss, Oberkochen, Germany) with a high numerical aperture objective lens (Olympus Plapo 100× TIRFM, NA = 1.45, Olympus, Tokyo, Japan). Fluorescence detection was performed by a liquid-cooled image-intensified charge-coupled device (ICCD) camera (I-PentaMAX, Roper Scientific, Trenton, NJ USA). Fluorescence excitation was achieved by an Ar^+-laser (continuous wave, 10 mW, 488 nm). For excitation power control, neutral density filters with optical density from 0.3–1.5 were installed in the laser path. A detailed description of the setup was published recently [27,28].

The cantilever was approached to the surface in 2.5 nm steps. After each step a series of 200 images was acquired with an exposure time of 50 ms. During the approach to the surface, the cantilever deflection was sampled. The exact tip surface distance was evaluated by linear approximation of the free and contact regimes of the deflection versus piezo extension plot.

Sample and cantilever preparation

Microscope glass cover slips (24 × 24 mm^2, Menzel, Germany) were washed with acetone, ethanol and water and dried gently with nitrogen. To remove any fluorescent adsorbates, the substrates were dipped in boiling piranha solution (1:3 sulphuric acid 96% and hydrogen peroxide 30%) for one minute, rinsed thoroughly with MilliQ filtered water and dried with nitrogen. After cleaning, hydrophobic fluorescent CdSe/ZnS nanoparticles [29] with a spectral emission maximum at 585 nm were diluted in *n*-heptane (Sigma Aldrich), microdispensed to the glass cover slips and dried. Sparsely covered (<1 quantum dot per 25 μm^2) samples allowed the addressing of individual fluorophores.

Silicon AFM cantilevers (PPP-NCHR, Nanosensors, Neuchatel, Switzerland) were washed with acetone, ethanol and water and dried in a gentle flow of nitrogen. Subsequently, a 50 nm thick gold layer was evaporated on the cantilevers at a rate of 0.2 nm/s.

Multiple dipole (MDP)-Simulation

To calculate the electromagnetic field distribution near interface boundaries one has to solve Maxwell's equations with regard to the boundary conditions. These are derived in common electrodynamics textbooks [30]. As our system is more complex than planar interfaces, analytical approaches are meaningless. Therefore, we selected a simplification of the multiple multipole (MMP) method [31,32], which is a semi-analytical approach to compute field distributions in arbitrarily shaped piecewise homogeneous, isotropic and linear media. In brief: The electromagnetic fields at the domain boundaries are approximated numerically whereas the field strength within the domain can be computed analytically. The system is modelled by choosing a set of matching points on the domain boundary. Multipole emitters along each side of the interface induce an electromagnetic field exclusively in the opposing domain. The strength of each emitter is approximated numerically in such a way that the boundary conditions are satisfied at the matching points. Superposition of all multipole emitter contributions results in a field distribution that is a solution of Maxwell's equations and satisfies the boundary conditions. To limit the demand for processing power and memory we made some simplifications: Firstly, we assumed cylindrical symmetry (along the *z*-axis). The sample is evanescently illuminated by p-polarized light leading to an enhancement of the field component normal to the interface. Thus, the polarization beyond the surface is almost parallel to the *z*-axis. The contribution parallel to the surface can therefore be neglected. Secondly, we omitted the silicon–gold interface. In principle, our tip surface geometry can be compared to a Kretschman–Raether configuration [33]. Even though this model is only applicable to planar geometries, it can serve as an ad hoc approximation for our more complex system. Consequently, the surface plasmon decay length *z* perpendicular to the boundary surface can be approximated by the following expression:

$$z = \frac{\lambda}{2\pi}\sqrt{\frac{\mathrm{Re}(\varepsilon_{\mathrm{Au}}) + \varepsilon_{\mathrm{glass}}}{\mathrm{Re}(\varepsilon_{\mathrm{Au}})}} \tag{1}$$

where λ denotes the wavelength, and $\varepsilon_{\mathrm{Au}}$ and $\varepsilon_{\mathrm{glass}}$ the dielectric functions of gold and glass, respectively. With the corresponding dielectric functions (see below) we determined a plasmon decay length of $z \approx 59$ nm, which is of the order of the thickness of the gold layer on the tip. Hence, the influence of the silicon tip core should be insignificant. Thirdly, we only considered the contribution of dipole emitters to the field distribution and omitted higher orders. Consequently, this approach will be referred to as multiple dipole (MDP) method.

MDP calculations were performed for various tip shapes and surface distances. As quantum mechanical effects such as electron transfer are not considered in this classical approach, the minimum tip surface distance was set to 5 nm. The tip geometry was modelled by cones with opening angles in the range of 18–46°; as tip apex a second order polynomial was appended continuously. The angle of sample illumination was set to 45°, which is well above the critical angle of total reflection (approx. 43°) at an air–glass interface. Corresponding to the experiment, the wave lengths for illumination and fluorescence emission were set to 488 nm and 585 nm, respectively. The dielectric functions ε of the corresponding medium at the given wavelengths are: $\varepsilon_{\mathrm{air}}(488\ \mathrm{nm}) = \varepsilon_{\mathrm{air}}(585\ \mathrm{nm}) = 1$, $\varepsilon_{\mathrm{glass}}$ (488 nm) = 2.34, $\varepsilon_{\mathrm{glass}}$ (585 nm) = 2.33, $\varepsilon_{\mathrm{Au}}$ (488 nm) = −1.33 + 3.06i and $\varepsilon_{\mathrm{Au}}$ (585 nm) = −7.7 + 1.06i [34].

In order to quantify the fluorophore excitation, we computed the relative excitation rate Γ_{exc} (Equation 2), which we define as the quotient of the excitation rate of the undisturbed system γ^0_{exc} (surface distance >500 nm) and the excitation rate γ_{exc} in proximity to the cantilever tip.

$$\Gamma_{\mathrm{exc}} = \frac{\gamma_{\mathrm{exc}}}{\gamma^0_{\mathrm{exc}}} = \frac{\left|E_{\mathrm{exc}}\right|^2}{\left|E^0_{\mathrm{exc}}\right|^2} \tag{2}$$

In terms of electric field strength, this can be expressed as the quotient of the corresponding field intensities at the location of the fluorophore. Accordingly, we define the relative emission rate Γ_{em} (Equation 3) of a single fluorophore by the product of Γ_{exc} and relative quantum yield *Q*.

$$\Gamma_{em} = \Gamma_{exc}\, Q \quad \text{with} \quad Q = \frac{q}{q_0} \tag{3}$$

where q and q_0 are the apparent and intrinsic quantum yield, respectively. Generally, the shift of the quantum yield can be described in terms of the radiative and nonradiative decay rates (γ_r, γ_{nr}) as follows:

$$q = \frac{1-\gamma_{nr}}{\gamma_{nr}+\gamma_r} \tag{4}$$

The coupling between a dipole emitter and a sharp metallic tip results in an increase of γ_r [32,35]. Yet, the degree of luminescence enhancement is inherently limited by the fluorophore's intrinsic quantum yield q_0, i.e., strong luminescence enhancement can only be observed for low q_0 ($\gamma_{nr} >> \gamma_r$).

In order to quantify Q, namely the impact of dipolar coupling between the gold tip apex and the fluorophore in the absence of any secondary fields, the detectable fluorescence emission I for arbitrary but constant Γ_{exc} was calculated. The normalized intensity of the electric field distribution $|E_{em}|^2 / |E_{em}^0|^2$ propagating in the lower glass half-space was integrated over a sphere (Equation 4). To rule out the contribution of the nonpropagating near-field, the sphere radius was set to R = 1000 µm. The integration limit of the polar angle Θ_{max} is given by the numerical aperture (NA = $n \cdot \sin \Theta_{max}$) of the objective lens. Consistent with the experiment we assumed a refractive index n = 1.51, and NA = 1.45.

$$I = R^2 \int_0^{2\pi} \int_0^{\theta_{max}} \frac{|E_{em}|^2}{|E_{em}^0|^2} \sin\theta \, d\theta \, d\varphi \tag{5}$$

The approximation of the experimental data was made analogously, however, the distance dependence of Γ_{exc} was taken into consideration.

Acknowledgements

This work was financially supported by the Deutsche Forschungsgemeinschaft (DFG), SFB 613. We are also grateful for fruitful discussions with Prof. Dr. Robert Ros and Dr. Rainer Eckel.

References

1. Förster, T. *Ann. Phys.* **1948,** *437,* 55–75. doi:10.1002/andp.19484370105
2. Stryer, L.; Haugland, R. P. *Proc. Natl. Acad. Sci. U. S. A.* **1967,** *58,* 719–726. doi:10.1073/pnas.58.2.719
3. Root, D. D.; Shangguan, X.; Xu, J.; McAllister, M. A. *J. Struct. Biol.* **1999,** *127,* 22–34. doi:10.1006/jsbi.1999.4127
4. Kapanidis, A. N.; Lee, N. K.; Laurence, T. A.; Doose, S.; Margeat, E.; Weiss, S. *Proc. Natl. Acad. Sci. U. S. A.* **2004,** *101,* 8936–8941. doi:10.1073/pnas.0401690101
5. Binnig, G.; Quate, C. F.; Gerber, C. *Phys. Rev. Lett.* **1986,** *56,* 930–933. doi:10.1103/PhysRevLett.56.930
6. Ashkin, A.; Dziedzic, J. M.; Bjorkholm, J. E.; Chu, S. *Opt. Lett.* **1986,** *11,* 288–290. doi:10.1364/OL.11.000288
7. Hugel, T.; Holland, N. B.; Cattani, A.; Moroder, L.; Seitz, M.; Gaub, H. E. *Science* **2002,** *296,* 1103–1106. doi:10.1126/science.1069856
8. Chudakov, D. M.; Verkhusha, V. V.; Staroverov, D. B.; Souslova, E. A.; Lukyanov, S.; Lukyanov, K. A. *Nat. Biotechnol.* **2004,** *22,* 1435–1439. doi:10.1038/nbt1025
9. Eckel, R.; Walhorn, V.; Pelargus, C.; Martini, J.; Enderlein, J.; Nann, T.; Anselmetti, D.; Ros, R. *Small* **2007,** *3,* 44–49. doi:10.1002/smll.200600130
10. Habuchi, S.; Ando, R.; Dedecker, P.; Verheijen, W.; Mizuno, H.; Miyawaki, A.; Hofkens, J. *Proc. Natl. Acad. Sci. U. S. A.* **2005,** *102,* 9511–9516. doi:10.1073/pnas.0500489102
11. Lounis, B.; Moerner, W. E. *Nature* **2000,** *407,* 491–493. doi:10.1038/35035032
12. Buchler, B. C.; Kalkbrenner, T.; Hettich, C.; Sandoghdar, V. *Phys. Rev. Lett.* **2005,** *95,* 063003. doi:10.1103/PhysRevLett.95.063003
13. Anger, P.; Bharadwaj, P.; Novotny, L. *Phys. Rev. Lett.* **2006,** *96,* 113002. doi:10.1103/PhysRevLett.96.113002
14. Gersen, H.; García-Parajó, M. F.; Novotny, L.; Veerman, J. A.; Kuipers, L.; van Hulst, N. F. *Phys. Rev. Lett.* **2000,** *85,* 5312–5315. doi:10.1103/PhysRevLett.85.5312
15. Lee, J.; Govorov, A. O.; Dulka, J.; Kotov, N. A. *Nano Lett.* **2004,** *4,* 2323–2330. doi:10.1021/nl048669h
16. Ruckstuhl, T.; Enderlein, J.; Jung, S.; Seeger, S. *Anal. Chem.* **2000,** *72,* 2117–2123. doi:10.1021/ac991358k
17. Axelrod, D.; Thompson, N. L.; Burghardt, T. P. *J. Microsc. (Oxford, U. K.)* **1983,** *129,* 19–28. doi:10.1111/j.1365-2818.1983.tb04158.x
18. Lee, J.; Govorov, A. O.; Kotov, N. A. *Angew. Chem., Int. Ed.* **2005,** *44,* 7439–7442. doi:10.1002/anie.200501264
19. Dammer, U.; Popescu, O.; Wagner, P.; Anselmetti, D.; Güntherodt, H. J.; Misevic, G. N. *Science* **1995,** *267,* 1173–1175. doi:10.1126/science.7855599
20. Eckel, R.; Ros, R.; Decker, B.; Mattay, J.; Anselmetti, D. *Angew. Chem., Int. Ed.* **2005,** *44,* 484–488. doi:10.1002/anie.200461382
21. Eckel, R.; Wilking, S. D.; Becker, A.; Sewald, N.; Ros, R.; Anselmetti, D. *Angew. Chem., Int. Ed.* **2005,** *44,* 3921–3924. doi:10.1002/anie.200500152
22. Florin, E. L.; Moy, V. T.; Gaub, H. E. *Science* **1994,** *264,* 415–417. doi:10.1126/science.8153628
23. Lee, G. U.; Chrisey, L. A.; Colton, R. J. *Science* **1994,** *266,* 771–773. doi:10.1126/science.7973628
24. Ros, R.; Schwesinger, F.; Anselmetti, D.; Kubon, M.; Schäfer, R.; Plückthun, A.; Tiefenauer, L. *Proc. Natl. Acad. Sci. U. S. A.* **1998,** *95,* 7402–7405. doi:10.1073/pnas.95.13.7402
25. Rief, M.; Gautel, M.; Oesterhelt, F.; Fernandez, J. M.; Gaub, H. E. *Science* **1997,** *276,* 1109–1112. doi:10.1126/science.276.5315.1109
26. Ebenstein, Y.; Mokari, T.; Banin, U. *J. Phys. Chem. B* **2004,** *108,* 93–99. doi:10.1021/jp036135j

27. Eckel, R.; Walhorn, V.; Pelargus, C.; Martini, J.; Anselmetti, D.; Ros, R.; Nann, T. *Proc. SPIE* **2006,** *6092,* 609206. doi:10.1117/12.645067
28. Walhorn, V.; Schulz, O.; Pelargus, C.; Anselmetti, A.; Ros, R. *Proc. SPIE* **2007,** *6444,* 644406. doi:10.1117/12.700631
29. Nann, T. *Chem. Commun.* **2005,** 1735–1736. doi:10.1039/B414807J
30. Jackson, J. D. *Classical Electrodynamics;* Wiley: New York, 1998.
31. Hafner, C. *Electr. Eng.* **1986,** *69,* 321–325. doi:10.1007/BF01574747
32. Novotny, L.; Hecht, B. *Principles of nano-optics;* Cambridge Univ. Press, 2006.
33. Kretschmann, E.; Raether, H. *Z. Naturforsch.* **1968,** *23a,* 2135–2136.
34. Weber, M. J. *Handbook of Optical Materials. Laser and Optical Science and Technology;* CRC Press, 2002.
35. Zhang, D.; Heinemeyer, U.; Stanciu, C.; Sackrow, M.; Braun, K.; Hennemann, L. E.; Wang, X.; Scholz, R.; Schreiber, F.; Meixner, A. J. *Phys. Rev. Lett.* **2010,** *104,* 056601. doi:10.1103/PhysRevLett.104.056601

License and Terms

Beilstein Journal of Nanotechnology

How to remove the influence of trace water from the absorption spectra of SWNTs dispersed in ionic liquids

Juan Yang*, Daqi Zhang and Yan Li*

Full Research Paper

Open Access

Address:
Beijing National Laboratory for Molecular Sciences, State Key Laboratory of Rare Earth Materials Chemistry and Applications, Key Laboratory for the Physics and Chemistry of Nanodevices, College of Chemistry and Molecular Engineering, Peking University, Beijing 100871, China

Email:
Juan Yang* - yang_juan@pku.edu.cn; Yan Li* - yanli@pku.edu.cn

* Corresponding author

Keywords:
absorption spectra; ionic liquids; quantitative analysis; single-walled carbon nanotubes

Beilstein J. Nanotechnol. **2011,** *2,* 653–658.
doi:10.3762/bjnano.2.69

Received: 30 June 2011
Accepted: 16 September 2011
Published: 30 September 2011

This article is part of the Thematic Series "Nanophotonics, nano-optics and nanospectroscopy".

Guest Editor: A. J. Meixner

Abstract

Single-walled carbon nanotubes (SWNTs) can be efficiently dispersed in the imidazolium-based ionic liquids (ILs), at relatively high concentration, with their intrinsic structure and properties retained. Due to the hygroscopicity of the ILs, water bands may be introduced in the absorption spectra of IL-dispersed SWNTs and cause problems in spectral deconvolution and further analysis. In order to remove this influence, a quantitative characterization of the trace water in $[BMIM]^+[PF_6]^-$ and $[BMIM]^+[BF_4]^-$ was carried out by means of UV–vis-NIR absorption spectroscopy. A simple yet effective method involving spectral subtraction of the water bands was utilized, and almost no difference was found between the spectra of the dry IL-dispersed SWNT samples treated under vacuum for 10 hours and the spectra of the untreated samples with subtraction of the pure water spectrum. This result makes it more convenient to characterize SWNTs with absorption spectra in the IL-dispersion system, even in the presence of trace amount of water.

Introduction

The so-called room-temperature ionic liquids (ILs) are a group of room-temperature molten salts that are composed of specific cations and anions [1,2]. Compared to conventional volatile organic solvents, they are nonpolluting, recyclable green solvents with remarkable physical and chemical properties, including low melting points, nondetectable vapor pressure, excellent stability, etc. [1-3]. In addition, by varying the structures of the component cations or anions the properties of ILs can be easily adjusted. Due to all the above advantages, ILs have attracted significant attention in many research areas such as electrochemistry [4,5], and chemical reactions and separations [6-9].

In 2003, Fukushima et al. [10] found that by mixing together and mechanically grinding the single-walled carbon nanotubes with imidazolium-based ILs, a thermally stable bucky gel can be formed with SWNTs untangled from the heavily entangled bundles. Since the poor solubility and low dispersibility of SWNTs in conventional solvents have hindered the processing and applications of SWNTs for more than a decade, this phenomenal discovery showed a new direction for the dispersal of SWNTs with high concentrations (~1 wt %), which are about two or three orders of magnitude higher than other suspension methods, including surfactant dispersion [11,12], DNA wrapping [13,14], polymer wrapping [15], and sidewall covalent functionalization [16,17]. As it does not involve any rigorous sonication, centrifugation, or chemical reaction, the structure of the SWNTs is not damaged. Moreover, a previous study [18] has shown that the electronic structure and properties of SWNTs are retained since there is no strong interaction, but only weak van der Waals interaction, between SWNTs and ILs. Therefore, imidazolium-based ILs are ideal media for the investigation of the properties and applications of SWNTs.

As it is well known that ILs are hygroscopic and that the amount of water absorbed in ILs can significantly affect the physical properties, such as polarity, viscosity, conductivity, and solubility [19-21], much research [21,22] have been carried out to study the states of water dissolved in ILs at the molecular level in order to achieve better understanding of ILs. It was found that the up-taken water interacts strongly through hydrogen bonding with the anions of the ILs, and for 1-butyl-3-methylimidazolium ($[BMIM]^+$)-based ILs, $[BF_4]^-$ provides stronger interactions than $[PF_6]^-$ and more water is absorbed in $[BMIM]^+[BF_4]^-$ than in $[BMIM]^+[PF_6]^-$ [22].

In the case of IL-dispersed SWNTs, the presence of water not only changes the properties of the IL but also affects the spectroscopic characterization of the dispersed SWNTs. The optical transitions of SWNTs occur when the energy of the incident radiation matches the energy gap between the van Hove singularities of SWNTs. For HiPco samples, in which the diameter of the nanotubes is about 0.7–1.1 nm, the E_{11} and E_{22} transitions of the semiconducting nanotubes are in the ranges of 850–1600 nm and 600–800 nm, respectively, while the E_{11} transitions of the metallic nanotubes are of 400–650 nm [23]. As the E_{11} transitions of semiconducting nanotubes are of the lowest energy and do not overlap with higher energy transitions, the deconvolution of the absorption bands in this region with respect to their chiralities is of great importance in the quantitative analysis of bulk SWNT samples. However, because water has strong absorption bands in the near-infrared (NIR) region where the E_{11} of semiconducting SWNTs lies, even a trace amount of water dissolved in an IL may introduce notable peaks in the SWNTs absorption spectra, which will affect the deconvolution and quantitative analysis significantly. Therefore, treatment of the ILs under high vacuum, immediately before taking the spectra, is necessary to reduce the peaks introduced by the trace amount of water. Even so, the water bands are still inevitable because ILs will absorb water from the atmosphere during the period of time it takes to collect the spectra. In order to correct for the influence of water in the absorption spectra of SWNTs dispersed in ILs and furthermore to avoid an inconvenient sample treatment procedure, a simple but effective method is needed.

In this paper, a study of the UV-vis-NIR spectra of $[BMIM]^+$ based ILs with different amounts of added water is described, and a quantitative characterization of the spectra with respect to the water concentrations is made. A spectral-subtraction method is used to remove the water bands from the absorption spectra of IL-dispersed SWNTs and the results are compared with the corresponding spectra of water-free samples. The exact amount of water taken up in the untreated sample is calculated consequently.

Experimental

The $[BMIM]^+[PF_6]^-$ and $[BMIM]^+[BF_4]^-$ ILs were purchased from Henan Lihua Pharmaceutical Co. Ltd., China. The as-received ILs were first treated under 10^{-5} Pa vacuum for 10 h to remove the absorbed water. Different amount of water (produced by Millipore SimPak 1, resistivity ≥18.2 MΩ cm) was then added to the dry ILs through a microsyringe. The water concentrations were calculated by the volume of added water and the weights of the dry ILs.

The SWNT suspensions in ILs were prepared by mechanically grinding ~0.1 mg HiPco SWNTs and ~8.0 g untreated ILs together in an agate mortar for 20 min. The as-prepared samples ("untreated" samples) were used directly for spectral measurements. As comparison, the mixtures were then treated under 10^{-5} Pa vacuum for 10 h and the corresponding spectra of the "dry" samples were collected with dehydrates present in the sample chamber to maximally avoid the absorption of water vapor from the atmosphere.

The UV–vis-NIR absorption spectra were collected in a cell with a 1.0 cm path length with a PerkinElmer Lambda 950 spectrophotometer. A scan rate of 140 nm/min with a step size of 0.5 nm was typically used. The spectra for ILs were recorded in the 300–2000 nm region while those for SWNTs-ILs were measured in the 300–1800 nm region. The program Origin 8.0 was used for data analysis.

Results and Discussion

Figure 1 illustrates the UV–vis-NIR spectra of $[BMIM]^+[PF_6]^-$ with a water concentration of 0.266 M, where dry $[BMIM]^+[PF_6]^-$ is used as a reference and thus its absorption is subtracted out automatically. The blue spectrum is a 20-times magnification of the red original spectrum in order to enlarge the weak signals. Since HiPco SWNTs only show absorption bands up to 1800 nm, it is the 300–2000 nm spectral region that we are most interested in. The negative bands below 450 nm and in the spectral region of 1600–1750 nm are due to the absorption of $[BMIM]^+$ $[PF_6]^-$, which was previously reported [22].

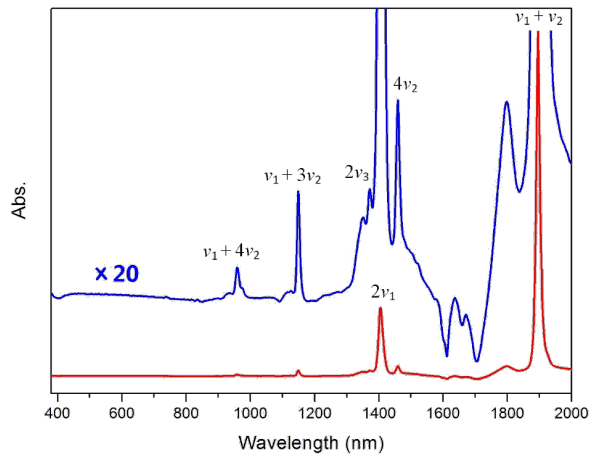

Figure 1: The UV–vis-NIR spectra of water in $[BMIM]^+[PF_6]^-$ with dry $[BMIM]^+[PF_6]^-$ used as a reference. The blue spectrum is a 20-times magnification of the red original spectrum in order to enlarge the weak signals.

In the water spectra two main features are observed at 1405 and 1896 nm, and can be attributed to the first overtone of the O–H symmetric stretching vibration ($2v_1$) and the combination of the O–H symmetric stretching and the angle bending vibrations ($v_1 + v_2$), respectively. The weak band at 1372 nm is assigned as the first overtone of the O–H antisymmetric stretching vibration ($2v_3$). Thus the three fundamental vibrations of water in $[BMIM]^+[PF_6]^-$ can be calculated as v_1 = 3559 cm^{-1}, v_2 = 1715 cm^{-1}, and v_3 = 3644 cm^{-1}, respectively. These numbers match very nicely with other bands in the spectra at 1460, 1149, and 959 nm, with the assignments as $4v_2$, $v_1 + 3v_2$, and $v_1 + 4v_2$, respectively. The $v_1 + 2v_2$ band is expected to be at 1431 nm but is not observed in the spectra. It may be that it is covered by the much more intense band at 1405 nm.

It is well known that for free water molecules the three fundamental vibrational frequencies are v_1 = 3652 cm^{-1}, v_2 = 1595 cm^{-1}, and v_3 = 3756 cm^{-1} [24]. In $[BMIM]^+[PF_6]^-$, water interacts strongly with the $[PF_6]^-$ anion through hydrogen bonding and the structure of water is changed consequently, which leads to the vibrational frequency shifts. In particular, due to the hydrogen bonding between the H atom in water and the F atom in $[PF_6]^-$, the O–H bonds are weakened, and thus the two stretching vibrations move to lower wavenumbers, as expected. The angle bending vibration, on the other hand, shifts to higher frequency because of the increased force constant arising from a more rigid H–O–H structure in the presence of hydrogen bonding.

The strength of the interactions between ILs and water depends mainly on the anions, therefore, ILs with different types of anions have different influence on the structural changes of the water molecule. The absorption spectra of water in $[BMIM]^+[BF_4]^-$ is shown in Figure 2, in which the blue spectrum is again the 20-times magnification of the red original spectrum. From the $2v_1$, $2v_3$, and $v_1 + v_2$ bands observed at 1416, 1383, and 1906 nm the corresponding fundamental vibrational frequencies of water can be calculated as v_1 = 3531 cm^{-1}, v_2 = 1716 cm^{-1}, and v_3 = 3615 cm^{-1}, respectively. The lower O–H stretching and slightly higher H–O–H bending vibrational frequencies suggest stronger interactions of water with $[BMIM]^+[BF_4]^-$ than with $[BMIM]^+[PF_6]^-$.

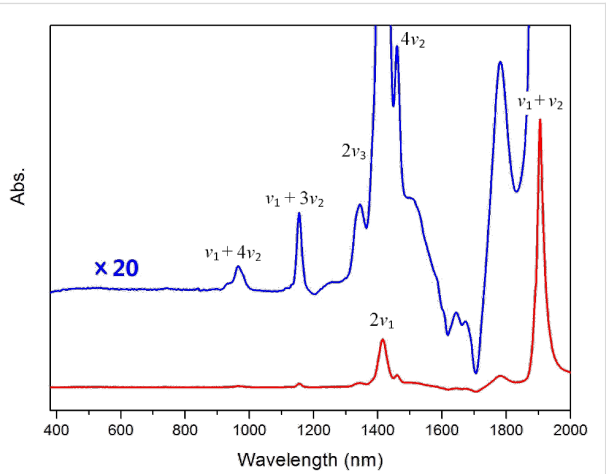

Figure 2: The UV–vis-NIR spectra of water in $[BMIM]^+[BF_4]^-$ with dry $[BMIM]^+[BF_4]^-$ used as reference. The blue spectrum is a 20-times magnification of the red original spectrum in order to enlarge the weak signals.

In Figure 3a the absorption bands at 1405 nm with different amounts of water (0.000, 0.075, 0.086, 0.159, 0.171, and 0.266 M) added to the dry $[BMIM]^+[PF_6]^-$ are plotted. It is clear that with the increased water concentration the band intensity increases concomitantly. After intensity normalization, all five bands exhibit identical frequency and shape, as shown in Figure 3b, indicating that the molecular state of water does not change in the experimental concentration range. The diagram of

band intensity versus water concentration is plotted in the inset of Figure 3a and is fitted by a linear relationship. The intercept is fixed to be zero during the iteration and the resulting linear function is given by

$$A = 0.7966c \quad (1)$$

where A is the absorbance at 1405 nm and c is the water molar concentration (in M) in $[BMIM]^+[PF_6]^-$. An R^2 of 0.99993 indicates excellent linear relationship between A and c. Although the peak areas are suppose to be used in the spectral fitting, the peak intensities could be used instead in this case because both the band shape and position remain unchanged.

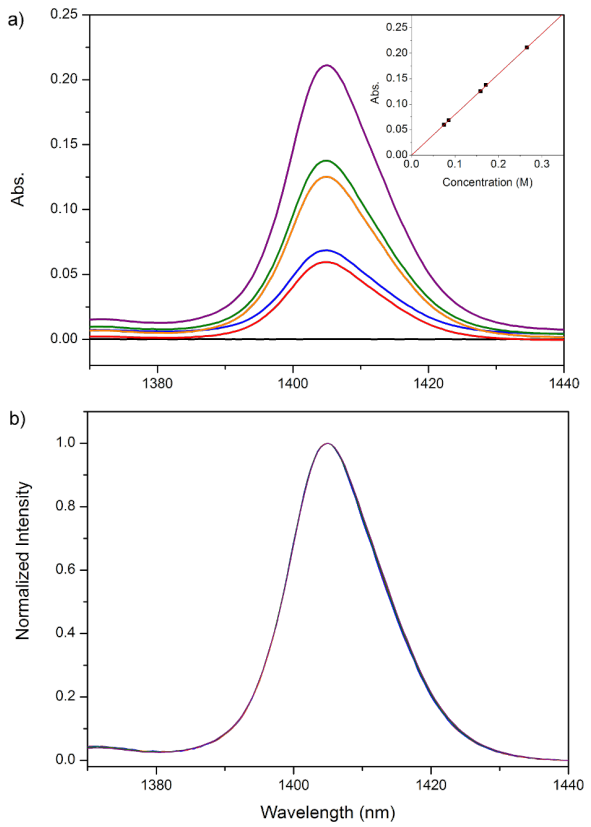

Figure 3: a) The absorption bands at 1405 nm with different amounts of water (from bottom to top: 0.000, 0.075, 0.086, 0.159, 0.171, and 0.266 M) added to dry $[BMIM]^+[PF_6]^-$. The inset plots the linear fitting of band intensity vs. water concentration. b) Intensity normalization of spectra in a).

The absorption spectrum of the untreated $[BMIM]^+[PF_6]^-$-dispersed SWNTs is shown as the black curve in Figure 4, with arrows indicating where the water peaks lie. The well-resolved electronic absorption bands of SWNTs demonstrate good dispersion of nanotubes in this IL. The intensity of the water band at 1405 nm is even higher than that of the nanotube absorption bands, so the deconvolution of the two broad bands close to 1400 nm with respect to semiconducting nanotube chiralities will be affected significantly by this intense water band. In order to remove this effect as well as to quantify the amount of water taken up by the untreated sample, a spectral subtraction method was utilized. To obtain the best fit with the spectrum of the water-free sample, given by the red curve in Figure 4, a specific multiplying parameter was used to scale the water spectrum in Figure 1, which was then subtracted from the spectrum of the untreated sample, the result of which is given by the blue curve. It is clearly shown in Figure 4 that not only the intense band at 1405 nm but also other weak bands can be subtracted out from the spectra at the same time with this best-fitting parameter. The excellent agreement of the blue and red curves verifies the feasibility of this spectral-subtraction method. The water concentration in the untreated sample can be calculated from Equation 1 as 0.0304 M and the corresponding amount of water taken up is 6.40×10^3 ppm.

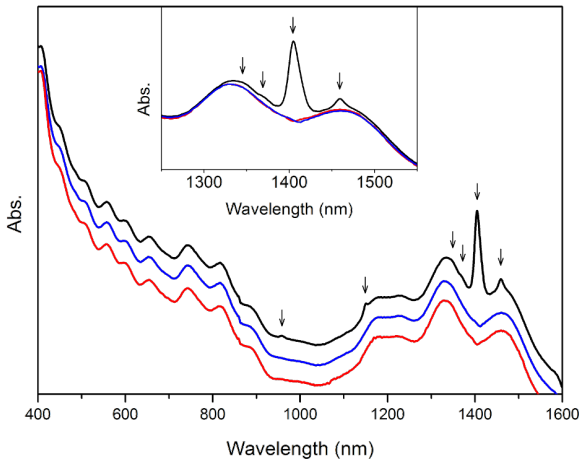

Figure 4: Absorption spectra of $[BMIM]^+[PF_6]^-$-dispersed SWNTs without treatment (black curve), after subtraction of water spectrum (blue curve), and treated under vacuum for 10 hours (red curve). The spectra are offset arbitrarily in the vertical direction for clarity. The inset shows the partially enlarged spectra. Arrows indicate the positions of water bands.

After removal of the water bands from the absorption spectra of SWNTs dispersed in $[BMIM]^+[PF_6]^-$, further analysis of the spectra can be carried out to obtain quantitative information about the bulk SWNT samples. As an example, Figure 5 illustrates the deconvolution of the baseline-corrected spectra in the E_{11} transition region of the semiconducting nanotubes, with the solid black curve as the baseline-corrected spectrum, the dashed red curve as the fitting spectrum, and the solid red curves as the deconvoluted individual peaks corresponding to different chiralities of the semiconducting nanotubes, as indicated in the figure. Compared to surfactant SDS-dispersed

HiPco SWNTs [23], an average of 30 meV red-shift in energy is observed in the semiconducting nanotube E_{11} region and this can be attributed to changes in the surrounding dielectric environment caused by $[BMIM]^+[PF_6]^-$.

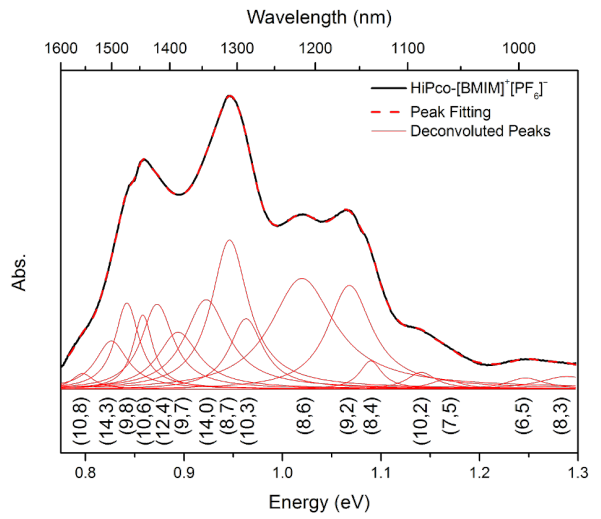

Figure 5: Deconvolution of the baseline-corrected absorption spectra of $[BMIM]^+[PF_6]^-$-dispersed SWNTs in the semiconducting nanotube E_{11} region with the solid black curve denoting the baseline-corrected spectrum, the dashed red curve denoting the fitting spectrum, and the solid red curves denoting the deconvoluted individual peaks corresponding to different chiralities of the semiconducting nanotubes.

A similar spectral-subtraction method was carried out with SWNTs dispersed in $[BMIM]^+[BF_4]^-$ and the resulting spectra are plotted in Figure 6. The agreement of the spectrum after subtraction of water with that of the water-free sample is also excellent, indicating the validity of this method for different types of ILs.

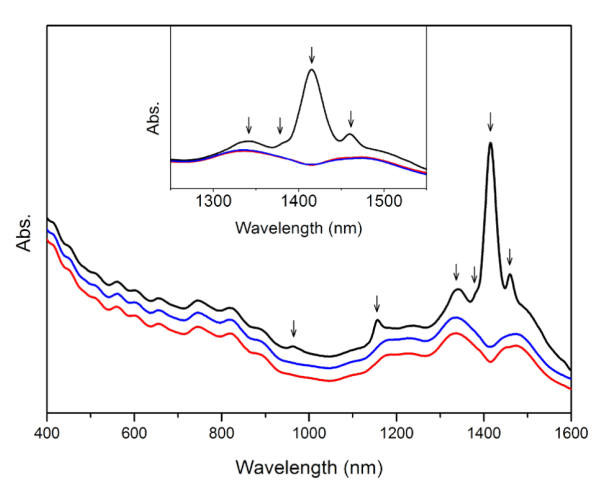

Figure 6: Absorption spectra of $[BMIM]^+[BF_4]^-$-dispersed SWNTs without treatment (black curve), after subtraction of water spectrum (blue curve), and treated under vacuum for 10 hours (red curve). The spectra are offset arbitrarily in the vertical direction for clarity. The inset shows the partially enlarged spectra. Arrows indicate the positions of water bands.

Conclusion

In this paper we have demonstrated a simple yet effective method for the spectral subtraction of the influence of trace water taken up by the ILs $[BMIM]^+[PF_6]^-$ and $[BMIM]^+[BF_4]^-$ on the absorption spectra of IL-dispersed SWNTs. The resulting spectra are in very good agreement with the spectra of water-free samples treated under high vacuum for 10 h. By utilizing this spectral-subtraction method, the additional step of sample treatment under vacuum can be avoid. The spectra after subtraction can be used directly for deconvolution and further quantitative analysis. This makes the characterization of SWNTs by analysis of absorption spectra more convenient in the IL-dispersion system.

Acknowledgement

The authors would like to thank NSF (Project 21005004), SRFDP of China, and MOST (Project 2011CB933003) of China for support.

References

1. Welton, T. *Chem. Rev.* **1999,** *99,* 2071–2084. doi:10.1021/cr980032t
2. Visser, A. E.; Swatloski, R. P.; Rogers, R. D. *Green Chem.* **2000,** *2,* 1–4. doi:10.1039/a908888a
3. Huddleston, J. G.; Rogers, R. D. *Chem. Commun.* **1998,** 1765–1766. doi:10.1039/a803999b
4. Compton, D. L.; Laszlo, J. A. *J. Electroanal. Chem.* **2002,** *520,* 71–78. doi:10.1016/S0022-0728(01)00747-1
5. Quinn, B. M.; Ding, Z.; Moulton, R.; Bard, A. J. *Langmuir* **2002,** *18,* 1734–1742. doi:10.1021/la011458x
6. Visser, A. E.; Swatloski, R. P.; Reichert, W. M.; Griffin, S. T.; Rogers, R. D. *Ind. Eng. Chem. Res.* **2000,** *39,* 3596–3604. doi:10.1021/ie000426m
7. Seddon, K. R. *J. Chem. Technol. Biotechnol.* **1997,** *68,* 351–356. doi:10.1002/(SICI)1097-4660(199704)68:4<351::AID-JCTB613>3.0.CO;2-4
8. Baker, S. N.; Baker, G. A.; Kane, M. A.; Bright, F. V. *J. Phys. Chem. B* **2001,** *105,* 9663–9668. doi:10.1021/jp0103528
9. Song, C. E.; Shim, W. H.; Roh, E. J.; Lee, S.; Choi, J. H. *Chem. Commun.* **2001,** 1122–1123. doi:10.1039/b101140p
10. Fukushima, T.; Kosaka, A.; Ishimura, Y.; Yamamoto, T.; Takigawa, T.; Ishii, N.; Aida, T. *Science* **2003,** *300,* 2072–2074. doi:10.1126/science.1082289
11. Islam, M. F.; Rojas, E.; Bergey, D. M.; Johnson, A. T.; Yodh, A. G. *Nano Lett.* **2003,** *3,* 269–273. doi:10.1021/nl025924u
12. Moore, V. C.; Strano, M. S.; Haroz, E. H.; Hauge, R. H.; Smalley, R. E.; Schmidt, J.; Talmon, Y. *Nano Lett.* **2003,** *3,* 1379–1382. doi:10.1021/nl034524j
13. Zheng, M.; Jagota, A.; Semke, E. D.; Diner, B. A.; McLean, R. S.; Lustig, S. R.; Richardson, R. E.; Tassi, N. G. *Nat. Mater.* **2003,** *2,* 338–342. doi:10.1038/nmat877

14. Zheng, M.; Jagota, A.; Strano, M. S.; Santos, A. P.; Barone, P.; Chou, S. G.; Diner, B. A.; Dresselhaus, M. S.; McLean, R. S.; Onoa, G. B.; Samsonidze, G. G.; Semke, E. D.; Usrey, M.; Walls, D. J. *Science* **2003,** *302,* 1545–1548. doi:10.1126/science.1091911
15. Star, A.; Stoddart, J. F.; Steuerman, D.; Diehl, M.; Boukai, A.; Wong, E. W.; Yang, X.; Chung, S.-W.; Choi, H.; Heath, J. R. *Angew. Chem., Int. Ed.* **2001,** *40,* 1721–1725. doi:10.1002/1521-3773(20010504)40:9<1721::AID-ANIE17210>3.0.CO;2-F
16. Bahr, J. L.; Yang, J.; Kosynkin, D. V.; Bronikowski, M. J.; Smalley, R. E.; Tour, J. M. *J. Am. Chem. Soc.* **2001,** *123,* 6536–6542. doi:10.1021/ja010462s
17. Holzinger, M.; Abraham, J.; Whelan, P.; Graupner, R.; Ley, L.; Hennrich, F.; Kappes, M.; Hirsch, A. *J. Am. Chem. Soc.* **2003,** *125,* 8566–8580. doi:10.1021/ja029931w
18. Wang, J.; Chu, H.; Li, Y. *ACS Nano* **2008,** *2,* 2540–2546. doi:10.1021/nn800510g
19. Kazarian, S. G.; Briscoe, B. J.; Welton, T. *Chem. Commun.* **2000,** *20,* 2047–2048. doi:10.1039/b005514j
20. Aki, S. N. V. K.; Brennecke, J. F.; Samanta, A. *Chem. Commun.* **2001,** 413–414. doi:10.1039/b008039j
21. Cammarata, L.; Kazarian, S. G.; Salter, P. A.; Welton, T. *Phys. Chem. Chem. Phys.* **2001,** *3,* 5192–5200. doi:10.1039/b106900d
22. Tran, C. D.; De Paoli Lacerda, S. H.; Oliveira, D. *Appl. Spectrosc.* **2003,** *57,* 152–157. doi:10.1366/000370203321535051
23. Strano, M. S.; Dyke, C. A.; Usrey, M. L.; Barone, P. W.; Allen, M. J.; Shan, H.; Kittrell, C.; Hauge, R. H.; Tour, J. M.; Smalley, R. E. *Science* **2003,** *301,* 1519–1522. doi:10.1126/science.1087691
24. Vinogradov, S. N.; Linnel, R. H. *Hydrogen Bonding;* Reinhold Publishing Group: New York, 1971.

License and Terms

Beilstein Journal of Nanotechnology

Nano-FTIR chemical mapping of minerals in biological materials

Sergiu Amarie[1], Paul Zaslansky[2], Yusuke Kajihara[1,3], Erika Griesshaber[4], Wolfgang W. Schmahl[4] and Fritz Keilmann[*1]

Full Research Paper

Open Access

Address:
[1]Max Planck Institute of Quantum Optics and Center for NanoScience, 85748 Garching, Germany, [2]Max Planck Institute of Colloids and Interfaces, Wissenschaftspark Golm, 14424 Potsdam, Germany, [3]Department of Basic Science, The University of Tokyo, Tokyo 153-8902, Japan and [4]GeoBio-Center at LMU and Department of Earth and Environmental Sciences, Ludwig-Maximilians-Universität, 80333 München, Germany

Email:
Fritz Keilmann[*] - fritz.keilmann@mpq.mpg.de

* Corresponding author

Keywords:
biomineralization; chemical mapping; infrared spectroscopy; nanocrystals; optical near-field microscopy

Beilstein J. Nanotechnol. **2012,** *3,* 312–323.
doi:10.3762/bjnano.3.35

Received: 30 December 2011
Accepted: 07 March 2012
Published: 05 April 2012

This article is part of the Thematic Series "Nanophotonics, nano-optics and nanospectroscopy".

Guest Editor: A. J. Meixner

Abstract

Methods for imaging of nanocomposites based on X-ray, electron, tunneling or force microscopy provide information about the shapes of nanoparticles; however, all of these methods fail on chemical recognition. Neither do they allow local identification of mineral type. We demonstrate that infrared near-field microscopy solves these requirements at 20 nm spatial resolution, highlighting, in its first application to natural nanostructures, the mineral particles in shell and bone. "Nano-FTIR" spectral images result from Fourier-transform infrared (FTIR) spectroscopy combined with scattering scanning near-field optical microscopy (s-SNOM). On polished sections of *Mytilus edulis* shells we observe a reproducible vibrational (phonon) resonance within all biocalcite microcrystals, and distinctly different spectra on bioaragonite. Surprisingly, we discover sparse, previously unknown, 20 nm thin nanoparticles with distinctly different spectra that are characteristic of crystalline phosphate. Multicomponent phosphate bands are observed on human tooth sections. These spectra vary characteristically near tubuli in dentin, proving a chemical or structural variation of the apatite nanocrystals. The infrared band strength correlates with the mineral density determined by electron microscopy. Since nano-FTIR sensitively responds to structural disorder it is well suited for the study of biomineral formation and aging. Generally, nano-FTIR is suitable for the analysis and identification of composite materials in any discipline, from testing during nanofabrication to even the clinical investigation of osteopathies.

Introduction

Fourier-transform infrared spectroscopy (FTIR) [1] is a standard tool in chemical analysis. It can identify virtually any substance through the "fingerprint" of the molecular vibrational absorption spectrum in the 3–30 µm wavelength region. Nano-FTIR spectroscopic near-field microscopy is a fascinating recent advance [2-4]. It enables scattering near-field optical microscopes (s-SNOM) [5,6] to operate at ultrahigh spatial resolution over a broad mid-infrared spectrum emitted from either a coherent supercontinuum source [2,3] or an incoherent thermal source [4]. The s-SNOM uses a metalized AFM tip as a light-concentrating antenna such that the sample is probed with a nanofocused light field (Figure 1). The nanofocus is a light spot of the same size as the tip radius, which thus defines both the optical and the topographic resolutions of s-SNOM. Detection of the backscattered light reveals local optical information. The probed volume extends typically 20 nm laterally, as well as into the sample (sometimes even less than 10 nm) [7]. The high resolution is independent of the wavelength. This enables the utilization of long wavelengths corresponding to the infrared fingerprint vibrations. s-SNOM has been successfully operated with visible, infrared and terahertz illumination, and has been applied to organic [8,9] and inorganic [10] materials, in such diverse fields as nanoelectronics [11], the physics of phase transitions [12], or material identification [13]. The underlying near-field interaction has been theoretically modeled and experimentally verified. The observable contrasts and spectra can be derived from the complex dielectric function of the sample material [6,14], and include both the absolute efficiency and the phase of the scattering [3]. Nano-FTIR has, up to now, been demonstrated with flat test samples only, consisting of metals, semiconductors and polar crystals [3,4].

Hard biological tissues are highly textured composites of submicrometric inorganic particles embedded in organic matrices [15-17]. Major tissues of interest include the phosphatic (bone) family of materials, and the carbonatic family as found, e.g., in mollusc shells. Within the phylum Brachiopoda, both strategies of hybrid shell architecture have evolved: Calcium carbonate crystals in an organic matrix [18-20], and laminates of calcium phosphate nanoparticle reinforced chitin fibers [21,22]. FTIR spectroscopic microscopy is a well-established method and has been extensively used to study bone biominerals at several micrometers spatial resolution [23-30]. Its strength in the study of bone biopsies, mineralized tendons, dentin or ivory is mainly due to a broad absorption band between 950 and 1150 cm^{-1} assigned to the ν_3 vibration of the PO_4^{3-} ion of apatite. It is thus possible to acquire maps of mineral concentration, and to relate mineral to protein (collagen) or carbonate distributions, usually revealing considerable spatial variation. Moreover, the apatite band exhibits a weak spectral substructure, evident from Fourier self-deconvolution [1]. It reveals relative weights of apatite species that are assigned, with the help of chemical and X-ray analyses, to Mg^{2+}, F^- or CO_3^{2-} substitution, or differing particle size, or crystal imperfections [24,31,32]. In this study we demonstrate the power of nano-FTIR to map naturally formed mineralized nanostructures. We show that we obtain fingerprint information on two example systems of biominerals. Experimental comparison is made with electron microscopy (SEM) to verify that nano-FTIR perfectly matches what is already known about the structures, and that the method indeed provides rich chemical and structural contrasts at the 20 nm scale.

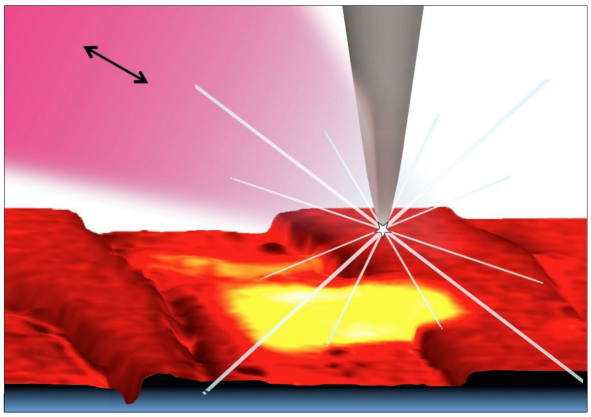

Figure 1: Nano-FTIR basic interaction. Focused infrared light incident from the upper left excites a nanofocus at the metal tip, symbolized as a star, which interacts with the scanning sample. The backscattered infrared light carries local information. Here, the infrared response (color code as in Figure 2b) is overlaid on a pseudo-3D rendering of the topography, which is simultaneously recorded, of a 1.4 × 1.6 μm^2 zoom area designated in Figure 2b by the dashed box on the left. Topographic height differences ca. 50 nm.

Results

Marine shell as an example of a carbonate-forming organism

We demonstrate nano-FTIR near-field microscopy on a *Mytilus edulis* (*M. edulis*) shell specimen, which exhibits easily resolvable fibrous biocalcite microcrystals and tablet-shaped bioaragonite nanocrystals. On a polished section, the expected characteristic interface [33] between an outer calcite layer and an inner aragonite layer is readily located with the help of an overview microscope (0.7 µm resolution) built into the commercial s-SNOM used (neaspec.com). On the inner side there is an interlayer, ca. 2 µm wide, with modified bioaragonite crystals [34]. Three adjoining s-SNOM images of 10 × 10 μm^2 area each were consecutively acquired and stitched together. The topography (Figure 2a) exhibits the arrangement of (i) fiber-

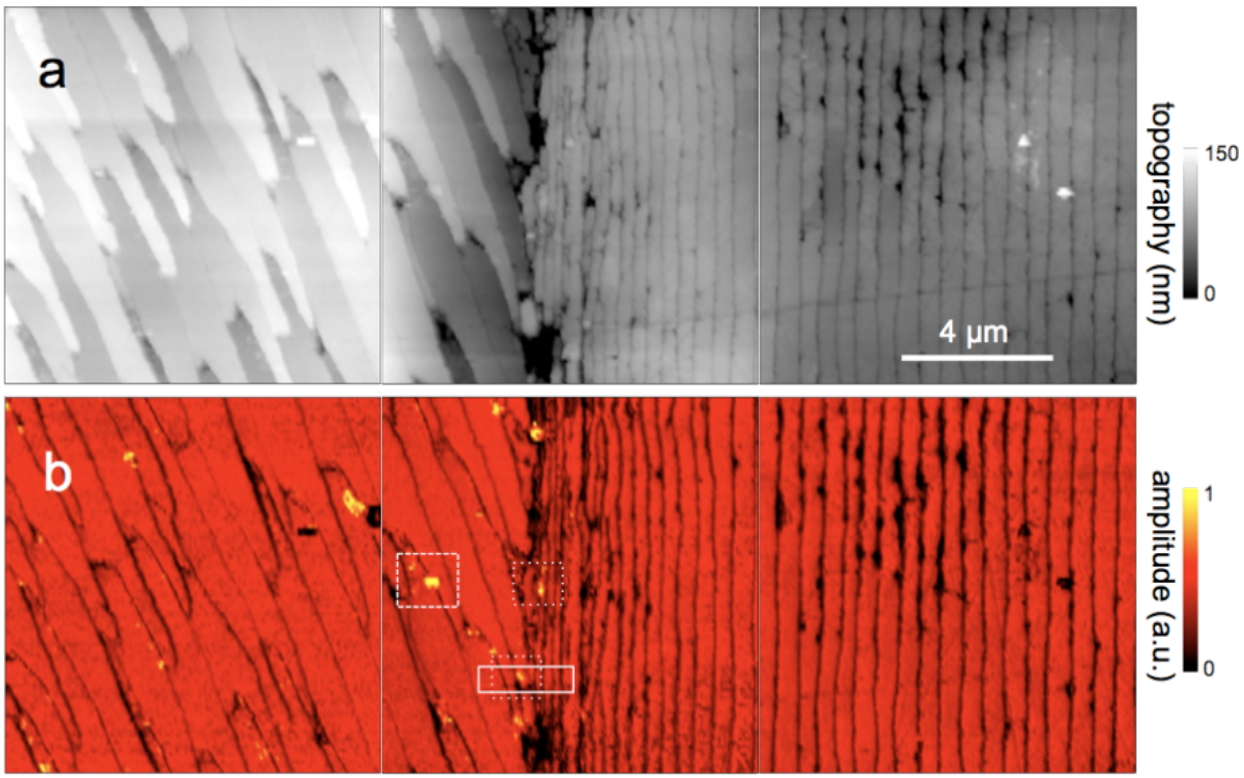

Figure 2: Polished section of *Mytilus edulis* viewed in monochromatic s-SNOM (980 cm^{-1}). (a) Topography of the interface between two calcium carbonate polymorphs, biocalcite crystals (left) and bioaragonite crystals (right); (b) the backscattered infrared amplitude (n = 3) contrasts the organic matrix at a relatively low level; a few, unexpected particles highlighted by their enhanced amplitude are chemically different; we refer to them as "phosphate" crystals because their spectra (Figure 3 and Figure 4) are characteristic of phosphate.

shaped biocalcite crystals with slightly oblique, flat surfaces at a few distinctly different heights, (ii) deep depressions mainly in the interlayer, and (iii) bioaragonite crystals with flat surfaces at equal height, some (in the interlayer) as narrow as 100 nm.

For chemical mapping we collected 300 nano-FTIR spectra along a 2.5 µm line marked in Figure 3a, across the interface region designated by a full white rectangle in Figure 2b (Figure 3, additional scans are shown in Figure 5). The spectra in Figure 3b and Figure 3c (and also the extracted averaged spectral profiles in Figure 4) are dominated by a single, sharp resonance, which differs in frequency position for orthorhombic aragonite (855 cm^{-1}) and trigonal calcite (873 cm^{-1}), and thus both calcium carbonate polymorphs can be readily distinguished. The biocalcite spectra show no spectral shift within a given crystal, either upon comparison of neighboring crystals of the same type, or with changes in topographic height as seen with the three leftmost (biocalcite) crystals in Figure 3. Intriguingly, we notice on close inspection of all biocarbonate surfaces, e.g., in Figure 1, a shallow amplitude modulation on a 50–200 nm lateral scale, which we tentatively explain to be due to a mesocrystalline substructure that has been recently observed by SEM [35].

In Figure 3 and Figure 5 the infrared resonance is not as repeatable on the bioaragonite as on the biocalcite crystals, both with regard to spectral position and height. Further away from the interface layer bioaragonite has a more stable spectrum (not shown). This indicates that the interlayer carbonate (i) is truely bioaragonite but (ii) has a reduced, changeable mineral content. The interlayer bioaragonite crystals are clearly smaller and less well ordered (Figure 2).

Surprisingly, we find in Figure 3 a 350 nm long section with a similarly strong and sharp resonance at a much higher frequency of about 1018 cm^{-1}, which we tentatively assign to be phosphate (see Discussion section). In order to specifically map its occurrence we acquired monochromatic s-SNOM images (Figure 2 and Figure 6) at 980 cm^{-1}, which is a CO_2 laser frequency at which the scattering signal is still weakly enhanced by the "phosphate" resonance (see amplitude spectra in Figure 3b, Figure 4 and Figure 5b). "Phosphate" occurs at a few spots only, in the calcite region up to and including the interlayer, but not further out in the aragonite region; in the calcite region its occurrence diminishes with distance from the interface (Figure 6). Additional zoomed images such as Figure 1 (see also Figure 11) unveil individual "phosphate"

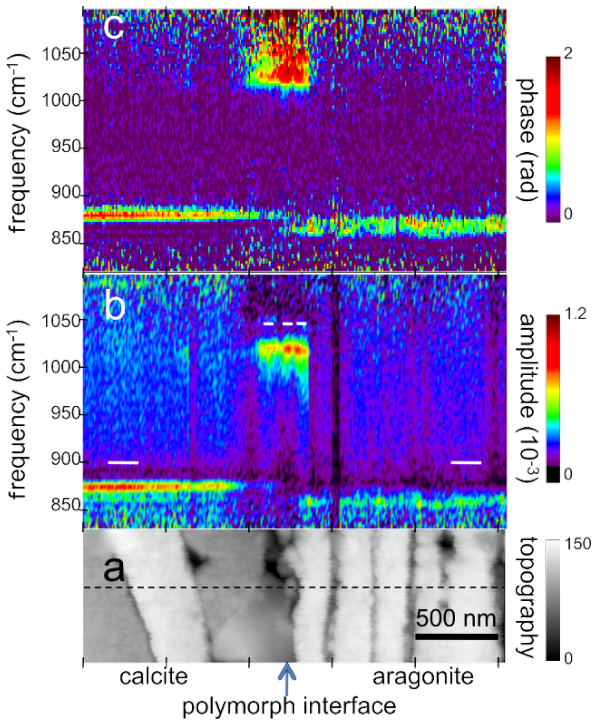

Figure 3: Nano-FTIR spectral line scan across the interface between calcite and aragonite layers; (a) Topography corresponding to the full white box of Figure 2b, with the scan line marked by a dashed line; (b) infrared amplitude and (c) infrared phase spectra identify calcite, "phosphate" and aragonite by their resonances at 872, 1018, and 857 cm^{-1}, respectively. The white bars define the ranges of averaging for the spectra for Figure 4.

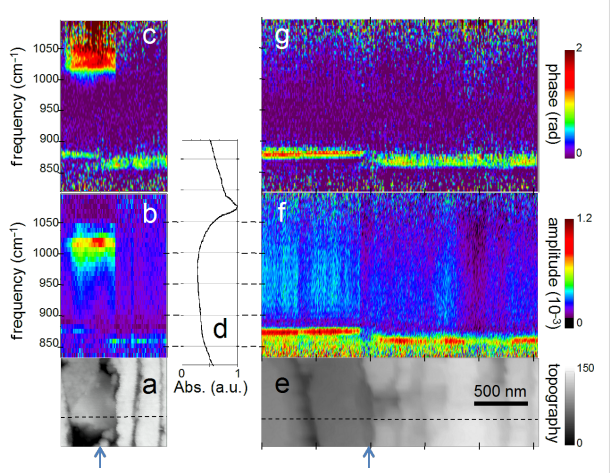

Figure 5: Nano-FTIR spectral line scans as in Figure 3; (a–c) Topography, amplitude and phase spectra ca. 300 nm below the scan in Figure 3; (e–g) the same but further away; (d) infrared absorption of dry polished material, with frequency scale aligned to (b and f).

regions as sparsely scattered, contiguous particles of 100 to 500 nm size that seem to be no higher than 10 or 20 nm judging from their topography. All "phosphate" particles are distinguishable in the topography images. In passing we note that there are numerous other nanoparticles with a topographic height of up to 100 nm (Figure 2 and Figure 6); these exhibit a small infrared amplitude pointing to a nonresonant organic material [6]. The "phosphate" particles in Figure 3 and Figure 5a–c happen to bridge the interface as they exhibit in their left part a reduced calcite resonance (best recognizable in the phase spectra), and in their right part also a reduced aragonite resonance. This superposition of spectra suggests that the "phosphate" particles are thin enough, about 20 nm, for sensing also of the underlying calcite or aragonite (see Discussion section) [36].

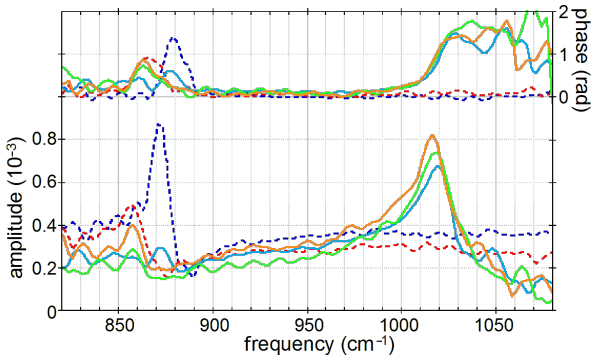

Figure 4: Nano-FTIR spectra of *M. edulis* obtained from Figure 3b and Figure 3c by averaging over the ranges indicated in Figure 3b by the white bars: calcite region (blue, dashed), aragonite region (red, dashed), "phosphate"/interface region (full, from left to right: yellow, green, blue).

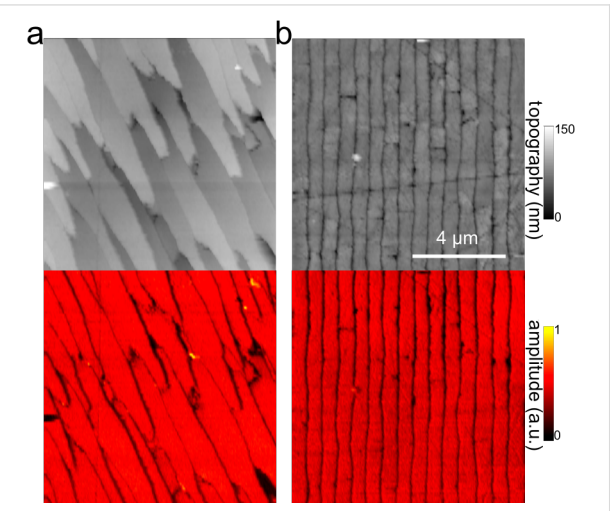

Figure 6: Polished section of *Mytilus edulis* viewed in monochromatic s-SNOM (980 cm^{-1}), continued from Figure 2; (a) 120 µm further left in the calcite region and (b) 120 µm further right in the aragonite region.

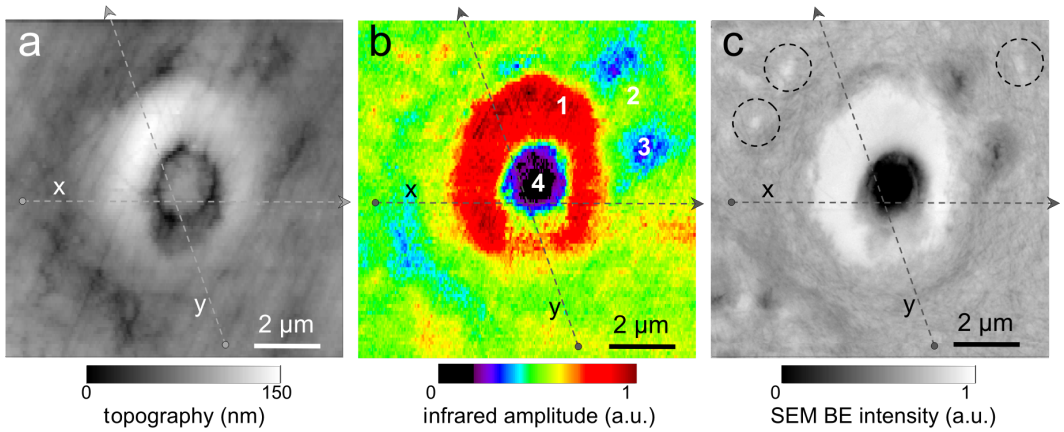

Figure 7: Tubule in human dentin and its surrounding imaged by (a,b) nano-FTIR where the topography (a) is acquired simultaneously with the infrared amplitude image (b, in spectrally integrating mode), and by (c) SEM (backscattered electron image (BEI)).

Human dentin

The exciting potential of nano-FTIR imaging of phosphate-based biominerals is demonstrated with a human tooth in which the bone-like phosphate nanocrystals are too small to be resolved, but where a hierarchy of structures exists at all scales including the submicrometer range [16,37]. Here, we explore dentine, a mineralized collagen-fibril-based [37] biological composite that supports enamel and is similar to bone, but does not remodel and does not contain cells. Dentin contains extensions of the pulp cells, which reside in ca. 1 µm thick tubules that are often surrounded by 1 to 2 µm thick mineralized sheaths devoid of collagen. Tubules of teeth are known to branch into nano-tubuli [38] and are easily observed on perpendicularly cut sections. Figure 7 shows a 10 × 10 µm^2 area surrounding a typical tubule (filled with PMMA, see methods) inside the tooth, approximately 1.5 mm away from the enamel/dentin junction. The infrared image in Figure 7b was obtained in a spectrally integrating mode that highlights the phosphate band from approx. 950 to 1150 cm^{-1} (see Experimental section). A general similarity is seen with the SEM backscattered electron (BE) image (Figure 7c), in which the intensity is known to be a measure of the mineral density, averaged over ca. 1 µm depth [39]. The high-density peritubular rims produce the strongest infrared scattering. As a consequence of their higher resistance to polishing, they protrude approximately 50 nm from the surrounding dentin matrix. Outside the peritubular ring, the upper-right quadrant of the BE image exhibits two low-density spots with about 100 nm diameter designating nanotubuli. They appear clearly in the infrared images as spots of about 1 µm in diameter with an amplitude between the low one of PMMA (inside the large tubule) and that of intertubular dentin. Several high-density patches revealed by BEI (e.g., encircled in Figure 7c) are clearly expressed in the infrared image by a slightly enhanced amplitude. Thus spectrally integrated (phosphate band) nano-FTIR images of dentin compare well with the BE image of the same tissue.

The unique spectroscopic information provided by nano-FTIR is substantiated by four spectra centered on the phosphate ν_3 vibrational band (Figure 8), acquired at characteristic locations marked in Figure 7b, and a fifth on the same tooth section taken 2 mm away on the enamel. The enamel and dentin amplitude (and phase) spectra are dominated by the resonance at 1025 cm^{-1}. The peak height varies with location similarly as the spectrally integrated infrared amplitude as imaged in Figure 7b. While being assigned to phosphate as in the *M. edulis* case, we find that the tooth phosphate resonance is significantly broadened. Apparently this is an inhomogeneous broadening akin to what is known from classical FTIR spectra of bone [23-32].

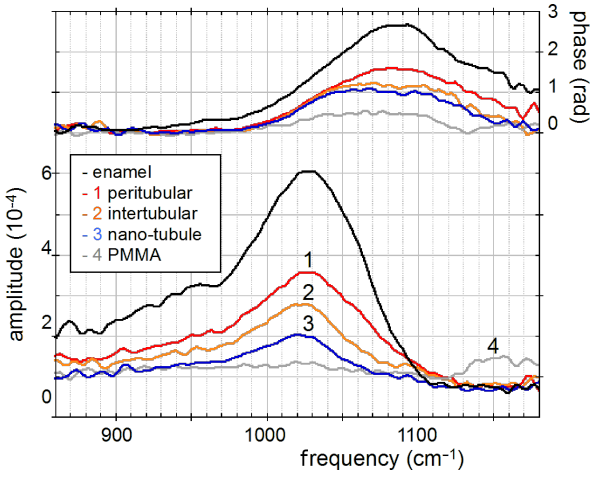

Figure 8: Local infrared spectra registered by nano-FTIR at positions 1–4 in Figure 7b (colors), and further away on enamel of the same tooth section (black).

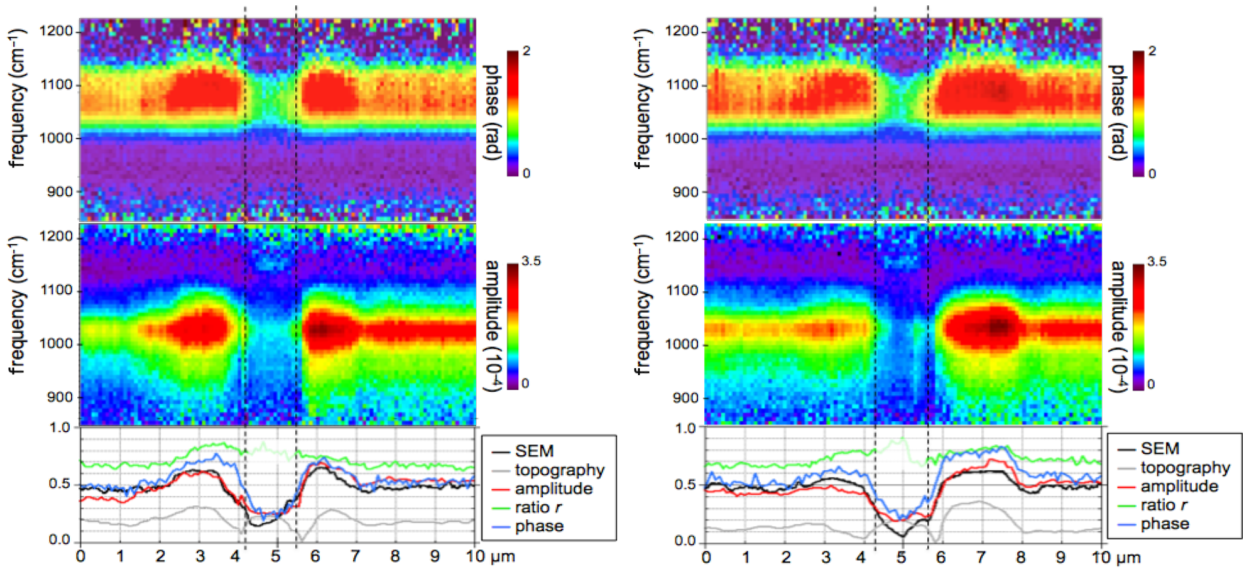

Figure 9: Dentin characteristics along line scans marked x (left part) and y (right part) in Figure 7; SEM intensity (black), topography (grey, in nm scaled by 1/240), nano-FTIR spectra (upper two panels), and three therefrom extracted quantities: amplitude at 1020 cm^{-1} (red, scaled ×2500), ratio *r* of amplitudes at 1053 and 1022 cm^{-1} (green), and phase at 1080 cm^{-1} (blue, in rad scaled by 1/2).

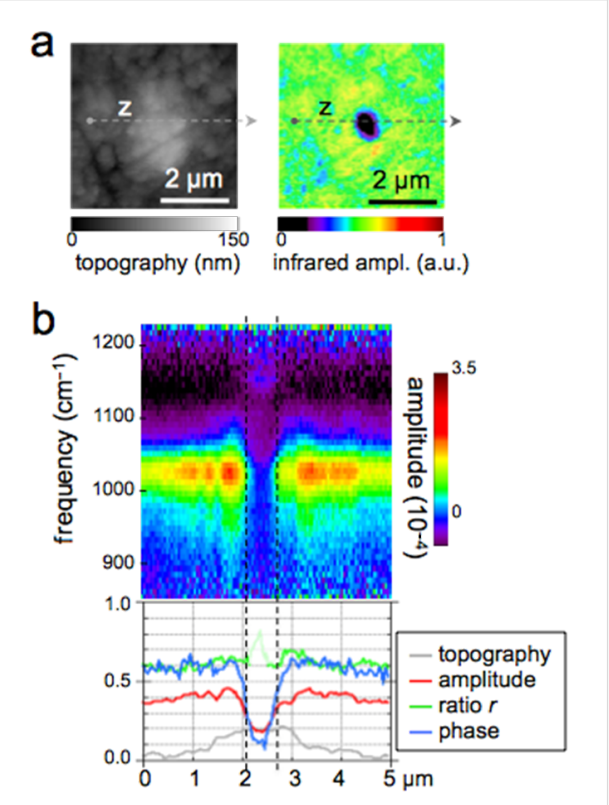

Figure 10: Tubule in human dentin near the enamel, imaged by nano-FTIR in which the infrared amplitude image (a, right, in spectrally integrating mode) is acquired simultaneously with the topography (a, left); (b) dentin characteristics along line scan marked z in (a), topography (grey, in nm scaled by 1/240), infrared amplitude spectrum (upper panel), and extracted quantities as in Figure 9.

Interestingly, the processed spectra show that the band shapes are significantly different for each of the five locations (see Discussion section, Figure 12a). The PMMA amplitude spectrum shows a relatively weak resonance around 1160 cm^{-1}.

The nano-FTIR spectra (Figure 9) recorded along 110 pixels of 10 µm long trajectories (marked in Figure 7) demonstrate the excellent reproducibility of the method. Local spectral variations clearly mark the dentin microstructure. Though weak, the spectrum of PMMA allow us to define the approximate tubule opening, designated by two dashed lines in Figure 9 and Figure 10. The lower panels of these figures show three interesting quantities extracted from the nano-FTIR spectral scans (colored curves, see Discussion section), together with the simultaneously recorded profiles of SEM intensity (black curve) and of topography (grey curve). A second tubule adjacent to the enamel junction displays a considerably narrower lumen and little topographic height, but clear infrared signatures (Figure 10).

Discussion

FTIR is well established as a method for studying biominerals in a variety of settings, and nano-FTIR extends this functionality to include spectroscopic mapping at the nanometer length scale. Our observations of phosphates and carbonates in the well-studied examples of *M. edulis* and human dentin reveal exquisite detail, which matches what is observed by electron microscopy and nanoindentation. The achievement of chemical and structural mapping of biominerals opens new horizons for

our understanding of mineral arrangements and variability in biological systems. Intricate carbonate-based natural skeletons, that may include transient and stabilized amorphous phases, can now be mapped within and across interfaces by a noncontact and nondestructive imaging technique. With respect to apatite studies, our method is directly applicable to the investigation of healthy and diseased forms of vertebrate bones and teeth. Mineral precipitation, aggregation and aging can now be analyzed and quantified in submicrometer detail, to better understand the biological processes of bone formation, abnormal development, and healing in response to drug treatment.

Several technical advantages of surface scanning make the nano-FTIR approach extremely robust and useful for the study of biological materials. The samples need not be thin, only reasonably flat, thus avoiding thin-section preparations, which are prone to damage. Unavoidable topographic obstacles resulting from the cutting and polishing procedures are of little consequence: Height variations of 100 nm do not change the off-resonant infrared amplitude (Figure 2) nor the resonant response in amplitude and phase, as demonstrated for example by the repeatability of the carbonate resonance spectra within the sample region containing biocalcite (Figure 3). At steep topographic edges though, the s-SNOM amplitude is known to be reduced over a width equal to the spatial resolution, resulting in "edge darkening" [6]. This effect probably contributes to the dark regions seen between calcite crystals in Figure 2b and remains to be further investigated. The impressive spatial resolution of nano-FTIR can be judged from the edges of the biocalcite crystals (Figure 3a) that demonstrate a mechanical (AFM) resolution certainly below 30 nm. Abrupt edges of the nano-FTIR line section showing the phosphate resonance (Figure 3b,c and Figure 5b,c) prove that the infrared resolution is better than 20 nm.

The "phosphate" particles in *M. edulis* are clearly recognized from their spectral signature (Figures 3–5), but would have been barely detected based on their topographic appearance alone (interestingly, their surfaces (see also Figure 1 and Figure 11) appear smoother than the neighboring biocarbonate crystals). Note that the nano-FTIR spectra of the "phosphate" particles additionally show one of the carbonate resonances (Figures 3–5), obviously originating from the crystals underneath [36,40]. To understand this effect, we recall that the basic near-field interaction probes the sample to a depth on the order of the tip radius (or somewhat deeper when one chooses the tapping amplitude or the average tip-to-sample distance to be larger than the tip radius) [6]. Thus buried objects may affect the backscattering provided that the covering layer is not thicker than a few times the tip radius [36]. Based on this effect, even a tomographic mapping capability of s-SNOM has been suggested [6,41]. Our present observation is the first report to distinguish different phonon resonances in both the covering layer and the buried material. We estimate from the observed amplitudes that the thickness of the "phosphate" particles is on the order of 10–30 nm, in agreement with their topographic appearance.

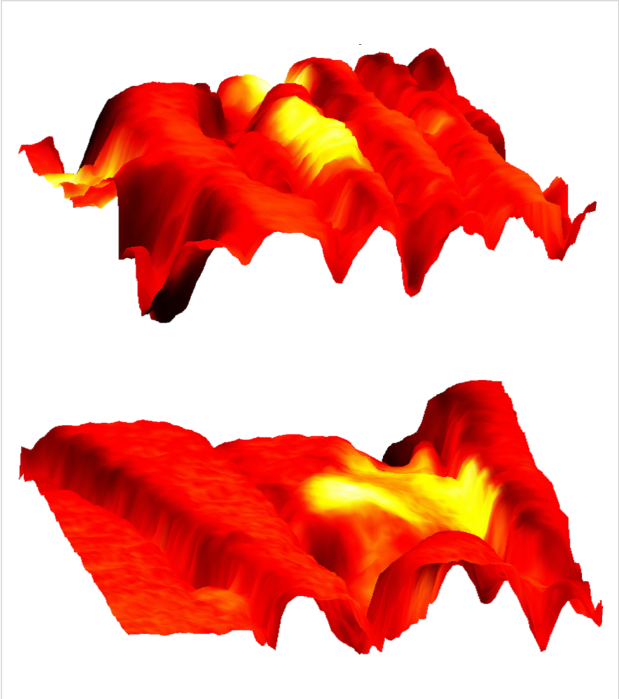

Figure 11: "Phosphate" in *M. edulis*. High-resolution images (similar to Figure 1) of the dotted-box areas, 1.0 × 1.2 μm^2 of Figure 2. Backscattered infrared amplitude in color code as in Figure 2b, overlaid on a pseudo-3D rendering of the topography.

The origin of the "phosphate" particles remains unclear in this proof-of-principle study. Their erratic distribution may suggest some unknown preparation artifact. The material could be a modification of materials in the organic matrix; however, this is not highlighted in the infrared images. Nevertheless, it is clear that the particles could not simply be dried polishing material (Struers OP-A) since this shows a weak FTIR absorption at 1073 cm^{-1} (Figure 5d) but no discernible nano-FTIR resonance in the frequency range of interest. A strong argument for the assignment of the particles as crystalline phosphate is the observed high spectral phase effect of about 80°, exceeding that of bioaragonite (50°) and biocalcite (70°). Typically the spectral phase effect is on the order of 30° for strong polymer vibrations [8,9] but on the order of 400° for strong crystal phonons [3,6]. For molluscs the employment of phosphate in shell architecture has not been reported, but the radula (tooth structure) of the chitons is known to contain calcium phosphate [42,43]. In bones, phosphorylated proteins have been suggested as impor-

tant components of the organic matrix [44,45]. Notwithstanding their unclear origin, our finding of "phosphate" particles demonstrates that nano-FTIR can easily locate and chemically recognize nanometer-sized material even at high rarefaction. We finally note that the observed particles are crystalline for two more reasons: (i) Their near-field scattering amplitude is about 10^{-3} as with calcite (Figure 3b and Figure 4), and not much smaller than 3×10^{-3} as known for two strongly polar crystals, SiC and SiO_2 [3]; and (ii) their near-field resonance line shape is asymmetric, with the steep high-frequency edge (Figure 4) typical of strong oscillators [6,46]. Disorder in a crystal would strongly reduce the amplitude, as has been shown systematically [47]. Amorphous materials have a reduced, broadened resonance [3], while typical organic materials are known to have an even weaker response [8], as is also seen in this study with the PMMA resonance peaking at 1.5×10^{-4} near 1150 cm^{-1} (grey curve in Figure 8).

The broad phosphate bands measured in dentin by nano-FTIR contain information on the biomineral composition and density. Firstly, from their peak and baseline amplitudes (Figure 8) we tentatively determine the local volume fraction f of mineral particles (assuming $f = 1$ for enamel) to amount to $f = 0.54$, 0.30, and 0.26, respectively, for the spectra 1, 2, and 3 (see Experimental section). Then, following normalization, we obtain the line shapes of the mineral fraction at each of the three locations, plotted in Figure 12a (in the same colors as in Figure 8). Clearly there are significant, position-dependent differences in the 1020 to 1120 cm^{-1} frequency range. These differences show that (i) tooth materials consist, even on a 20 nm length scale, of several mineral types differing in their vibrational resonances, and (ii) the mineral composition varies with location. Specific spectral components may be identified at 1020, 1055, and 1100 cm^{-1}. The component at 1055 cm^{-1} is present in enamel and peritubular dentin but not in intertubular dentin, and may relate to the lack of collagen protein, whereas the component at 1100 cm^{-1} is present in all dentin but not in enamel. For discussing possible assignments we have calculated and plotted the distribution of three characteristic quantities, which we extract from the nano-FTIR spectral scans, namely the peak s-SNOM amplitude (red), the ratio r of amplitudes at 1053 cm^{-1} and 1022 cm^{-1} (green; not meaningful in the tubule lumen), and the phase at 1080 cm^{-1} (blue), in a direct comparison with the BEI profiles (Figure 9 and Figure 10).

In the BE image with 0.12 nm resolution (Figure 7c), the brightness provides a local measure of the electron density [48] and consequently of the mineral content [39]. While the white hypermineralized rim of the tubule exhibits an identical shape to that seen in the infrared (Figure 7b), the fine linear fibrils in the BEI are not seen in the infrared images presumably because

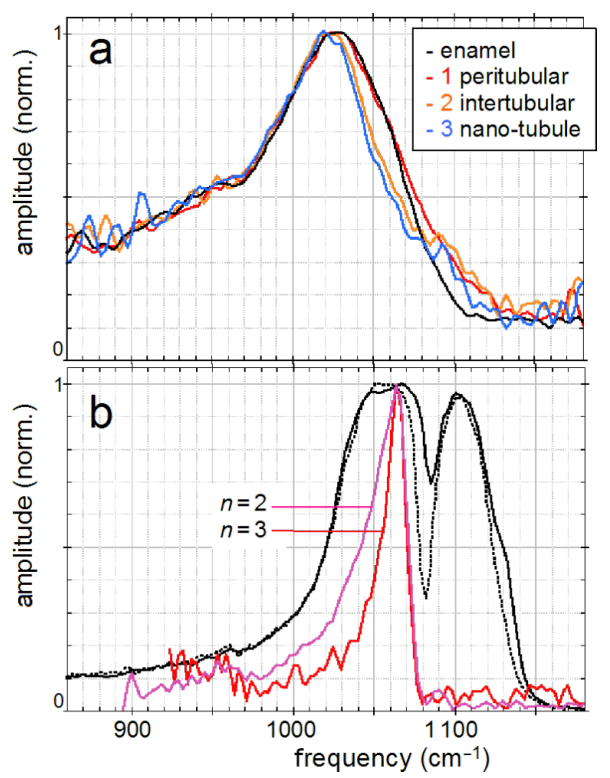

Figure 12: Normalized infrared resonance of phosphate; (a) of dentin and enamel measured by nano-FTIR (colors as in Figure 8); (b) of fluorapatite crystal at 10 nm tapping amplitude by nano-FTIR (magenta), and measured simultaneously at $n = 3$ demodulation (red, see Experimental section), and by conventional FTIR reflectance (black); the latter also for hydroxyapatite (black, dotted).

they are too deep below the surface. We note in passing that s-SNOM is nondestructive, unlike SEM in which the interaction of electrons with bony materials is known to induce damage. The extracted BE profiles (Figure 9) mark the edges of the tubule lumen, as do the extracted infrared profiles. Outside the peritubular rim, the amplitude (red) and phase (blue) correlate qualitatively with the BE-defined mineral content (black). An exception in the 7.1–7.5 µm section of Figure 9 (right) is attributed to the different probing depths of the s-SNOM and BE imaging methods. Amplitude and phase thus appear to be equally capable of measuring small density changes. As for the spectral differences within the phosphate band, the ratio r is about 0.8 and 0.7 for the peritubular and intertubular regions of the large tubule (x,y), respectively, but interestingly only 0.7 and 0.6, respectively, for the small tubule (z, Figure 10). For enamel $r = 0.80$ (Figure 12a).

An assignment of the observed nano-FTIR spectral components of tooth at around 1020, 1055, and 1100 cm^{-1} is, unfortunately, not straightforward, because most apatite species of interest have not yet been measured by s-SNOM as pure substances. For bulk crystals, it is well known from theory and experiments that

the near-field resonance in the case of a strong oscillator is up-shifted from the transverse phonon frequency that marks the infrared absorption [6]. The up-shift nearly to the longitudinal phonon frequency amounts to 62 cm^{-1} for SiO_2 [3], and even to 120 cm^{-1} for the exceptionally strong phonon of SiC [46]. For fluorapatite, infrared-active modes are known to be at 1030 cm^{-1} (strong), 1042.5 cm^{-1} (weak), and 1091 cm^{-1} (medium) [49], while nano-FTIR registers a strong resonance at 1063 cm^{-1} (as also in hydroxyapatite) and a weak one at 1090 cm^{-1}, as shown in Figure 12b (for comparison we also show reflectivity spectra that nearly match for both apatites). The strong near-field resonance obviously comes from the strong infrared-active mode at 1030 cm^{-1}, and thus is up-shifted by 33 cm^{-1}. Naively one would expect that the near-field components observed at 1020, 1055, and 1100 cm^{-1} in tooth materials connect to correspondingly lower-frequency, strong infrared absorption components. But this seems not to be the case, because the experimental FTIR absorption of dentin exhibits peaks at 1039, 1069, 1108 [30], or 1040, 1060, 1092 cm^{-1} [28]. A down-shift of the 1040 line to 1014 cm^{-1} was reported for caries-affected dentin [26]. Theoretically it has not been explored for the case of small particles as to whether, and in which direction, the near-field resonance should shift from a given far-field absorption peak. Our experiments show that the near-field resonance in enamel and dentin exhibits a peak near 1020 cm^{-1}, which is 43 cm^{-1} below the near-field resonance of apatite (Figure 12).

Generally, the interpretation of infrared absorption observed in bone should be extended to include the influence of the particles' shape through depolarization effects [50,51]. Recently, density functional theory has been applied specifically to the apatite ν_3 vibrational infrared absorption, predicting strong spectral distortion and splitting (up to ±50 cm^{-1}) due to these macroscopic electrostatic effects (not to be confused with microscopic distortion of lattice cells), depending on whether the particles are spherical, needle-like or plate-like [52]. Powder measurements with classical FTIR displayed absorption peaks at 1038, 1067, 1097 cm^{-1} for fluorapatite, and at 1034, 1053, 1105 cm^{-1} for hydroxyapatite, where indeed the last two peaks were found to be strongly split by the nonspherical shape of the particles [52]. Similar values were reported in other studies [24,53,54]. As the mineral in dentin and bone consists of isolated, locally ordered apatite platelets, strong depolarization effects probably distort the infrared spectra in the ν_3 phosphate resonance region. Clearly a systematic study is warranted in which near-field and far-field infrared apatite bands are acquired for various shapes of chemically and structurally well-defined nanocrystals. Such a study should also cover the weaker ν_1 phosphate band, which is less affected by electrostatic effects, as are all Raman lines [52].

Figure 12b directly illustrates the spectral discrimination provided by nano-FTIR [46], which has great potential for mineral research. The measured near-field response is seen to drop within 7 cm^{-1} (between 90% and 10% of the peak amplitude); the response is even sharper because our present instrumental resolution is about 6 cm^{-1} [3]. Additionally, Figure 12b shows that the resonance becomes narrowed simply by choosing a higher order n of signal demodulation (see Experimental section) [6]. This would result in a virtual "tip sharpening" and improve the spatial resolution of the s-SNOM [6,55,56]. As for the spectral resolution, a discrimination of components differing by just a few cm^{-1} is certainly achievable.

Experimental

s-SNOM near-field microscope

We employed a commercial scattering near-field microscope based on AFM (NeaSNOM, neaspec.com) equipped with a standard metalized tip (NCPt arrow, nanoandmore.com). It is operated in AFM tapping mode to modulate the near-field interaction between the tip and sample, and records the backscattered infrared signal simultaneously with the topography. Typical tapping amplitudes are 50–60 nm. Lock-in detection at the $n = 2$ harmonic (default) of the tapping frequency (approx. 300 kHz) provides background-free near-field imaging. Monitoring of the infrared signal versus tip–sample separation (approach curves) was used to ensure the optimal working settings of the tapping amplitude, the demodulation order n, and the focusing. In the monochromatic infrared near-field imaging mode of the s-SNOM a line-tunable CO_2 laser attenuated to 10 mW is used for illumination. The acquisition time was 5 ms per pixel, requiring several minutes for a 128 × 128 sized image.

Nano-FTIR mode of s-SNOM

The nano-FTIR spectroscopic mode of s-SNOM uses illumination by a coherent broadband mid-infrared beam (here 25 μW) from a difference-frequency source [3] driven by a femtosecond (<100 fs) Er fiber laser (FFS.SYS-2B and FFS-CONT, toptica.com). Detection and spectral analysis of the backscattered light is by an asymmetric Michelson interferometer that generates, by online Fourier transformation, infrared amplitude and phase spectra simultaneously; a switchable reference path ensures an absolute quantification of backscattering [3]. Note that while common FTIR spectrometers are not equipped to determine the complete, complex material response, the nano-FTIR phase spectra valuably complement the amplitude spectra [6]. For example, the phase change on resonance can be taken as a measure of the resonance strength. Nano-FTIR spectra can be monitored in real time at 3 Hz rate allowing the optimal focus adjustment on the tip. The usual acquisition time was 10 s

per pixel for obtaining highly resolved spectra as in Figure 3, Figure 5 and Figure 8. The spectroscopic line scans in Figure 9 and Figure 10b were obtained with a reduced spectral resolution of about 8 cm^{-1}, and the shown result is an average over five consecutive scans.

Figure 12b illustrates that the use of the $n = 3$ instead of the $n = 2$ demodulation order reduces the apatite resonance halfwidth by 40%. However, this is paid for by a five-fold reduction of the amplitude, as noted with other crystals previously [3]. Higher power than the presently available 25 μW would certainly allow for routine use of $n = 3$ and higher. Up to 10 mW is desirable (at which point tip heating starts to reduce the AFM stability) and would thus increase the present signal levels by 400×, or alternatively, reduce the acquisition time by 160,000× for a constant S/N ratio. Note that this positive perspective is in sharp contrast to tip-enhanced Raman scattering (TERS) for which up to 10 mW is readily available, but intrinsically weak cross sections leave little room for future signal improvement [57].

A spectrally integrated mode of nano-FTIR is also introduced in this study. It employs a fixed interferometer setting at a (free-induction-decay) [2] fringe maximum (ca. 150–300 fs delay). The detector amplitude signal then represents the background-suppressed near-field signal response averaged over a wide spectral band around the peak of the backscattered spectrum. Again the routine scanning is at a rate of 5 ms per pixel, requiring several minutes for a 128 × 128 pixel image.

Sample preparation

The shell valve of *M. edulis* was sectioned longitudinally into 200 μm thick wafers. These were polished on both sides and etched for 45 s with a suspension of alumina nanoparticles (Struers OP-A), then cleaned and dried. Tooth samples were embedded in PMMA following dehydration by a graded ethanol and PMMA exchange solution; samples were cut perpendicularly to the tubules, serially ground and polished by using diamond slurry down to 1 μm [58].

Line-shape determination of mineral component in a composite

A theory of near-field interaction for the dentin and bone cases of mixed particles that are smaller than the tip radius is not yet available. A straightforward solution would be to calculate an effective dielectric function, by using composite-medium theory [59], as a weighted average of the dielectric functions of the individual components (and taking proper account of depolarization), and then to apply the point-dipole or, better, the finite-dipole model of near-field interaction [3]. While composite-medium theory traditionally assumes spherical particles, an extension to ellipsoids is available [60]. Since individual dielectric functions are not known, however, we attempt here, for the first time in near-field microscopy, a simplified two-component analysis to extract the spectral contribution due to minerals. First, we determine the volume fraction f of mineral nanoparticles by extracting f from the spectra in Figure 8 in the following way. We assume the total scattering amplitude s to be a weighted sum of a mineral and an organic part, s^M and s^O, respectively, $s = f\,s^M + (1 - f)\,s^O$. We assume $f = 1$ for enamel, which consists nearly entirely of hydroxyapatite nanocrystals. For simplicity we assume a flat spectrum s^O. By setting $s^O = 0.00006$ we then determine $f = 0.54$, 0.30, and 0.26 for the spectra 1, 2, and 3, respectively. With these values we compute the mineral component normalized amplitude spectra, $s^M = (1 - (1 - f)\,s^O/s)/f$ shown in Figure 12a. Other settings of s^O would give less agreement of the spectra outside the phosphate band.

Conclusion

We have quite generally demonstrated the achievement of chemical identification—a central need for nanoscience—by an infrared nanoscope, at 20 nm resolution. We show both the highlighting of a selected compound in a scanned image, as well the measurement of local FTIR spectra. Our method is nondestructive and needs no vacuum or special sample preparation. Nano-FTIR is widely valuable for studying promising nanostructures, be it in nanotechnology, the pharmaceutical industry, or solid-state physics. For this study we have chosen biominerals over other obvious candidates because biomineralization is unexplored in its nanometer-scale detail but is yet of great medical importance.

Author contributions

F. K. conceived this study, P. Z., W. W. S. and E. G. identified and characterized the biomineral samples. F. K. and S. A. designed the SNOM experiments and analyzed the results. S. A., P. Z. and Y. K. performed the experiments. F. K. wrote the draft, and all authors contributed to the manuscript.

Acknowledgements

The authors are indebted to P. Fratzl for his long-term interest and support of this study. They acknowledge discussions with P. Hansma, U. Schade and A. Röseler. Supported by Deutsche Forschungsgemeinschaft through the Cluster of Excellence Munich Centre for Advanced Photonics.

References

1. Griffiths, P. R.; de Haseth, J. A. *Fourier Transform Infrared Spectroscopy;* Wiley: New York, 2007. doi:10.1002/047010631X
2. Amarie, S.; Ganz, T.; Keilmann, F. *Opt. Express* **2009,** *17,* 21794. doi:10.1364/OE.17.021794

3. Amarie, S.; Keilmann, F. *Phys. Rev. B* **2011,** *83,* 45404. doi:10.1103/PhysRevB.83.045404
4. Huth, F.; Schnell, M.; Wittborn, J.; Ocelic, N.; Hillenbrand, R. *Nat. Mater.* **2011,** *10,* 352. doi:10.1038/nmat3006
5. Knoll, B.; Keilmann, F. *Nature* **1999,** *399,* 134. doi:10.1038/20154
6. Keilmann, F.; Hillenbrand, R. In *Nano-Optics and Near-Field Optical Microscopy;* Richards, D.; Zayats, A., Eds.; Artech House: Boston, London, 2009.
7. Cvitkovic, A.; Ocelic, N.; Hillenbrand, R. *Nano Lett.* **2007,** *7,* 3177. doi:10.1021/nl071775+
8. Taubner, T.; Hillenbrand, R.; Keilmann, F. *Appl. Phys. Lett.* **2004,** *85,* 5064. doi:10.1063/1.1827334
9. Brehm, M.; Taubner, T.; Hillenbrand, R.; Keilmann, F. *Nano Lett.* **2006,** *6,* 1307. doi:10.1021/nl0610836
10. Kim, Z. H.; Liu, B.; Leone, S. R. *J. Phys. Chem. B* **2005,** *109,* 8503. doi:10.1021/jp047425i
11. Huber, A. J.; Keilmann, F.; Wittborn, J.; Aizpurua, J.; Hillenbrand, R. *Nano Lett.* **2008,** *8,* 3766. doi:10.1021/nl802086x
12. Qazilbash, M. M.; Brehm, M.; Chae, B.-G.; Ho, P.-C.; Andreev, G. O.; Kim, B.-J.; Yun, S. J.; Balatsky, A. V.; Maple, M. B.; Keilmann, F.; Kim, H.-T.; Basov, D. N. *Science* **2007,** *318,* 1750. doi:10.1126/science.1150124
13. Hillenbrand, R.; Keilmann, F. *Appl. Phys. Lett.* **2002,** *80,* 25. doi:10.1063/1.1428767
14. Hillenbrand, R.; Keilmann, F. *Phys. Rev. Lett.* **2000,** *85,* 3029. doi:10.1103/PhysRevLett.85.3029
15. Lowenstam, H. A. *Science* **1981,** *211,* 1126. doi:10.1126/science.7008198
16. Weiner, S.; Wagner, H. D. *Annu. Rev. Mater. Sci.* **1998,** *28,* 271. doi:10.1146/annurev.matsci.28.1.271
17. Meldrum, F. C.; Cölfen, H. *Chem. Rev.* **2008,** *108,* 4332. doi:10.1021/cr8002856
18. Schmahl, W. W.; Griesshaber, E.; Neuser, R.; Lenze, A.; Job, R.; Brand, U. *Eur. J. Mineral.* **2004,** *16,* 693. doi:10.1127/0935-1221/2004/0016-0693
19. Griesshaber, E.; Schmahl, W. W.; Neuser, R.; Pettke, T.; Blüm, M.; Mutterlose, J.; Brand, U. *Am. Mineral.* **2007,** *92,* 722. doi:10.2138/am.2007.2220
20. Goetz, A. J.; Steinmetz, D. R.; Griesshaber, E.; Zaeffere, S.; Raabe, D.; Kelm, K.; Irsen, S.; Sehrbock, A.; Schmahl, W. W. *Acta Biomater.* **2011,** *7,* 2237. doi:10.1016/j.actbio.2011.01.035
21. Merkel, C.; Griesshaber, E.; Kelm, K.; Neuser, R.; Jordan, G.; Logan, A.; Mader, W.; Schmahl, W. W. *J. Geophys. Res.* **2007,** *112,* G02008. doi:10.1029/2006JG000253
22. Schmahl, W. W.; Griesshaber, E.; Merkel, C.; Kelm, K.; Deuschle, J.; Neuser, R. D.; Göetz, A. J.; Sehrbrock, A.; Mader, W. *Mineral. Mag.* **2008,** *72,* 541. doi:10.1180/minmag.2008.072.2.541
23. Rey, C.; Shimizu, M.; Collins, B.; Glimcher, M. J. *Calcif. Tissue Int.* **1991,** *49,* 383. doi:10.1007/BF02555847
24. Pleshko, N.; Boskey, A.; Mendelsohn, R. *Biophys. J.* **1991,** *60,* 786. doi:10.1016/S0006-3495(91)82113-0
25. Carden, A.; Morris, M. D. *J. Biomed. Opt.* **2000,** *5,* 259. doi:10.1117/1.429994
26. Spencer, P.; Wang, Y.; Katz, J. L.; Misra, A. *J. Biomed. Opt.* **2005,** *10,* 031104. doi:10.1117/1.1914844
27. Boskey, A.; Mendelsohn, R. *J. Biomed. Opt.* **2005,** *10,* 031102. doi:10.1117/1.1922927
28. Abraham, J. A.; Sánchez, H. J.; Marceli, C. A.; Grenón, M.; Guidi, M. C.; Piccinini, M. *Anal. Bioanal. Chem.* **2011,** *399,* 1699. doi:10.1007/s00216-010-4430-0
29. Paschalis, E. P.; Mendelsohn, R.; Boskey, A. L. *Clin. Orthop. Relat. Res.* **2011,** *469,* 2170. doi:10.1007/s11999-010-1751-4
30. Tesch, W.; Eidelman, N.; Roschger, P.; Goldenberg, F.; Klaushofer, K.; Fratzl, P. *Calcif. Tissue Int.* **2001,** *69,* 147. doi:10.1007/s00223-001-2012-z
31. Paschalis, E. P.; DiCarlo, E.; Betts, F.; Sherman, P.; Mendelsohn, R.; Boskey, A. L. *Calcif. Tissue Int.* **1996,** *59,* 480. doi:10.1007/BF00369214
32. Gourion-Arsiquaud, S.; Faibish, D.; Myers, E.; Spevak, L.; Compston, J.; Hodsman, A.; Shane, E.; Recker, R. R.; Boskey, E. R.; Boskey, A. L. *J. Bone Miner. Res.* **2009,** *24,* 1565. doi:10.1359/jbmr.090414
33. Dalbeck, P.; England, J.; Cusack, M.; Lee, M. R.; Fallick, A. E. *Eur. J. Mineral.* **2006,** *18,* 601. doi:10.1127/0935-1221/2006/0018-0601
34. Feng, Q. L.; Li, H. B.; Pu, G.; Zhang, D. M.; Cui, F. Z.; Li, H. D.; Kim, T. N. *J. Mater. Sci.* **2000,** *35,* 3337. doi:10.1023/A:1004843900161
35. Griesshaber, E.; Kelm, K.; Jordan, G.; Xu, D.; Schmahl, W. W. In preparation.
36. Taubner, T.; Keilmann, F.; Hillenbrand, R. *Opt. Express* **2005,** *13,* 8893. doi:10.1364/OPEX.13.008893
37. Zaslansky, P. In *Collagen: Structure and Mechanics;* Fratzl, P., Ed.; Springer: Berlin, Heidelberg, 2008.
38. Mjör, I. A.; Nordahl, I. *Arch. Oral Biol.* **1996,** *41,* 401. doi:10.1016/0003-9969(96)00008-8
39. Roschger, P.; Fratzl, P.; Eschberger, J.; Klaushofer, K. *Bone* **1998,** *23,* 319. doi:10.1016/S8756-3282(98)00112-4
40. Raschke, M. B.; Lienau, C. *Appl. Phys. Lett.* **2003,** *83,* 5089. doi:10.1063/1.1632023
41. Sun, J.; Schotland, J. C.; Hillenbrand, R.; Carney, P. S. *Appl. Phys. Lett.* **2009,** *95,* 121108. doi:10.1063/1.3224177
42. Lowenstam, H. A.; Weiner, S. *Science* **1985,** *227,* 51. doi:10.1126/science.227.4682.51
43. Lee, A. P.; Brooker, L. R.; Macey, D. J.; van Bronswijk, W.; Webb, J. *Calcif. Tissue Int.* **2000,** *67,* 408. doi:10.1007/s002230001156
44. Thurner, P. J.; Lam, S.; Weaver, J. C.; Morse, D. E.; Hansma, P. K. *J. Adhes.* **2009,** *85,* 526. doi:10.1080/00218460902996424
45. Becker, A.; Ziegler, A.; Epple, M. *Dalton Trans.* **2005,** 1814. doi:10.1039/b412062k
46. Hillenbrand, R.; Taubner, T.; Keilmann, F. *Nature* **2002,** *418,* 159. doi:10.1038/nature00899
47. Ocelic, N.; Hillenbrand, R. *Nat. Mater.* **2004,** *3,* 606. doi:10.1038/nmat1194
48. Wells, O. C. *Scanning Electron Microsc.* **1977,** *1,* 747.
49. Kravitz, L. C.; Kingsley, J. D.; Elkin, E. L. *J. Chem. Phys.* **1968,** *49,* 4600. doi:10.1063/1.1669918
50. Fuchs, R. *Phys. Rev. B* **1975,** *11,* 1732. doi:10.1103/PhysRevB.11.1732
51. Bohren, C. F.; Huffmann, D. R. *Absorption and Scattering of Light by Small Particles;* Wiley: New York, 1983.
52. Balan, E.; Delattre, S.; Roche, D.; Segalen, L.; Morin, G.; Guillaumet, M.; Blanchard, M.; Lazzeri, M.; Brouder, C.; Salje, E. K. H. *Phys. Chem. Miner.* **2011,** *38,* 111. doi:10.1007/s00269-010-0388-x
53. Penel, G.; Leroy, G.; Rey, C.; Sombret, B.; Huvenne, J. P.; Bres, E. *J. Mater. Sci.: Mater. Med.* **1997,** *8,* 271. doi:10.1023/A:1018504126866
54. Leroy, G.; Leroy, N.; Penel, G.; Rey, C.; Lafforgue, P.; Bres, E. *Appl. Spectrosc.* **2000,** *54,* 1521. doi:10.1366/0003702001948448

55. Knoll, B.; Keilmann, F. *Opt. Commun.* **2000,** *182,* 321. doi:10.1016/S0030-4018(00)00826-9
56. Giessibl, F. J. *Science* **1995,** *267,* 68. doi:10.1126/science.267.5194.68
57. Richter, M.; Hedegaard, M.; Deckert-Gaudig, T.; Lampen, P.; Deckert, V. *Small* **2011,** *7,* 209. doi:10.1002/smll.201001503
58. Zaslansky, P.; Zabler, S.; Fratzl, P. *Dent. Mater.* **2010,** *26,* e1. doi:10.1016/j.dental.2009.09.007
59. Bruggeman, D. A. G. *Ann. Phys. (Berlin, Ger.)* **1935,** *416,* 636. doi:10.1002/andp.19354160705
60. Hinrichs, K.; Röseler, A.; Roodenko, K.; Rappich, J. *Appl. Spectrosc.* **2008,** *62,* 121. doi:10.1366/000370208783412744

License and Terms

Beilstein Journal of Nanotechnology

Combining nanoscale manipulation with macroscale relocation of single quantum dots

Francesca Paola Quacquarelli[1], Richard A. J. Woolley[2], Martin Humphry[3], Jasbiner Chauhan[2], Philip J. Moriarty[2] and Ashley Cadby[*1]

Letter

Open Access

Address:
[1]The Department of Physics and Astronomy, The Hicks Building, The University of Sheffield, Hounsfield Rd, Sheffield, South Yorkshire, S3 7RH, UK, [2]School of Physics and Astronomy, University of Nottingham, Nottingham, NG7 2RD UK and [3]Phase Focus Limited, The Kroto Innovation Centre, The University of Sheffield, North Campus, Broad Lane, Sheffield, S3 7HQ, UK

Email:
Ashley Cadby[*] - a.cadby@sheffield.ac.uk

* Corresponding author

Keywords:
automation; nanoscale manipulation; nanotechnology; quantum dots; single molecule spectroscopy

Beilstein J. Nanotechnol. **2012,** *3,* 324–328.
doi:10.3762/bjnano.3.36

Received: 05 January 2012
Accepted: 14 March 2012
Published: 10 April 2012

This article is part of the Thematic Series "Nanophotonics, nano-optics and nanospectroscopy".

Guest Editor: A. J. Meixner

Abstract

We have controllably positioned, with nanometre precision, single CdSe quantum dots referenced to a registration template such that the location of a given nanoparticle on a macroscopic (≈1 cm^2) sample surface can be repeatedly revisited. The atomically flat sapphire substrate we use is particularly suited to optical measurements of the isolated quantum dots, enabling combined manipulation–spectroscopy experiments on a single particle. Automated nanoparticle manipulation and imaging routines have been developed so as to facilitate the rapid assembly of specific nanoparticle arrangements.

Introduction

Techniques such as scanning probe microscopy and transmission electron microscopy have been used extensively to provide crucial high-resolution structural and morphological information on nanoscale systems. Measurement of the optical properties of a nanostructured material or nanoscale device with a resolution comparable to the length scale of the system of interest, however, continues to present a challenge. A number of techniques have been developed to push the resolution of optical microscopy and spectroscopy to the single-molecule/particle limit. These include scanning near-field optical microscopy (SNOM) [1-3] and techniques based on adaptations of single-molecule spectroscopy [4], such as fluorescence imaging with one-nanometer accuracy (FIONA) [5], stochastic optical reconstruction microscopy (STORM) [6]. These techniques require the fluorophore under observation to be isolated by distances larger than the diffraction limit of the microscope.

The study of single fluorophores separated by distances larger than the diffraction limit has proven to be a valuable tool in understanding the optical properties of a broad range of nanostructured systems, including conjugated polymers [7], biomolecules [8,9], and quantum dots [10]. Nonetheless, these techniques fundamentally rely on a statistical distribution of molecules and are therefore not optimal for the study of specific isolated nanostructures at well-defined locations on a surface. Recent attempts at the positioning of quantum dots (QDs) based on electro-osmotic flow control (EOFC) [11,12] have resulted in a positioning precision of 130 nm when particle diffusion is suppressed. In a challenging recent experiment, atomic force microscopy (AFM) was used to manipulate a single gold nanoparticle (≈35 nm) to approach a single quantum dot [13]. The gold nanoparticle was shown to dramatically quench the optical lifetime of the QD and to completely suppress its blinking.

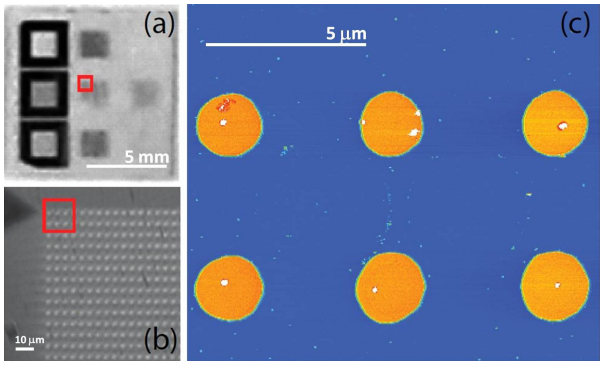

Figure 1: (a) An optical image of nine different reference grids on a 10 × 10 mm^2 sapphire substrate; (b) Optical zoom showing the grid structure comprising gold pillars 2 µm in diameter, 75 nm tall, with a centre-to-centre distance of 5 µm; (c) AFM image of a number of the grid cells. Quantum dots (QDs) are visible as small dots in the image.

Experimental

In this work, we position a single fluorophore, a CdSe QD, with nanometre precision on a macroscopic registration template, using automated atomic force microscopy (AFM) techniques. Our approach differs from previous work [13] in that we have manipulated, and subsequently re-located and spectroscopically identified, single nanoparticles of less than 5 nm diameter on an atomically flat substrate. Sapphire was selected as a suitable substrate as it is transparent across most of the visible spectrum [14] and comprises wide, atomically flat terraces (200 nm across) separated by steps only 0.22 nm in height. Moreover, as sapphire is an excellent electrical insulator it shows minimal quenching of optically excited states [13,15]. A simple optical lithography patterning procedure allows us to (re-)locate a given, previously positioned, QD in any optical system. To manipulate and characterise a single quantum dot we required the ability to repeatedly address an area of only a few square nanometres on a 10 × 10 mm^2 substrate. In order to realise this relocation capability, the sapphire substrate was patterned by using a grid of gold pillars as shown in Figure 1a.

The center-to-center distance of the pillars is 5 µm and the pillar height 75 nm. Four pillars form a single cell, which can be repeatedly addressed in both an optical microscope and by AFM by simply assigning each cell an X, Y coordinate. An AFM height image for cells A1–B1, using our reference notation detailed below, is shown in Figure 1c This enabled the re-location of single nanoparticles so that they could be analysed using a number of different techniques including optical microscopy, single-molecule microscopy, and atomic force microscopy. Importantly, the samples discussed here were transferred between two laboratories separated by ≈50 km, but it was possible to study the same nanoparticle in both labs. The quantum dots used in this work were CdSe/ZnS core/shell hydrophobic nanocrystals (PlasmaChem [16]), coated with hydrophobic organic molecules (TOPO and HDA [16]) and with a maximum emission wavelength of 610 nm. To prepare a sample suitable for manipulation experiments, the nanocrystals were dispersed in HPLC-grade toluene and the concentration varied until a QD number density of ≈10 QD per square micron on the patterned sapphire substrate was achieved. For AFM imaging and manipulation we used an Asylum MFP-3D atomic force microscope in tapping mode (imaging) or contact mode (manipulation) with AC240TS Olympus AFM cantilevers. Several cells were imaged over a large scan, typically 20–40 µm in size. From these initial scans a cell that had a small number of suitable quantum dots (and showed little adsorbed contamination) was selected for the manipulation region.

For a specific manipulation experiment, an individual QD having a line profile (height/lateral extent) appropriate for a single CdSe nanoparticle (as ascertained statistically from measurements of a large number of QDs) was selected, ensuring that it was at least one micron from the pillars and preferably close to the centre of the cell, as shown in Figure 2. The remaining unwanted QDs were moved away from the selected QD by using the AFM as follows: A suitable bitmap image was used as a mask to define the area of the substrate that was to be subjected to the *clearing* process, as shown in Figure 2b [17]. (A circular or square bitmap with an aperture centred on the selected QD was typically used). The AFM then performed a contact mode sweep in the area covered by the bitmap. The bitmap defined the areas in which the contact mode setpoint was high, i.e., an increased tip–sample interaction force is present. Figure 2b shows the regions of high contact force and the direction of travel of the AFM probe. Areas for which the bitmap was transparent corresponded to regions in which a low

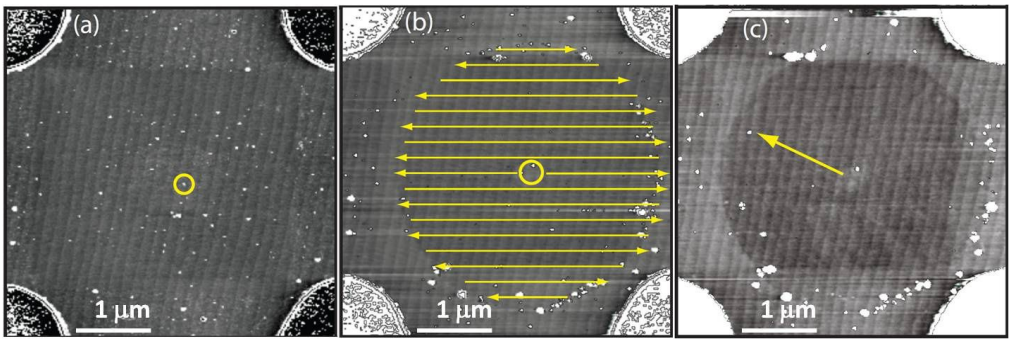

Figure 2: Isolation and manipulation of a single QD. (a) A typical cell after QDs have been spin cast on to the surface. The QD selected for study is highlighted with a yellow circle; (b) The yellow lines show the path that the AFM tip takes in contact mode, clearing a circle around the selected QD. (c) An area around the QD is cleared leaving only two QDs in the centre of the cell. The final QD is removed by nudging the QD with the AFM tip in contact mode with a high tip–sample interaction force. The approximately parallel lines seen in each of the images are atomic step edges on the sapphire substrate.

tip–sample interaction was required (e.g., close to the QD of interest). The use of manipulation masks of this type enabled a large area of the sample to be swept free of QDs quickly, leaving only the QD of interest (Figure 2c). Finally, and if required, the remaining QD can be nudged into place by using the AFM tip or a QD near to the QD of interest can be moved.

Results and Discussion

Optical measurements of the isolated QD were taken on a custom single-molecule spectrometer as described in the work of Khalil et al. [18]. A white-light image of the sample was used to identify the cell of interest, Figure 3a. (Without the gold registration markers it would of course be practically impossible to identify the manipulated QDs on any microscope other than the AFM used to perform the manipulation). Figure 3a shows the superposition of a white-light image and a laser-spot image taken at the same time, in which the laser spot can be seen in cell A2. The image shown in Figure 3a is of the same grid cell as that in Figure 1a. An AFM image of cell B1 is shown in Figure 3b in which all of the QDs except one have been removed from the cell, leaving a single dot in the centre.

To investigate the optical properties of single QDs after manipulation, the sample was excited with the 442 nm line of a He:Cd laser, this produced a 1 µm laser spot on the surface, as shown in Figure 3a. The sample was translated until the laser spot overlapped with the know position of the manipulated QD. The slit width of the monochromator was reduced to allow only light from the laser spot to enter, and the QD photoluminescence was collected. The sample was then translated by 1 µm to a section of the sample that had been cleaned of QDs, and a second spectrum was taken from that area. The two corresponding spectra are shown in Figure 3c. Both spectra contain several sharp features between 650 nm and 750 nm arising from photoluminescence (PL) caused by the sapphire substrate and are likely due to chromium ions [19]. The PL spectrum taken on the manipulated QD is centred at 608 nm, and luminescence at this wavelength is completely absent elsewhere in the cell. The full-

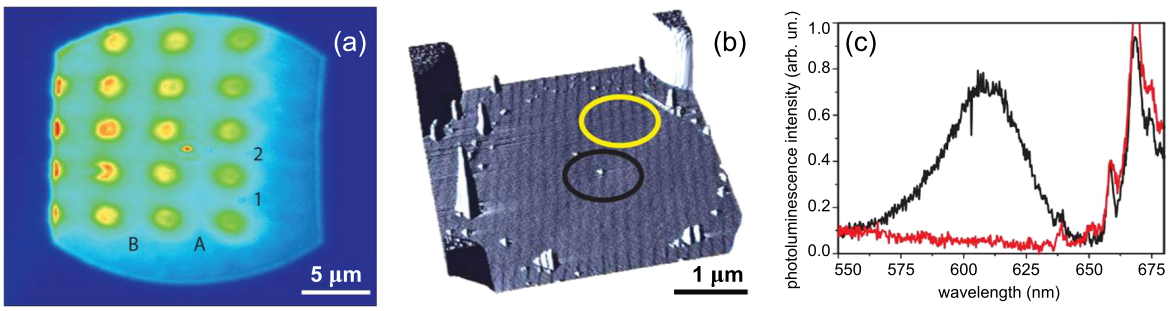

Figure 3: (a) A white-light image of several cells. The laser spot can be seen in cell A2; (b) An AFM image of cell B1. The black circle shows a single isolated QD, while the yellow circle indicates an area that has been cleared of QDs; (c) Photoluminescence spectrum from the areas of the cell highlighted in (b) after excitation with the 442 nm line of a He:Cd laser. The 610 nm QD emission can be clearly seen in the black spectrum. The emission above 650 nm is due to chromium contamination in the sapphire substrate.

width at half-maximum (FWHM) of the QD spectra is 108 meV, which corresponds well to the previously studied emission from single colloidal quantum dots, for which PL blinking was recorded to optically identify the emission as being that from a single QD [20,21]. Due to limitations in the collection optics it was not possible to see blinking in our sample.

The PL contamination, caused by chromium defects in the sapphire, limits the use of this substrate to QDs with peak emission wavelengths below 650 nm or above 750 nm. We have also manipulated and imaged other QDs with peak emission wavelengths at 440 nm, 550 nm and 780 nm on sapphire. It was seen that the manipulation of the QD does not affect the QD emission: QDs that have been moved over several microns in the clearing process still emit at the expected central wavelength and are highly luminescent.

The manipulation of each quantum dot requires several hours of intensive AFM work by a highly skilled operator, and thus this is hardly a cost-effective, scalable process. To address this issue, we have taken steps to automate the process of identifying the registration template and experimental cells; identifying the nano-particles suitable for manipulation; and, finally, identifying the correct parameters to perform the manipulation itself. Figure 4a shows how the automation software locates the coordinates of the experimental cells, then zooms in and identifies the cell contents (Figure 4c and Figure 4d).

We employ a simple object-classification algorithm, which identifies particles on the substrate surface based on their topographic dimensions. As QDs have very specific heights and ratios of surface-area to volume, it is possible to set strict parameters on what can be considered a suitable single QD and what can be classed as a clump of QDs or contamination. This process can be performed iteratively, which allows for a re-evaluation of the sample after each manipulation and means that the system can identify manipulations that have resulted in a break up of a cluster or a manipulation that has not successfully manipulated a single QD. Our manipulation routines are also quite uncomplicated, using the AFM in contact mode rather than lift mode, allowing us to maintain feedback as the nanoparticles are pushed. Importantly, we can ascertain the minimum amount of surface–tip contact force required for the manipulation to take place; reducing tip wear and image degradation. Tip state also plays an important role in the manipulation process, and the automatic characterisation and optimization of the AFM tip apex would be beneficial, as has been shown for STM imaging [22].

By using this method it is possible to greatly increase the number of manipulations that can be completed, and it allows for the possibility of performing manipulations to create an individual and distinctive structure in each cell without the need for an operator. As the colour of a QD is size-dependent, the manipulation algorithm could be used with dual-colour samples in order to build up structures in which energy transfer is utilized.

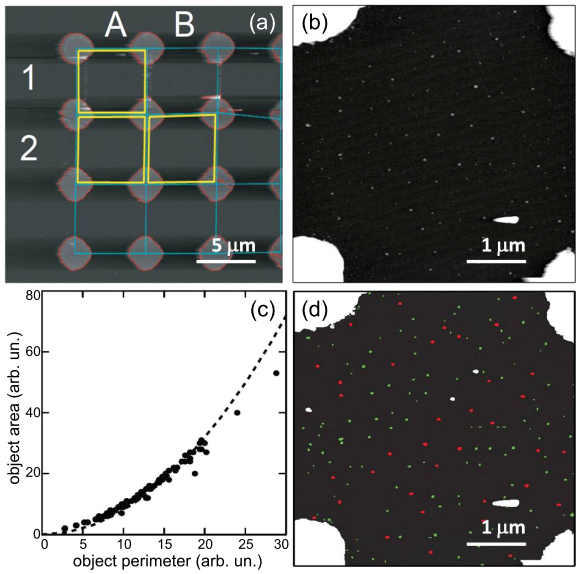

Figure 4: (a) The automation algorithm identifies the experimental cells from the macroscopic reference grid, (b) then zooms in. Each object over a given height threshold is classified according to its dimensions (c) (the dotted line indicates the area:perimeter ratio of a circle). The result of this classification is given in (d): larger noncircular features are classified as contaminations or QD clumps (white), whereas single quantum dots are given a red (larger) or green (smaller) colouration (indicating their position in the QD size distribution).

Conclusion

We have shown that it is possible to isolate and manipulate individual CdSe quantum dots on a sapphire surface and subsequently relocate the same QD within a macroscopic (centimetres squared) area to measure its optical properties. We have also taken initial steps pto scale the process by computer automation with possible applications in the fabrication of nanoscale devices.

References

1. Cadby, A.; Dean, R.; Fox, A. M.; Jones, R. A. L.; Lidzey, D. G. *Nano Lett.* **2005,** *5,* 2232. doi:10.1021/nl051525y
2. Gerton, J. M.; Wade, L. A.; Lessard, G. A.; Ma, Z.; Quake, S. R. *Phys. Rev. Lett.* **2004,** *93,* 180801. doi:10.1103/PhysRevLett.93.180801
3. Pohl, D. W.; Denk, W.; Lanz, W. *Appl. Phys. Lett.* **1984,** *44,* 651. doi:10.1063/1.94865
4. Müller, J. G.; Lemmer, U.; Raschke, G.; Anni, M.; Scherf, U.; Lupton, J. M.; Feldmann, J. *Phys. Rev. Lett.* **2003,** *91,* 267403. doi:10.1103/PhysRevLett.91.267403

5. Yildiz, A.; Forkey, J. N.; McKinney, S. A.; Ha, T.; Goldman, Y. E.; Selvin, P. R. *Science* **2003,** *300,* 2061. doi:10.1126/science.1084398
6. Rust, M. J.; Bates, M.; Zhuang, X. *Nat. Methods* **2006,** *3,* 793. doi:10.1038/nmeth929
7. Gesquiere, A. J.; Park, S.-J.; Barbara, P. F. *J. Phys. Chem. B* **2004,** *108,* 10301. doi:10.1021/jp049583f
8. Weiss, S. *Science* **1999,** *283,* 1676. doi:10.1126/science.283.5408.1676
9. Chaudhuri, D.; Galusha, J. W.; Walter, M. J.; Borys, N. J.; Bartl, M. H.; Lupton, J. M. *Nano Lett.* **2009,** *9,* 952. doi:10.1021/nl802819n
10. Banin, U.; Bruchez, M.; Alivisatos, A. P.; Ha, T.; Weiss, S.; Chemla, D. S. *J. Chem. Phys.* **1999,** *110,* 1195. doi:10.1063/1.478161
11. Ropp, C.; Probst, R.; Cummins, Z.; Kumar, R.; Berglund, A. J.; Raghavan, S. R.; Waks, E.; Shapiro, B. *Nano Lett.* **2010,** *10,* 2525. doi:10.1021/nl101105j
12. Ropp, C.; Cummins, Z.; Probst, R.; Qin, S.; Fourkas, J. T.; Shapiro, B.; Waks, E. *Nano Lett.* **2010,** *10,* 4673. doi:10.1021/nl1029557
13. Ratchford, D.; Shafiei, F.; Kim, S.; Gray, S. K.; Li, X. *Nano Lett.* **2011,** *11,* 1049. doi:10.1021/nl103906f
14. Apetz, R.; van Bruggen, M. P. B. *J. Am. Ceram. Soc.* **2003,** *86,* 480. doi:10.1111/j.1151-2916.2003.tb03325.x
15. Govinda, S.; Rao, K. V. *Phys. Status Solidi A* **1975,** *27,* 639. doi:10.1002/pssa.2210270237
16. Plasmachem // ADDO, Galvanoadditive, DLC, TRIO, Nanoluminograph, Sedimentation Gauge, BET, Carbon Analysis, Custom Synthesis. http://www.plasmachem.com (accessed Jan 4, 2012).
17. Excess HDA ligands are present in the commercial nanocrystal samples we used. This possibly accounts for the observation of the darker region in Figure 2b and Figure 2c, due to the removal of HDA from the sample surface while performing the manipulation scan.
18. Khalil, G. E.; Adawi, A. M.; Fox, A. M.; Iraqi, A.; Lidzey, D. G. *J. Chem. Phys.* **2009,** *130,* 044903. doi:10.1063/1.3054142
19. Kadlečíková, M.; Breza, J.; Veselý, M.; Červeň, I. *Microelectron. J.* **2003,** *34,* 95. doi:10.1016/S0026-2692(02)00173-8
20. Li, Q.; Han, R.; Meng, X.; Gai, H.; Yeung, E. S. *Anal. Biochem.* **2008,** *377,* 176. doi:10.1016/j.ab.2008.03.017
21. Nikiforov, M. P.; Jesse, S.; Morozovska, A. N.; Eliseev, E. A.; Germinario, L. T.; Kalinin, S. V. *Nanotechnology* **2009,** *20,* 395709. doi:10.1088/0957-4484/20/39/395709
22. Woolley, R. A. J.; Stirling, J.; Radocea, A.; Krasnogor, N.; Moriarty, P. J. *Appl. Phys. Lett.* **2011,** *98,* 253104. doi:10.1063/1.3600662

License and Terms

BEILSTEIN JOURNAL OF NANOTECHNOLOGY

Controlling the optical and structural properties of ZnS–$AgInS_2$ nanocrystals by using a photo-induced process

Takashi Yatsui*, Fumihiro Morigaki and Tadashi Kawazoe

Full Research Paper

Open Access

Address:
School of Engineering, University of Tokyo, Bunkyo-ku, Tokyo 113-8656, Japan

Email:
Takashi Yatsui* - yatsui@ee.t.u-tokyo.ac.jp

* Corresponding author

Keywords:
low toxicity; self-assembly; visible-light-emitting nanocrystals; ZnS–$AgInS_2$ (ZAIS)

Beilstein J. Nanotechnol. **2014,** *5,* 1767–1773.
doi:10.3762/bjnano.5.187

Received: 17 June 2014
Accepted: 24 September 2014
Published: 14 October 2014

This article is part of the Thematic Series "Nanophotonics, nano-optics and nanospectroscopy".

Guest Editor: A. J. Meixner

Abstract

ZnS–$AgInS_2$ (ZAIS) solid-solution nanocrystals are promising materials for nanophotonic devices in the visible region because of their low toxicity and good emission properties. We developed a technique of photo-induced synthesis to control the size and composition of the ZAIS nanocrystals. This method successfully decreased the defect levels, as well as the size and size variation of ZAIS nanocrystals by controlling the excitation wavelength during synthesis. Detailed analysis of transmission electron microscope images confirmed that the photo-induced synthesis yielded a high crystallinity of the ZAIS nanocrystals with small variations in size and content.

Introduction

Continued innovation in optical technology is essential for the advancement of information-processing systems. In particular, it is important to reduce both the size and energy consumption of photonic devices to ensure successful integration [1]. To reduce the size of photonic devices beyond the diffraction limit, the photons should be coupled with material excitation such as electrons in metallic materials [2]. To avoid absorption loss in metallic materials, we have proposed nanophotonic devices using semiconductor quantum structures, including quantum cubes [3], quantum dots (QDs) [4], quantum wells [5], and quantum rings [6]. Kawazoe et al., have demonstrated the room-temperature operation of AND-gate and NOT-gate devices using InAs QD pairs [7]. In a nanophotonic device, near-field energy-transfer via a dipole-forbidden energy state, which is unattainable in conventional photonic devices, is used [8]. The near-field energy-transfer originates from an exchange of virtual photons between the resonant energy states [9], where the virtual photons on a nanoparticle activate the dipole-forbidden energy state.

The successful fabrication of a nanophotonic device requires the control of its size to ensure that the quantized energy levels are

resonant to facilitate an efficient optical near-field interaction. The solution process could be a promising process for this purpose because it can easily regulate the size and shape by controlling the growth kinetics [10]. It affords precise control over the size of CdSe QDs with a very low size variation that is as small as a fifth of the atomic interface [11], and it has been used to manufacture commercially available display devices [12]. On the other hand, the reduction of toxic components such as Cd and Se is required. Therefore, ZnS–$AgInS_2$ solid-solution (ZAIS) nanocrystals [13] are promising materials for nanophotonic devices in the visible region because of their low toxicity. In addition, since ZAIS nanocrystals have long decay times for emissions [14], it can be applied to optical buffer memory [15]. To realize a room-temperature operation of nanophotonic devices, the spectrum width of photoluminescence (PL) needs to be narrowed. Emission-wavelength controlled nanocrystals with a narrow spectral range are also of great interest for display devices. This is because nanometer-scale control in wavelength is required for the color display to tune the color rendering index. To meet this requirement, size control at the scale of single atoms is required [12]. We performed laser-assisted synthesis of ZAIS nanocrystals to meet those requirements.

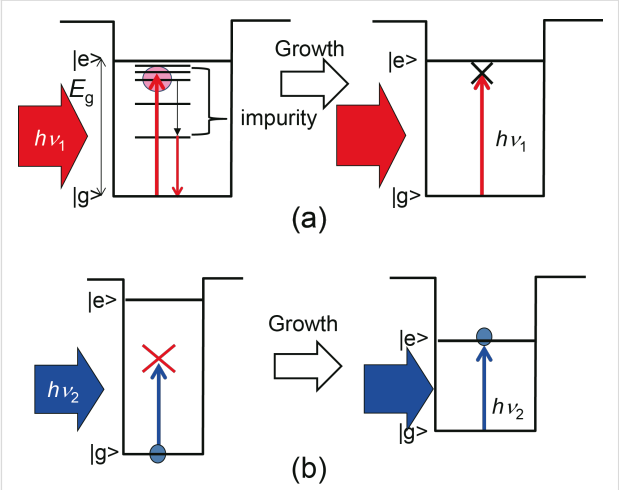

Figure 1: Schematic of the photo-induced synthesis. (a) Selective etching of defect levels. The relationship between the energy of an incident photon and the band structure of a ZAIS nanocrystal is shown in the left panel. As growth proceeds, the defect levels disappear, resulting in the high-quality nanocrystal at the end (right panel). (b) Controlling the size of a nanocrystal. The relationship between the energy of an incident photon and the band structure of a ZAIS nanocrystal is shown in the left panel. As growth proceeds, the size of the nanocrystal increases and the band gap energy decreases below the energy of the incident photon. Electron–hole pairs are then excited and trigger an oxidation–reduction reaction in the ZAIS nanocrystal and growth halts (right panel).

Results and Discussion

Photo-induced synthesis

Defects or impurities must be removed to reduce the spectral width and to obtain a higher crystal quality [14,16]. Since the energy level corresponding to a defect or an impurity in ZAIS nanocrystals is lower than the band gap energy (E_g), the excited carriers are trapped at the inter-band defect levels. Consequently, the quantum efficiency of the ZAIS nanocrystals decreases if a larger number of defect levels is present. However, when illuminated by a photon with an energy of $h\nu_1$, which is larger than the defect levels and smaller than E_g, defect levels are removed preferentially. This occurs because photo-induced etching takes place in the areas with defects as a result of local oxidation–reduction reactions after the excited electron–hole pairs have relaxed to those defect areas in ZAIS nanocrystals (Figure 1a). During the photo-synthesis of ZAIS nanocrystals with the illumination photon energies exceeding E_g, excitons induce an oxidation–reduction reaction in the nanocrystals. Consequently, the etching of the deposited ZAIS atoms on the nanocrystals surface proceeds. The growth rate is controlled by the absorbed light intensity and wavelength, which control the nanocrystal size. Similar photo-synthesis for controlling the size of nanocrystals have been reported for CdSe [14], ZnO [16,17], and Si [18] (Figure 1b).

We measured the excitation spectra of the synthesized ZAIS nanocrystals to find the optimum wavelength for controlling the spectra. Based on the synthesis method described in [13], solid-solution nanocrystals of ZAIS were synthesized by thermal decomposition of a metal-ion–diethyldithiocarbamate complex of $(AgIn)_xZn_{2(1-x)}(S_2CN(C_2H_6)_2)_4$. Here, we set x to 0.5 for all experiments. By using 50 mg of the precursor powder, ZAIS nanocrystals were synthesized as follows: Step (1): The precursor was annealed at 180 °C for 30 min in a N_2 atmosphere, yielding a brown powder. Step (2): Oleylamine was added to the brown powder obtained in step (1), followed by further annealing at 180 °C for a time t (defined as the growth time for this process) in a N_2 atmosphere to grow ZAIS nanocrystals. During the crystal growth in this annealing process, irradiation with light was introduced to control the size and crystallinity. Step (3): Large particles were removed from the resulting suspension by centrifugation. By adding methanol, the ZAIS nanocrystals were separated from the supernatant.

Figure 2a and Figure 2b show the excitation spectra of fabricated ZAIS without laser irradiation during step (2), in which ZAIS nanocrystals were synthesized in t = 60 min. Figure 2c shows a typical emission spectrum obtained after excitation at 440 nm. This spectrum had a broad spectral width, with several emission peaks at 620 (peak I), 650 (peak II), and 720 nm (peak III) in addition to the main emission peak at around 550 nm. The main peak should have originated from the emission from the band edge of ZAIS and the remaining peaks should have

originated from the defect levels. Based on these results, 593 nm light (λ_1) was chosen to decrease the number of impurity sites. As this wavelength was longer than the spectral peak wavelength around 550 nm, it prevented carrier excitation in the ZAIS nanocrystals (see Figure 1a). In addition, to control the size of the ZAIS nanocrystals, 532 nm light (λ_2) was used so that the ZAIS nanocrystals would absorb the light (see Figure 1b).

Selective reduction of defect levels

To realize selective etching of the defect levels, ZAIS nanocrystals were synthesized with 593 nm light (λ_1) illumination (10 mW) during the heat treatment in step (2). Figure 3a shows the dependence of the PL spectra obtained with the 325 nm light excitation on the growth time, t. A large spectral change was observed at t = 60 min at emission wavelengths $\lambda > 550$ nm, which was confirmed by obtaining the differential of the PL spectra (open circles in Figure 3b). The differential PL spectrum (= $PL_{without} - PL_{with}$) was fitted by using three curves: curve A with a peak wavelength of 515 nm, curve II with a peak wavelength of 650 nm, and curve III with a peak wavelength of 720 nm. The peak wavelengths of curves II and III corresponded to those in Figure 2c, thus indicating that the impurity sites were selectively etched away. Meanwhile, the spectral peak around 515 nm increased (i.e., the differential PL intensity decreased), whose wavelength corresponded to the main emission peak in Figure 2c. These results indicate that the decrease in impurity sites resulted in the decrease of the non-radiative energy dissipation, and resulted in the increase of the emission intensity of the band edge.

Using the emission spectra to control the nanocrystal size

For the investigation of ways to control the size of ZAIS nanocrystals, we synthesized ZAIS nanocrystals with 532 nm irradiation (λ_2) during the heat treatment in step (2). Figure 4a shows the PL spectra with different excitation power levels during the synthesis. From these spectra, the differential PL spectra (= $PL_{without} - PL_{with}$) were obtained, as shown in Figure 4b. The positive value of the differential PL intensity at

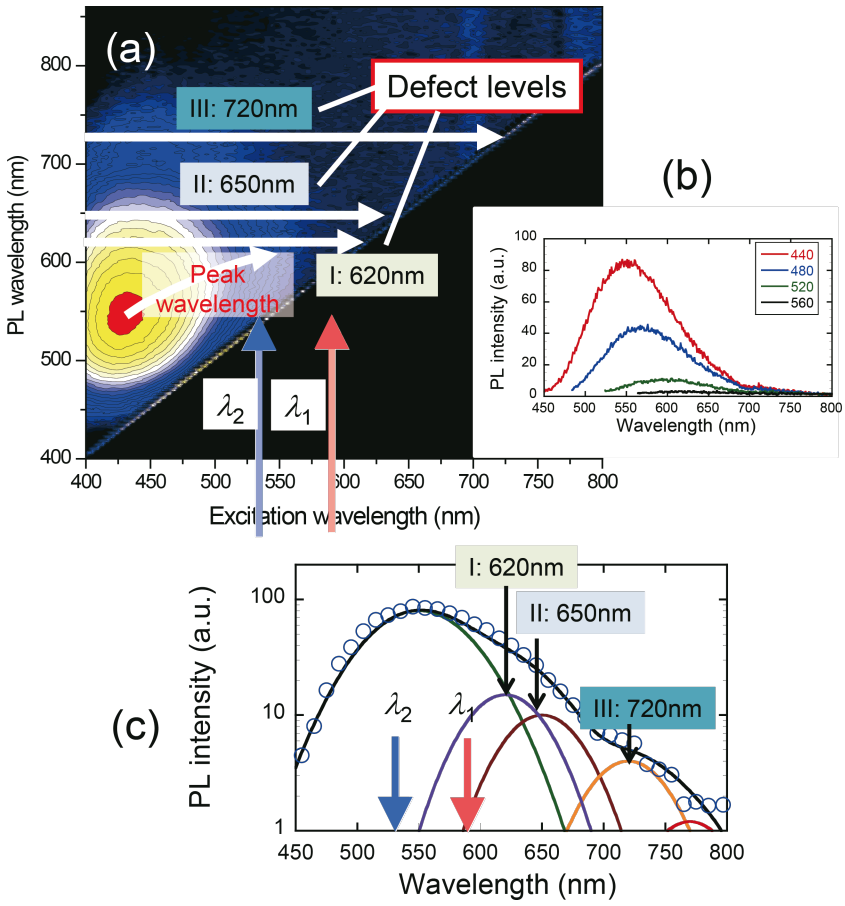

Figure 2: (a) Dependence of PL spectra on excitation wavelength. (b) PL spectra obtained with excitation wavelengths of 440, 480, 520, and 560 nm. (c) Fitted PL spectrum (the same as the red curve in (b)) and several Lorenz curves with peak wavelengths of 550, 620, 650, and 720 nm.

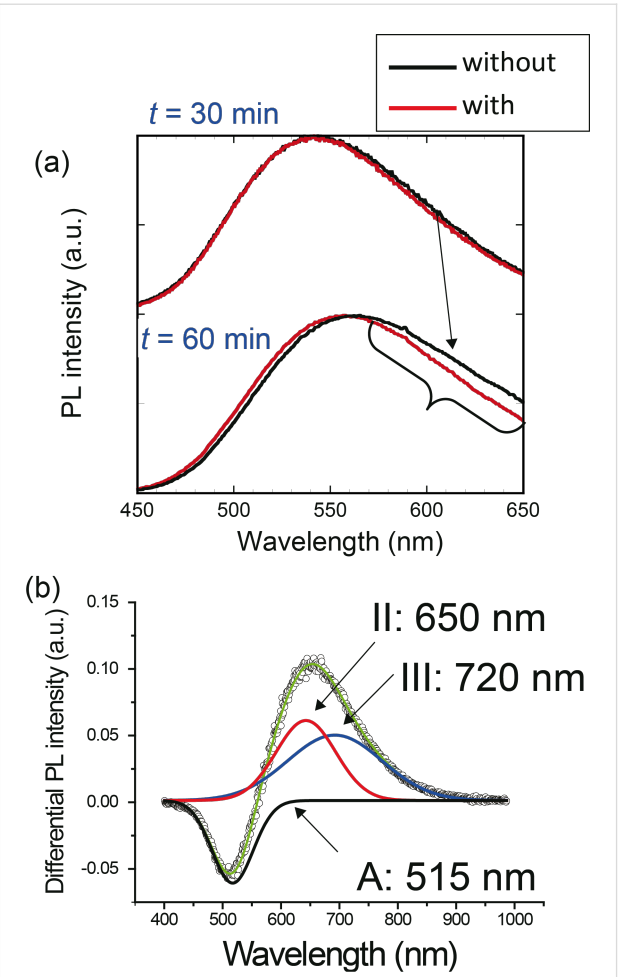

Figure 3: (a) PL spectra obtained with 593 nm light (λ_1) as functions of the growth time, *t*. Black solid lines: spectra of nanocrystals obtained without light irradiation, $PL_{without}$. Red solid lines: spectra of nanocrystals obtained with light irradiation, PL_{with}. (b) Differential PL spectra calculated from the spectra obtained (after *t* = 60 min) with irradiation (red line in (a)) and without irradiation (black line in (a)).

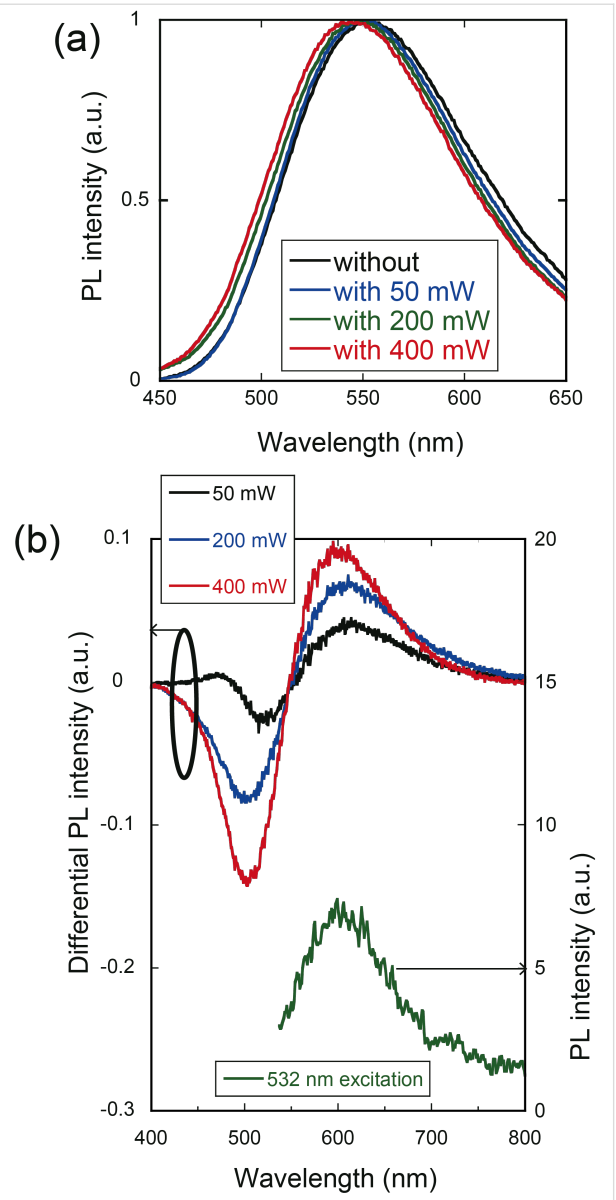

Figure 4: (a) PL spectra obtained with 532 nm light (λ_2) and different levels of irradiation power. (b) (Left vertical axis) Differential PL spectra calculated from spectra obtained with and without irradiation. (Right vertical axis) PL spectrum of ZAIS nanocrystals grown without laser irradiation. The PL spectrum was obtained by using 532 nm light.

600 nm indicates a decrease in the PL intensity of ZAIS nanocrystals synthesized with laser irradiation. Because the peak wavelength (600 nm) corresponded to the peak PL wavelength for ZAIS nanocrystals synthesized without laser irradiation, using an excitation wavelength of 532 nm (solid green line in Figure 4b), the decrease in PL intensity of the nanocrystals synthesized with 532 nm light excitation should have originated from carrier excitation by the 532 nm light. In addition, the differential PL intensity at shorter wavelengths around 500 nm was decreased, which indicates that the number of ZAIS nanocrystals with smaller size was increased.

Transmission electron microscopy analysis of crystal size and shape

Next, we evaluated the size distributions by using a transmission electron microscope (TEM, Hitachi H-9000NAR, acceleration voltage of 300 kV) to confirm the variations among the nanocrystals. Figure 5 and Figure 6 show the typical TEM images of synthesized ZAIS nanocrystals without and with 532 nm light (400 mW), obtained after *t* = 60 min, in which the red line indicates the outer shape of the nanocrystals. We evaluated the diameter by using high-magnification images (4,000,000×). We determined the edge of the nanocrystals by using the IMTool (Foundation for Promotion of Material Science and Technology of Japan). By taking the cross-sectional profiles, the edge of the nanocrystals is determined by the disappearance of the periodic contrast. Figure 7a and

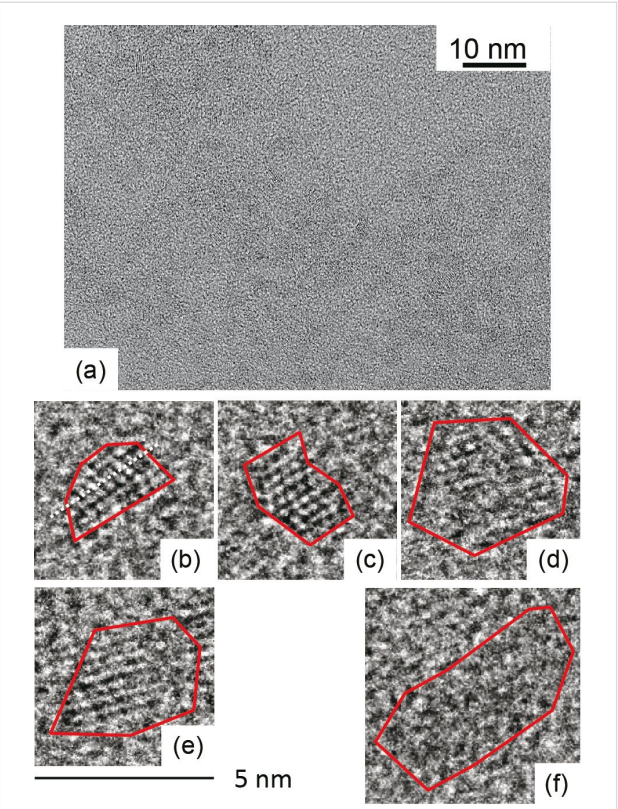

Figure 5: TEM images of ZAIS nanocrystals grown without irradiation, t = 60 min; (a) low (2,000,000×) and (b–f) high (4,000,000×) magnification.

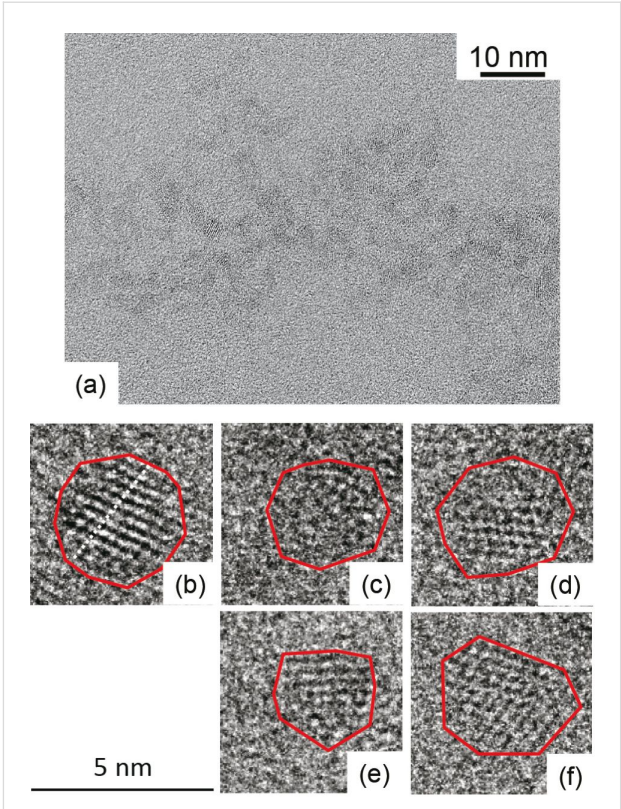

Figure 6: TEM images of ZAIS nanocrystals grown with 532 nm light (400 mW), t = 60 min; (a) low (2,000,000×) and (b–f) high (4,000,000×) magnification.

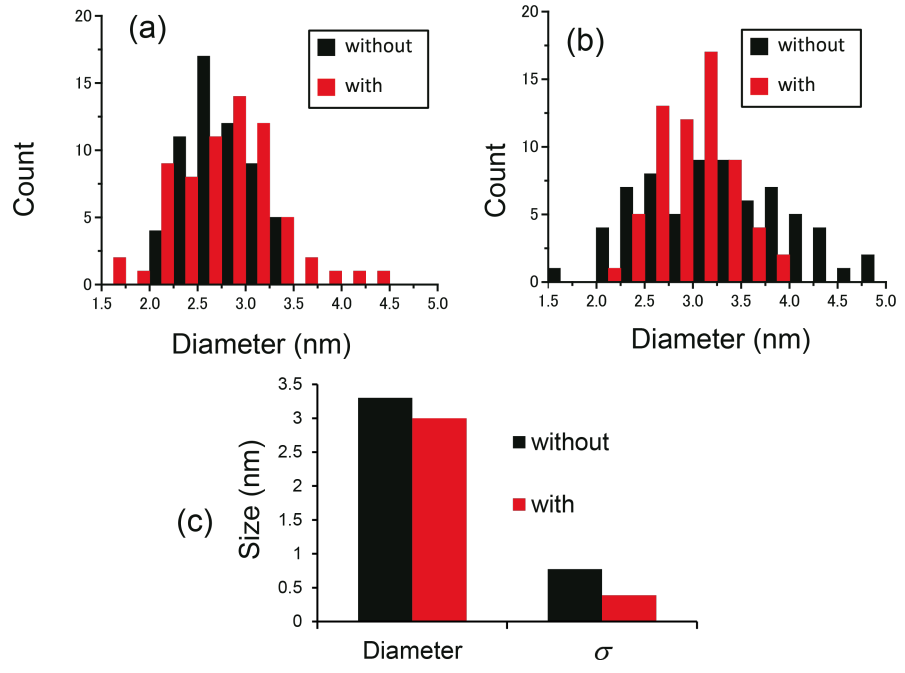

Figure 7: (a) Size distribution of among nanocrystals grown without and with 532 nm light (400 mW), t = 5 min. (b) Distribution of diameter among nanocrystals grown without and with 532 nm light (400 mW), t = 60 min. (c) Average diameter and σ.

Figure 7b show the size distribution for growth times of t = 5 and 60 min, after using 532 nm light (400 mW) during the heat treatment. Although the actual shape of ZAIS nanocrystals was non-circular, the diameter was determined as the equivalent diameter of circles that would occupy the same amount of space as the ZAIS nanocrystals. Figure 7c shows the average diameter, $\bar{d}$, and the standard deviation, $\sigma = \sqrt{\sum\left(d-\bar{d}\right)^2/\left(n-1\right)}$, of the diameter of ZAIS nanocrystals produced after t = 60 min. It indicates a decrease in diameter from 3.30 to 3.00 nm and a decrease in σ from 0.77 to 0.39 nm. These results support the postulates from Figure 4, namely the reduction of large ZAIS nanocrystals and the increase of smaller ZAIS nanocrystals by the irradiation of 532 nm light during synthesis.

In addition to examining the change in size distribution, we evaluated the aspect ratios of the nanocrystals by using TEM measurements. By using the TEM images (Figure 5 and Figure 6), we calculated the aspect ratio R (= b/a; a: shorter axis length, b: longer axis length, see Figure 8c). Figure 8a shows the distribution of values of R among ZAIS nanocrystals synthesized without and with irradiation of 532 nm light, at 400 mW for t = 60 min. The number of nanocrystals with larger R was decreased by introducing irradiation during the synthesis, and the value of the average R was decreased from 3.3 (without irradiation) to 2.4 (with irradiation). ZAIS consist of the solid solution $(AgIn)_xZn_{2(1-x)}S_2$. As x increases, it turns into $AgInS_2$ with a tetragonal crystal structure; as x decreases, it becomes ZnS with a cubic crystal structure (see Figure 8c) [13]. Therefore, the observed decrease in the value of R should have originated from the reduction in Ag and In content.

To support the above postulate of the change in crystal structure by using photo-assisted synthesis, we evaluated the TEM images. The black and red curves in Figure 8b show the cross-

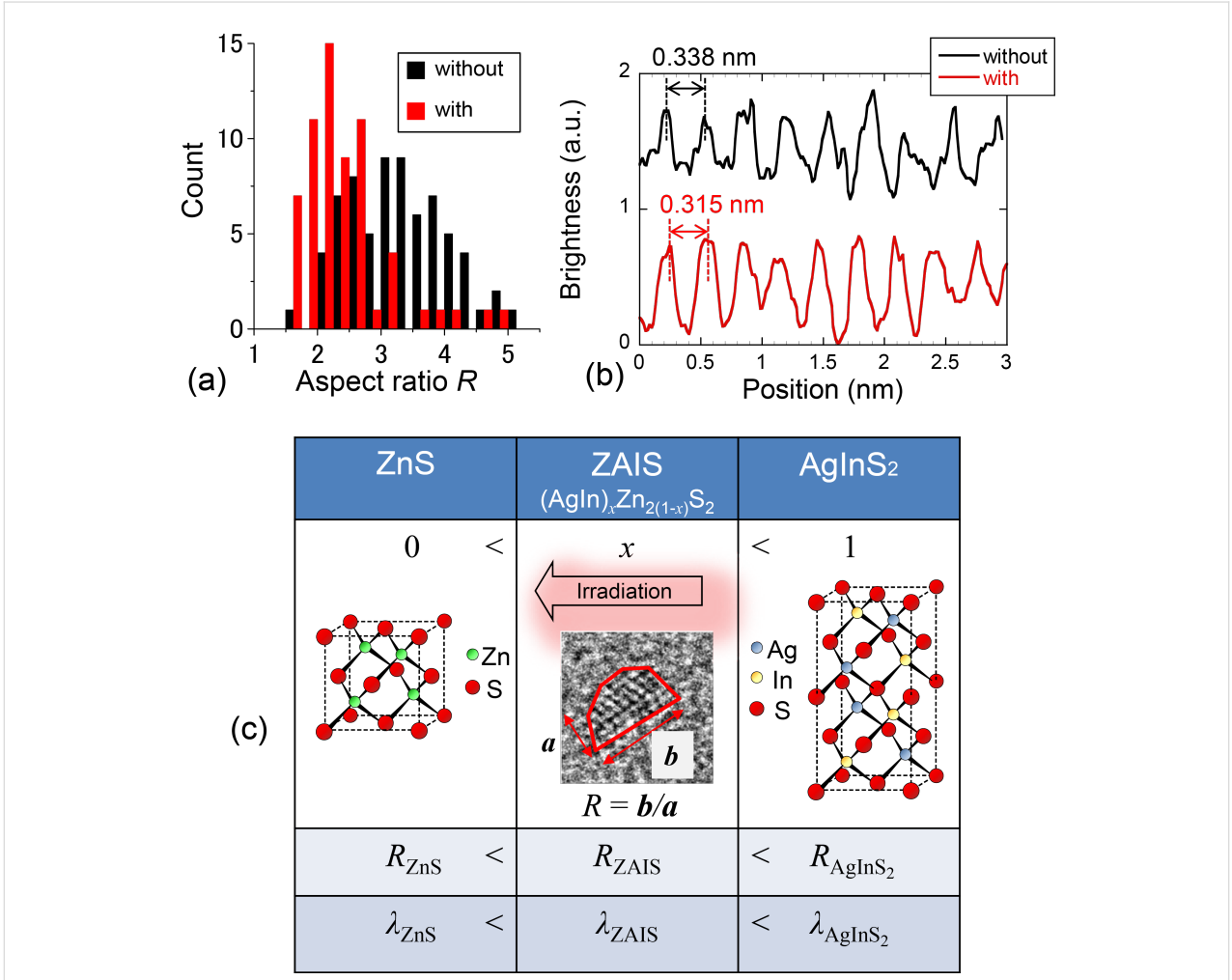

Figure 8: (a) Distribution of R among nanocrystals grown without and with 532 nm light (400 mW), for a growth time of t = 60 min. (b) Cross-sectional profiles of image brightness along the dashed white line in Figure 5b (without irradiation) and Figure 6b (with irradiation). (c) Schematic of the transition of the crystal structure of ZnS and $AgInS_2$ depending on the composition.

sectional profiles of image brightness along the white dashed lines in the TEM images in Figure 5b and Figure 6b of ZAIS nanocrystals grown without and with irradiation (t = 60 min), respectively. From these results, the average separation of the peak-to-peak distances was determined to be 0.338 nm with a standard deviation σ of 0.019 nm for nanocrystals grown without irradiation and 0.315 nm with σ of 0.025 nm for nanocrystals grown with irradiation. These values are comparable to the reported values of 0.335 nm for $AgInS_2$ nanocrystals [19] and 0.310 nm for ZnS nanocrystals [20]. These results also support the assertion that the observed decrease in R resulted from the reduction in Ag and In content. In other words, highly controlled nanocrystal size and uniform composition were realized by using photo-assisted synthesis.

Conclusion

In conclusion, we attained precise size and composition control of ZAIS nanocrystals by introducing light irradiation during synthesis. The PL measurements and TEM analysis confirmed the reduction of the PL spectral width and a corresponding reduction of the size distribution of the nanocrystals. Furthermore, these results indicate that the synthesized ZAIS nanocrystals had a higher crystallinity; thus, higher energy-transmission efficiency can be expected for nanophotonic devices.

Acknowledgements

The authors wish to express special thanks to Prof. Tsukasa Torimoto (Nagoya University) and Prof. Motoichi Ohtsu (University of Tokyo) for their active support and discussions. This work was partially supported by a Grant-in-Aid for Scientific Research (B) (No. 26286022), the Exploratory Research program (No. 26630122) of MEXT, JSPS Core-to-Core Program, A. Advanced Research Networks, and a research grant (Basic Research) from The Asahi Glass Foundation.

References

1. Kirchain, R.; Kimerling, L. *Nat. Photonics* **2007,** *1,* 303–305. doi:10.1038/nphoton.2007.84
2. Gramotnev, D. K.; Bozhevolnyi, S. I. *Nat. Photonics* **2014,** *8,* 13–22. doi:10.1038/nphoton.2013.232
3. Kawazoe, T.; Kobayashi, K.; Lim, J.; Narita, Y.; Ohtsu, M. *Phys. Rev. Lett.* **2002,** *88,* 067404. doi:10.1103/PhysRevLett.88.067404
4. Yatsui, T.; Jeong, H.; Ohtsu, M. *Appl. Phys. B* **2008,** *93,* 199–202. doi:10.1007/s00340-008-3154-8
5. Yatsui, T.; Sangu, S.; Kawazoe, T.; Ohtsu, M.; An, S. J.; Yoo, J.; Yi, G.-C. *Appl. Phys. Lett.* **2007,** *90,* 223110. doi:10.1063/1.2743949
6. Yatsui, T.; Nomura, W.; Mano, T.; Miyazaki, H. T.; Sakoda, K.; Kawazoe, T.; Ohtsu, M. *Appl. Phys. A* **2014,** *115,* 1–4. doi:10.1007/s00339-013-7905-y
7. Kawazoe, T.; Ohtsu, M.; Aso, S.; Sawado, Y.; Hosoda, Y.; Yoshizawa, K.; Akahane, K.; Yamamoto, N.; Naruse, M. *Appl. Phys. B* **2011,** *103,* 537–546. doi:10.1007/s00340-011-4375-9
8. Mukai, K.; Abe, S.; Sumi, H. *J. Phys. Chem. B* **1999,** *103,* 6096–6102. doi:10.1021/jp984469g
9. Ohtsu, M.; Kawazoe, T.; Yatsui, T.; Naruse, M. *IEEE J. Sel. Top. Quantum Electron.* **2008,** *14,* 1404–1417. doi:10.1109/JSTQE.2008.918110
10. Peng, X.; Manna, L.; Yang, W.; Wickham, J.; Scher, E.; Kadavanich, A.; Alivisatos, A. P. *Nature* **2000,** *404,* 59–61. doi:10.1038/35003535
11. Shirasaki, Y.; Supran, G. J.; Bawendi, M. G.; Bulović, V. *Nat. Photonics* **2013,** *7,* 13–23. doi:10.1038/nphoton.2012.328
12. Mashford, B. S.; Stevenson, M.; Popovic, Z.; Hamilton, C.; Zhou, Z.; Breen, C.; Steckel, J.; Bulovic, V.; Bawendi, M.; Coe-Sullivan, S.; Kazlas, P. T. *Nat. Photonics* **2013,** *7,* 407–412. doi:10.1038/nphoton.2013.70
13. Torimoto, T.; Adachi, T.; Okazaki, K.-i.; Sakuraoka, M.; Shibayama, T.; Ohtani, B.; Kudo, A.; Kuwabata, S. *J. Am. Chem. Soc.* **2007,** *129,* 12388–12389. doi:10.1021/ja0750470
14. Torimoto, T.; Murakami, S.-y.; Sakuraoka, M.; Iwasaki, K.; Okazaki, K.-i.; Shibayama, T.; Ohtani, B. *J. Phys. Chem. B* **2006,** *110,* 13314–13318. doi:10.1021/jp062645c
15. Xia, F.; Sekaric, L.; Vlasov, Y. *Nat. Photonics* **2007,** *1,* 65–71. doi:10.1038/nphoton.2006.42
16. Liu, Y.; Morishima, T.; Yatsui, T.; Kawazoe, T.; Ohtsu, M. *Nanotechnology* **2011,** *22,* 215605. doi:10.1088/0957-4484/22/21/215605
17. Liu, Y.; Yatsui, T.; Ohtsu, M. *Appl. Phys. B* **2012,** *108,* 707–711. doi:10.1007/s00340-012-5151-1
18. Koyama, H.; Koshida, N. *J. Appl. Phys.* **1993,** *74,* 6365–6367. doi:10.1063/1.355160
19. Deng, M.; Shen, S.; Wang, X.; Zhang, Y.; Xu, H.; Zhang, T.; Wang, Q. *CrystEngComm* **2013,** *15,* 6443–6447. doi:10.1039/c3ce40173a
20. Gayou, V. L.; Salazar Hernández, B.; Delgado Macuil, R.; Zavala, G.; Santiago, P.; Oliva, A. I. *J. Nano Res.* **2010,** *9,* 125–132. doi:10.4028/www.scientific.net/JNanoR.9.125

License and Terms